

MICROCOPY RESOLUTION TEST CHART
NATIONAL BUREAU OF STANDARDS 1963-A



LEVEL III

12

USAFA-TR-81-4

A093378

AD A108338

AIR FORCE ACADEMY

AERONAUTICS DIGEST - FALL/WINTER 1980

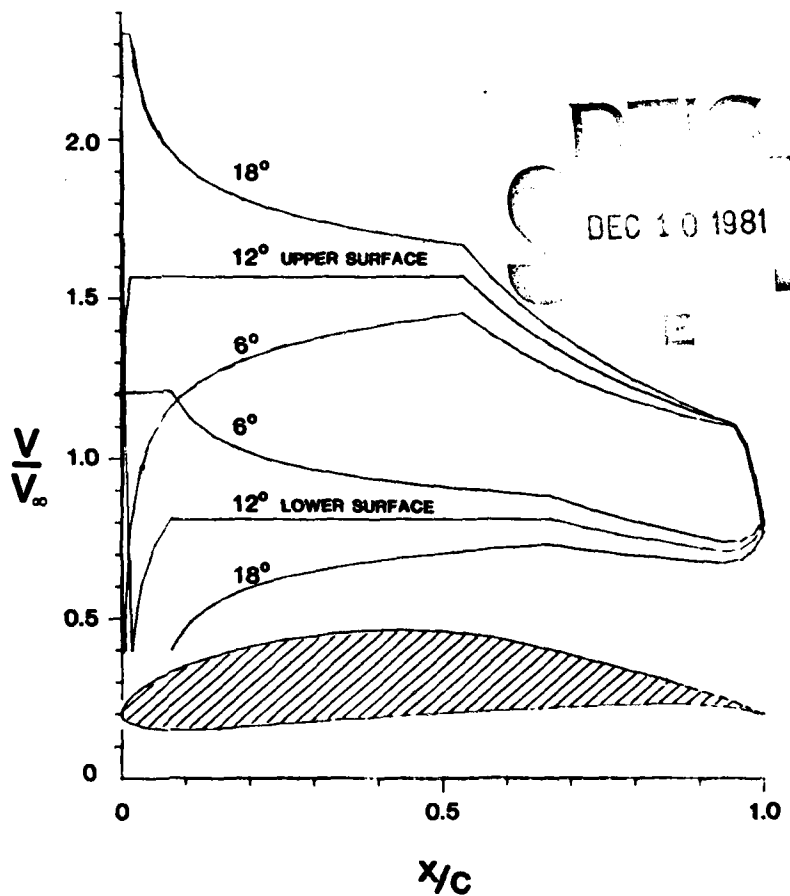
MAY 1981

FINAL REPORT

DTIC FILE COPY

APPROVED FOR PUBLIC RELEASE: DISTRIBUTION UNLIMITED

DEPARTMENT OF AERONAUTICS
DEAN OF THE FACULTY
UNITED STATES AIR FORCE ACADEMY
COLORADO 80840



DEC 10 1981

81 12 08 010

COVER:

The cover shows a typical computer-graphics plot of an airfoil which was designed using an airfoil design method developed by Professor Richard Eppler of the University of Stuttgart. This computerized design method allows the user to design an airfoil section shape that satisfies desired performance characteristics. It is used by USAF Academy cadets majoring in Aeronautical Engineering in their second course in Theoretical Aerodynamics.

The particular airfoil section shown on the cover was designed using the Eppler method to satisfy the following performance characteristics: (1) at 6 degrees angle of attack there is a short segment on the lower surface near the leading edge that has a constant velocity; (2) at 12 degrees angle of attack there is constant velocity over most of the forward portion of both the upper and lower surfaces; and (3) at 18 degrees angle of attack there is a short segment of constant velocity on the upper surface near the leading edge. Pressure recovery was specified as beginning on the upper surface about the mid-chord point and on the lower surface about two-thirds the chord.

Roger W. Gallington, Lt Col, USAF, Tenure Associate Professor

Editorial Review by Capt James M. Kempf, Department of English,
USAF Academy, Colorado 80840

This document is presented as a compilation of monographs worthy of publication. The United States Air Force Academy vouches for the quality of research, without necessarily endorsing the opinions and conclusions of the authors.

This Digest has been cleared for open publication and/or public release by the appropriate Office of Information in accordance with AFR 190-17 and DODD 5230.9. There is no objection to unlimited distribution of the Digest to the public at large, or by DDC to the National Technical Information Service.

This Digest has been reviewed and is approved for publication.

M.D. Bacon

M.D. Bacon, Colonel, USAF
Director of Research and
Continuing Education

UNCLASSIFIED

SECURITY CLASSIFICATION OF THIS PAGE (When Data Entered)

REPORT DOCUMENTATION PAGE		READ INSTRUCTIONS BEFORE COMPLETING FORM
1. REPORT NUMBER USAFA-TR-81-4	2. GOVT ACCESSION NO. AD-118338	3. RECIPIENT'S CATALOG NUMBER
4. TITLE (and Subtitle) Air Force Academy Aeronautics Digest Fall/Summer 1980		5. TYPE OF REPORT & PERIOD COVERED Final Report
		6. PERFORMING ORG. REPORT NUMBER
7. AUTHOR(s) Editors: A.M. Higgins J.M. Kempf E.J. Jumper B.J. Gregory		8. CONTRACT OR GRANT NUMBER(s) 141
9. PERFORMING ORGANIZATION NAME AND ADDRESS Department of Aeronautics United States Air Force Academy, CO 80840		10. PROGRAM ELEMENT, PROJECT, TASK AREA & WORK UNIT NUMBERS
11. CONTROLLING OFFICE NAME AND ADDRESS		12. REPORT DATE May 1981
		13. NUMBER OF PAGES 143
14. MONITORING AGENCY NAME & ADDRESS (if different from Controlling Office)		15. SECURITY CLASS. (of this report)
		15a. DECLASSIFICATION DOWNGRADING SCHEDULE
16. DISTRIBUTION STATEMENT (of this Report)		
17. DISTRIBUTION STATEMENT (of the abstract entered in Block 20, if different from Report)		
18. SUPPLEMENTARY NOTES		
19. KEY WORDS (Continue on reverse side if necessary and identify by block number) Aerodynamics, Flight Mechanics, Propulsion, Thermodynamics, Wind Tunnel, Aeronautical Instrumentation, Aeronautical History, Aero- space Biomechanics		
20. ABSTRACT (Continue on reverse side if necessary and identify by block number) This Digest covers unclassified research in aeronautics performed at the United States Air Force Academy during the six months ending 15 January 1981. This report includes technical papers in the spe- cific areas of aerodynamics, propulsion, experimental instrumenta- tion, biomechanics, engineering education, and aeronautical history.		

DD FORM 1473
1 JAN 73

EDITION OF 1 NOV 65 IS OBSOLETE

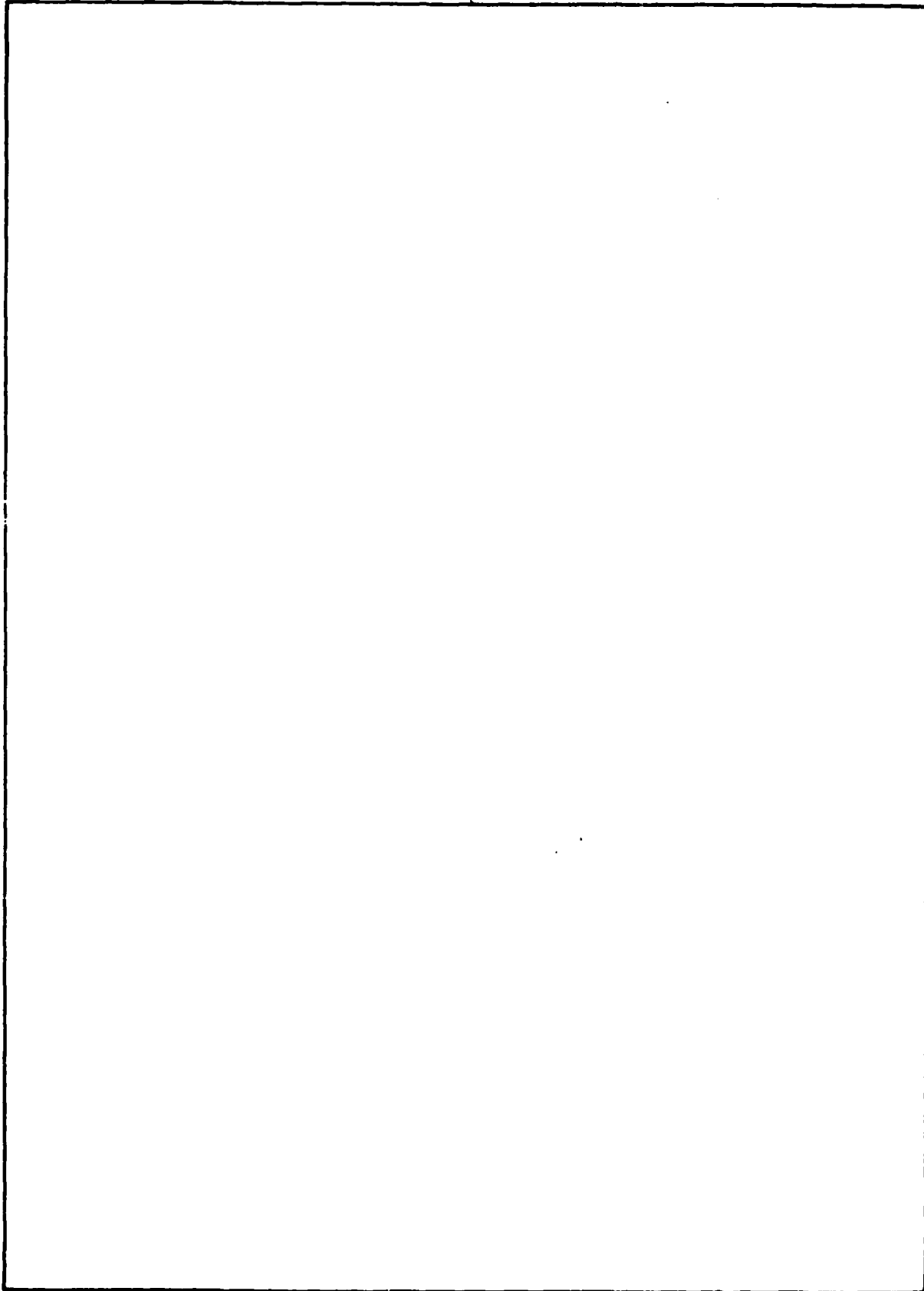
UNCLASSIFIED

SECURITY CLASSIFICATION OF THIS PAGE (When Data Entered)

01102

UNCLASSIFIED

SECURITY CLASSIFICATION OF THIS PAGE(When Data Entered)



UNCLASSIFIED

SECURITY CLASSIFICATION OF THIS PAGE(When Data Entered)

PREFACE

This report is the sixth issue of the Air Force Academy Aeronautics Digest.^{*} Our policy is to print articles which represent recent scholarly work by students and faculty of the Department of Aeronautics, members of other departments of the Academy and the Frank J. Seiler Research Laboratory, researchers directly or indirectly involved with USAFA-sponsored projects, and authors in fields of interest to the USAFA.

In addition to complete papers, the Digest also includes, when appropriate, abstracts of lengthier reports and articles published in other formats. The editors will consider for publication contributions in the general field of Aeronautics, including:

- Aeronautical Engineering
 - Flight Mechanics
 - Propulsion
 - Structures
 - Instrumentation
- Fluid Mechanics
- Thermodynamics and Heat Transfer
- Biomechanics
- Engineering Education
- Aeronautical History

Papers on other topics will be considered on an individual basis. Contributions should be sent to:

Editor, Aeronautics Digest
DFAN
US Air Force Academy, CO 80840

The Aeronautics Digest is presently edited by Maj A.M. Higgins, PhD; Maj E.J. Jumper, PhD; and Capt J.M. Kempf, Department of English, who provided the final editorial review. Our thanks also to our Associate Editor, Barbara J. Gregory, of Contract Technical Services, Inc.

* The first five issues of the Digest can be ordered from the Defense Documentation Center (DDC), Cameron Station, Alexandria, VA 22324. Use the following AD numbers: Aeronautics Digest - Spring 1978, ADA060207; Aeronautics Digest - Fall 1978, ADA069044; Aeronautics Digest - Spring 1979, ADA075419; Aeronautics Digest - Fall 1979, ADA085770; and Aeronautics Digest - Spring/Summer 1980, ADA096678.

CONTENTS

<u>Section</u>	<u>Page</u>
I. AERODYNAMICS	1
→ PARTIAL COMMENTS INCLUDE: <ul style="list-style-type: none"> → CANARD WAKE MEASUREMENT AND DESCRIPTION. ----G. Sisson and R. Crandall → EXAMINING A RULE OF THUMB FOR THE RELATION BETWEEN CAMBER AND ZERO-LIFT ANGLE OF ATTACK; ----E.J. Jumper → EXPERIMENTAL AERODYNAMIC EFFECTS OF THREE-DIMENSIONAL SQUARE CROSS-SECTION MISSILES AT MODERATE ANGLES OF ATTACK; ----T.R. Yechout, G.J. Zollars, and D.C. Daniel 	2 21 41
II. INSTRUMENTATION AND HARDWARE	56
<ul style="list-style-type: none"> → CALIBRATION OF SEVEN-HOLE PROBES SUITABLE FOR HIGH ANGLES IN SUBSONIC COMPRESSIBLE FLOWS; ----A.A. Gerner and C.L. Maurer 	57
III. BIOMECHANICS	93
<ul style="list-style-type: none"> → DEVELOPMENT OF DESIGN CRITERIA FOR RAPID PRE-EJECTION CREW RESTRAINT OF UPPER TORSO; ----A.M. Higgins and G. Kroh 	94
VI. ENGINEERING EDUCATION	112
<ul style="list-style-type: none"> → SI UNITS (MASS?, WEIGHT?) LET'S DO IT RIGHT, <i>and</i> ----R.F. Felton 	113
V. AERONAUTICAL HISTORY	119
<ul style="list-style-type: none"> → THE EARLY HISTORY OF THE JET ENGINE. ----Sir Frank Whittle 	120

Accession For	
NTIS GRA&I	<input checked="" type="checkbox"/>
NTIS J	<input type="checkbox"/>
Unannounced	<input type="checkbox"/>
Justification	<input type="checkbox"/>
A	

SECTION I

Aerodynamics

CANARD WAKE MEASUREMENT AND DESCRIPTION

G. Sisson* and R. Crandall**

Abstract

This paper describes a method for measuring, describing, and visualizing the complex flow fields that occur when canard-configured aircraft models are tested in the wind tunnel. This simple, rapid, and inexpensive technique is a source of complex empirical aerodynamic data suitable for the preliminary design of future fighter aircraft. The technique makes use of a miniature seven-hole probe, a computer-driven traverse mechanism, computerized data acquisition equipment, and computer graphic displays. Numerical and graphic descriptions of wakes from three canard models are presented.

I. Introduction

Since the summer of 1978 the U.S. Air Force Academy and NASA's Ames Research Center have participated in a joint research effort to understand the aerodynamics of canard-equipped aircraft. These configurations are similar to proposed fighter aircraft designs for the 1990's, which have pitch control surfaces located in front of the wings in lieu of a conventional aft-located tail. The program began as summer research projects, with Academy cadets and officers attempting to analytically predict the aerodynamics of these configurations using potential flow computer analysis. Their efforts were largely unsuccessful because the location of the canard wake was not known in advance. To solve this problem, NASA Ames contracted the USAF Academy Department of Aeronautics to develop a rapid, inexpensive technique to precisely measure the location of canard wakes.

The approach taken used specially-designed seven-hole pressure probes to collect pressure measurements in the model wake. One characteristic of canard wakes is a region of lower fluid-mechanical energy seen as a drop in total pressure. This wake exists at each point in the airstream where the measured total pressure differs significantly from the free-stream value. This region is located by placing the pressure-measuring probe at many points downstream of the model using a three-dimensional positioning mechanism known as a traverse. The measured pressures were plotted as contour graphs, where the steep pressure gradients (like those occurring at the edge of the canard wake) were indicated by a collection of closely-spaced contour lines. A series of these graphs compose a mapping of the flow field.

This entire procedure was reduced to four computer programs run in sequence. Each program prompts the computer operator for all necessary information. The time and expense required to perform the procedure is primarily a function of the three-dimensional traverse mechanism and how quickly it can move the pressure-measuring probe. The reduction and display of the data takes less than two additional minutes after data collection is complete. The procedure has been successfully performed by many Academy cadets and

*Captain, USAF, Department of Aeronautics, DFAN

**2nd Lieutenant, USAF, Department of Aeronautics, DFAN

officers on a variety of aerodynamic models. On the basis of these results the research can be considered successful in developing a new technique which can simply, rapidly, and inexpensively measure and describe the wakes of wind tunnel aerodynamic models.

This paper consists of four parts: (1) a theory section describing the expected results of mapping a theoretical vortex in the free-stream direction, (2) an apparatus description, (3) a procedure description, and (4) a discussion of the results of mapping three canard wakes. An appendix consisting of the user manual for the four computer programs is included.

II. Theory

One of the simplest pieces of instrumentation for studying steady flow field properties is the pressure probe. It is easy to understand and manufacture, its use is widespread, and it directly measures one of the most important aerodynamic properties. The seven-hole pressure probe extends these characteristics to include direct measurement of local flow angles and static, total and dynamic pressure, and allows calculation of local velocities at angles up to 80 degrees off axis without iteration (Ref. 1). These properties make the seven-hole probe the best instrumentation for this research.

Total pressure is a measure of total fluid-mechanical energy and results from slowing the fluid velocity to zero without loss. Static pressure is the pressure exerted on an aerodynamic surface parallel to the free stream. Dynamic pressure is total pressure minus static pressure. All three pressures can be used to locate the canard wake by observing where large changes or gradients exist in the flow. Since these pressures are affected by slight changes in wind tunnel velocity or room temperature, pressure coefficients will be used instead, where the differences in local pressures and reference pressures are divided by tunnel dynamic pressure, resulting in:

$$\frac{\text{Static Pressure}}{\text{Dynamic Pressure}} = C_{\text{STATIC}} = \frac{P_{\infty L} - P_{\infty}}{P_0 - P_{\infty}}$$

$$\frac{\text{Total Pressure}}{\text{Dynamic Pressure}} = C_{\text{TOTAL}} = \frac{P_{0L} - P_0}{P_0 - P_{\infty}}$$

where

- $P_{\infty L}$ = Local Static Pressure (measured by probe flow)
- P_{∞} = Free Stream Static Pressure
- P_{0L} = Local Total Pressure (measured by probe in flow)
- P_0 = Free Stream Total Pressure

To anticipate what our coefficients will resemble in the canard wake, we will start with a simpler example of an ideal two-dimensional vortex (Ref. 2). In an ideal two-dimensional vortex, angular velocity increases exponentially as the distance to the vortex filament (radius) decreases (Figure 1). In reality the viscosity of the fluid reduces

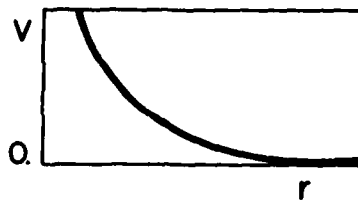


Figure 1. Fluid Velocity Versus Distance from Vortex Center for an Ideal Vortex

the angular velocity long before it reaches infinity (Ref. 3). In this region where viscous effects are substantial, the angular velocity drops until it is zero at the vortex center. Figure 2 shows the velocity distribution of a vortex with a viscous core

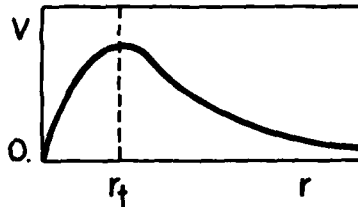


Figure 2. Fluid Velocity Versus Distance from Vortex Center for a Real Fluid

(Ref. 3). At distances greater than r_t , the flow is approximately inviscid.

The conventional aerodynamic pressure coefficient is defined as

$$C_{P_A} = \frac{P_A - P_\infty}{\frac{1}{2} \rho_\infty V_\infty^2} ,$$

where P_A is local static pressure at any Point A. In a steady, incompressible flow we have

$$\frac{1}{2} \rho_\infty V_\infty^2 = P_0 - P_\infty ,$$

and then

$$C_{STATIC} = \frac{P_{\infty L} - P_\infty}{P_0 - P_\infty} = \frac{P_{\infty L} - P_\infty}{\frac{1}{2} \rho_\infty V_\infty^2} ,$$

which yields

$$C_{STATIC} = C_{P_A} .$$

C_p is also defined by

$$C_p = 1 - \left(\frac{V_L}{V_\infty} \right)^2 .$$

Since the conditions at infinity approach free-stream conditions, C_p and C_{STATIC} approach zero. As the radius decreases from infinity to r_t , the angular velocity increases. This

increase in velocity causes the static pressure to drop. Hence, as we go from r_∞ to r_t , C_{STATIC} goes from zero to a negative value.

Out to r_t , viscous effects preclude the use of the previous equations. This viscous region has recently been examined experimentally, and Figure 3 shows the typical C_{STATIC} variation in this region as well as the C_{STATIC} variation in the inviscid region which was previously discussed. Thus the effect of vorticity shed from the canard of

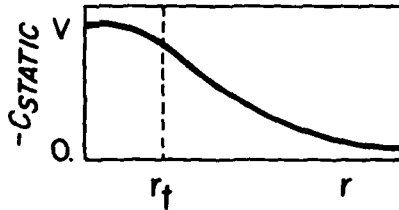


Figure 3. Typical C_{STATIC} Behavior with Distance from the Vortex Center

our wind tunnel model induces higher velocities and therefore causes a decrease in local static pressure at points in the flow near that vorticity. Unfortunately, the C_{STATIC} coefficient does not allow us to clearly define the edge of the wake. This is evident in Figure 3 where r_t has been arbitrarily located near the inflection point of the curve.

The C_{TOTAL} coefficient, however, can be used to locate the edge of the wake. Bernoulli's equation shows that total pressure is constant in isentropic, incompressible flow. Using our definition,

$$C_{TOTAL} = \frac{P_{oL} - P_o}{P_o - P_\infty} ,$$

it follows that the coefficient of total pressure in the inviscid region is zero. Since viscosity causes a loss in total mechanical energy, P_o decreases at radii less than r_t . As P_{oL} drops, C_{TOTAL} will decrease to a negative value. Figure 4 approximately shows this behavior. We thus expect the canard wake to appear as a mound with a depression in

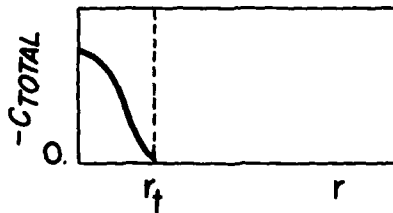


Figure 4. C_{TOTAL} (Theoretical) Versus Distance from the Vortex Center

it on the C_{TOTAL} contour maps. If we define the edge of the wake as points where the total pressure begins to deviate from free stream, i.e., r_t , we have the indicator of the wake location we desire.

An aerodynamic problem associated with the canard wake is the lack of dynamic pressure resulting from viscous losses. If there is a connection between the local dynamic pressure and our definition of C_{STATIC} , it might also serve to locate the edge of the wake. Our definition is

$$C_{DYN} = C_{TOTAL} - C_{STATIC}$$

Manipulating these equations gives

$$\begin{aligned} C_{DYN} = C_{TOTAL} - C_{STATIC} &= \frac{P_{oL} - P_o}{P_o - P_\infty} - \frac{P_{\infty L} - P_\infty}{P_o - P_\infty} \\ &= \frac{P_{oL} - P_{\infty L} - (P_o - P_\infty)}{P_o - P_\infty} \\ &= \frac{P_{oL} - P_{\infty L}}{P_o - P_\infty} - 1 \end{aligned}$$

$P_{oL} - P_{\infty L}$ is the local dynamic pressure, while $P_o - P_\infty$ is the free-stream dynamic pressure. Thus, C_{DYN} is proportional to the ratio of local dynamic pressure to free-stream dynamic pressure.

Since the conditions at infinity approach those of free stream, C_{DYN} will be approximately zero. $C_{DYN} = |C_{STATIC}|$ from infinity to r_t since $C_{TOTAL} = 0$. At the center of the vortex, local velocity and thus local dynamic pressure is zero, causing C_{DYN} to equal -1. From r_t to the center, C_{DYN} goes from $|C_{STATIC}|$ to -1 as in Figure 5. Thus

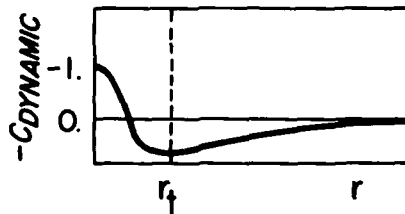


Figure 5. $C_{DYNAMIC}$ (Theoretical) Versus Distance from the Vortex Center

C_{DYN} also provides an indication of wake location when it reaches the point of its local maximum.

To this point we have considered only a single, isolated two-dimensional vortex. The actual canard wake is much more complex and includes many other factors such as flow separation, multiple vortices, and fuselage interference. We therefore must recognize that this theory only provides us an approximate guide to explain this complex wake behavior.

To measure this complex flow we used a seven-hole probe. Then, using the procedure outlined in Ref. 1, we calculated the angle of attack, α , sideslip angle, β , and two pressure coefficients C_o and C_∞ directly from the seven measured pressures. C_{TOTAL} and C_{STATIC} are calculated using C_o and C_∞ , and C_{DYN} is calculated from C_{TOTAL} and C_{STATIC} .

After the data is collected and all coefficients are calculated, we graphically display a three-dimensional surface consisting of the Y and Z location of each point and the desired coefficient. The graphs are displayed with either an axonometric or contour projection. (The 1980 Spring/Summer Edition of the Aeronautics Digest displays an axonometric projection on its cover.)

III. Apparatus

The apparatus we used to perform these tests consisted of a model, seven-hole probe, traverse mechanism, wind tunnel, and data acquisition system.

A. Model

The model used in the wind tunnel was a variable-height canard with swept-back wings. The canard was positioned at either a high, middle, or low position. Because of the size of the subsonic wind tunnel used, we utilized a half-span model. This half-span model was a replica of one used at NASA in their Langley Wind Tunnel Facility. The model differs slightly in several linear dimensions from NASA's model because of construction problems. The dimensions of the model with the canard in the low position are shown in Figures 6 and 7.

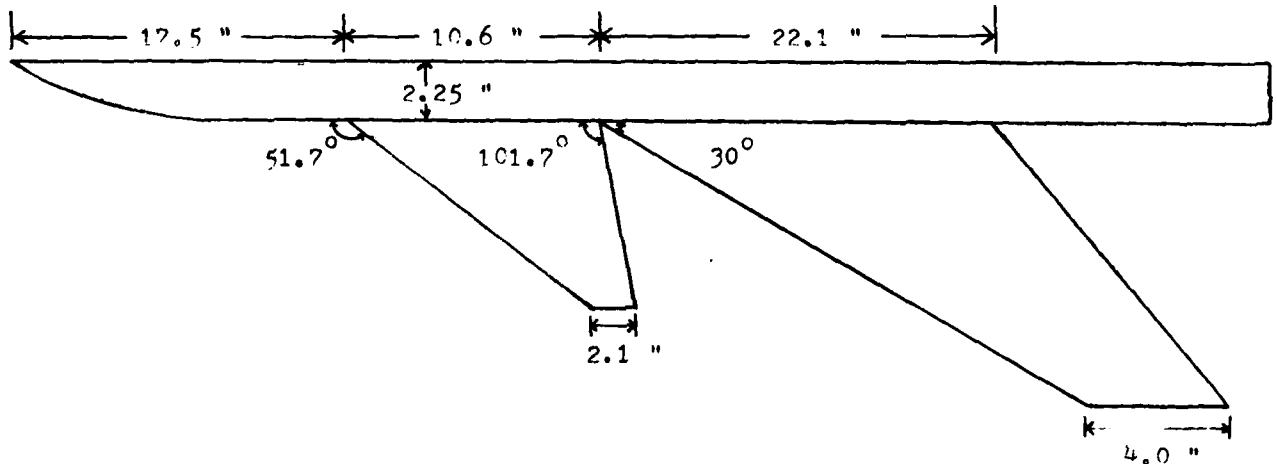


Figure 6. Canard Model (top view)

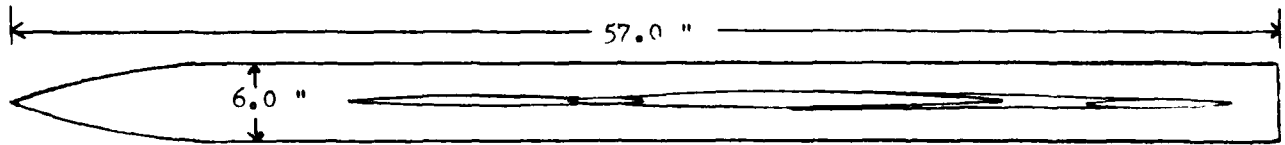


Figure 7. Canard Model (side view)

B. Probe

We used the seven-hole probe built by Hollenbaugh and reported by Gallington (Ref. 1). This probe was calibrated last year in the subsonic wind tunnel. The hole arrangement is shown in Figure 8.

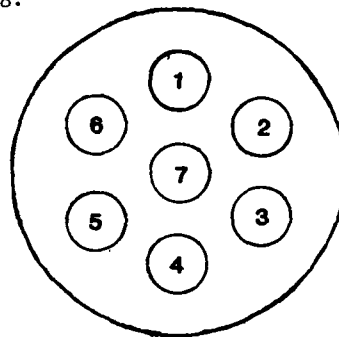


Figure 8. Probe Hole Arrangement

C. Traverse Mechanism

We used a previously-designed three-dimensional traverse mechanism and control unit developed by the Frank J. Seiler Research Laboratory for the subsonic wind tunnel. The axes of the traverse are shown in Figure 9. The traverse is computer-driven in the

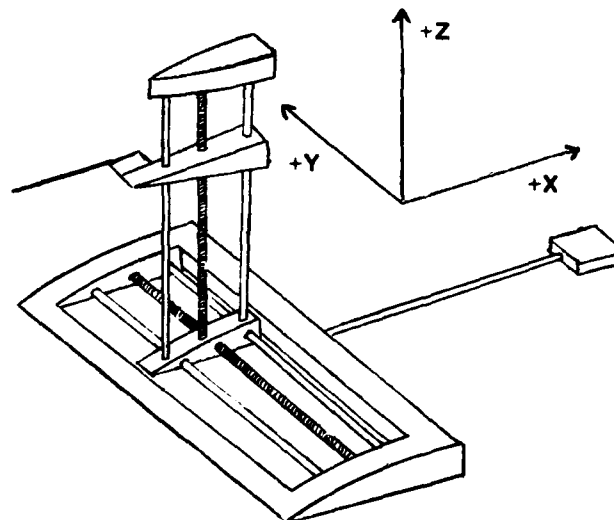


Figure 9. Traverse Mechanism Axes

Y and Z direction and manually controlled in the X direction.

D. Wind Tunnel

The experiment used the large closed-circuit wind tunnel which has a two foot by three foot test section and a velocity range from 50 ft/sec to 400 ft/sec at atmospheric pressure. The tunnel is driven by a 200-horsepower synchronous motor coupled with a fluid drive unit which is used to control the RPM of the four-bladed compressor. The tunnel does not have a heat exchanger, which caused tunnel velocity and temperature to increase throughout each run.

E. Data Acquisition System

Seven Statham PM6TC $\pm 1-350$ transducers were used to convert the probe pressures to voltages. Ten Ectron Model 560 amplifiers were used. A PDP-11/45 computer was used to drive the traverse and collect and reduce the data. The following peripherals and software were used in the data acquisition/reduction process:

- 1) A teletypewriter used as the system list device
- 2) A control/graphic display terminal used to display plots
- 3) A fast access 40-megabyte disk mass storage device
- 4) A system which converts analog signals from the transducers and traverse into digital form suitable for computer use
- 5) Standard graphics software for the display terminal
- 6) A high quality, flat bed pen plotter
- 7) A thermal hard copy device hooked into the display terminal

IV. Procedure

The actual test procedure can be considered the sequential execution of four computer programs. They were VOLCAL.FTN, TOPWNG.FTN, COEF7.FTN, and SCALAR.FTN. See Appendix A for user instructions for each program. The apparatus had to be installed in the wind tunnel to use the first two programs, but the latter two required only the PDP-11/45 computer.

The first step after the model, traverse, and probe were installed in the wind tunnel was to run VOLCAL.FTN on the computer. VOLCAL used a tri-linear scheme to define the measurement region as a variable number of points on a variable number of planes in a linear prismatoid. VOLCAL stored the three-dimensional coordinates of all the points in each plane in a data file, VOLUME.DAT.

The next program, TOPWNG.FTN, drove the probe to each point defined in VOLUME.DAT. It measured the pressures on each of the probe holes along with the tunnel total pressure, static pressure, and temperature. After completely measuring all the points in a given plane, the program wrote the data out to a file called WNGMAP.DAT.

COEF7.FTN reduced all the data stored in WNGMAP.DAT. Seven sets of calibration

coefficients had been previously determined based on the highest of the seven pressures. Two angles and two pressure coefficients were determined from the measured pressures and calibration coefficients which described the local total and static pressures and the local flow angularity (Ref. 1). The reduced data was stored in a file called CONTUR.DAT.

The last program, SCALAR.FTN, produced the graphs. The graphs were projected on the display terminal and hard copies were made on the pen plotter. Both axonometric and contour plots were created.

V. Discussion

Data were collected on three different canard wakes using the parametric model described above. Canard positions of 0 inches, 1.125 inches, and 2.75 inches above the plane of the aft-swept wing were investigated. All were at 11 degrees angle of attack. In addition, oil flow visualizations were performed on the high canard model at angles of attack of 11 and 22 degrees. Eight planes of data perpendicular to the free stream were collected for each wake. The oil flows will be discussed first, followed by a discussion of the wakes.

A sketch of the oil flow at 11 degrees angle of attack is shown in Figure 10 and it shows the main features of the flow over the canard and wing. On the canard we see a separation line and a reattachment line. Between the two the oil shows the existence of a large degree of spanwise flow caused by a vortex. This vortex will be called the canard leading edge separation vortex. It exists at the low angle of attack of 11 degrees because the leading edge radius of the canard is near zero. Outside the separation line

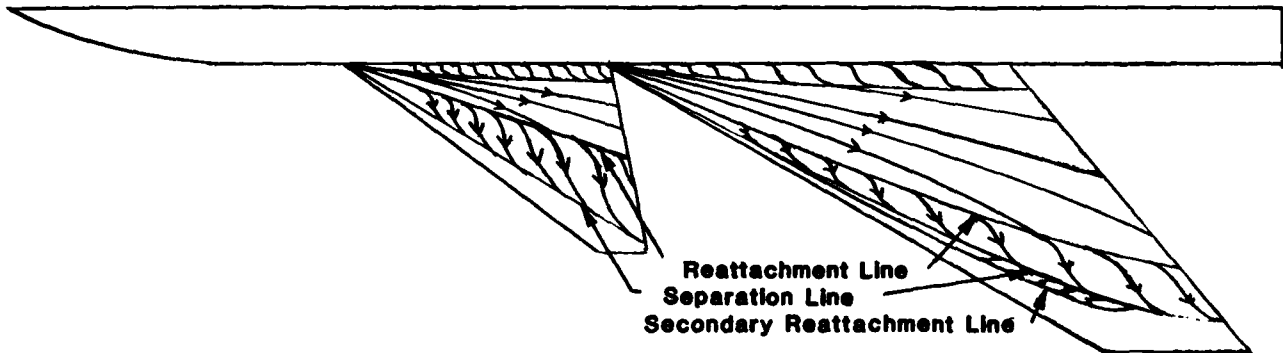


Figure 10. Oil Flow at Alpha = 11 Degrees

the oil has no streaks, indicating the flow is severely separated. To describe this region by potential flow would be very difficult.

On the wing a similar separated flow exists. One different feature is the occurrence of a weak secondary reattachment line outboard of the separation line. The small second-

ary separation vortex which causes this phenomenon is well-documented for highly swept wings (Ref. 4).

The oil flow inside the reattachment line shows the existence of a second, very weak vortex emanating from the non-faired canard-fuselage junction. The oil flow at 22 degrees shows the same results, differing only in the amount of separated flow. Since one of the reasons for mapping these wakes was to aid in their correct potential flow modeling, we chose to concentrate our efforts at 11 degrees angle of attack.

The middle-positioned canard wake will be discussed in detail first. Comparisons with the low- and high-positioned canard wakes will follow.

Contour maps showing lines of constant local total pressure in eight planes of data taken perpendicular to the free stream are presented in Figure 11. The X-axis is parallel to the free stream and therefore is at an 11-degree angle with the longitudinal axis of the fuselage. The Y-axis of the canard is increasing in the inboard direction and its origin is at the trailing edge of the canard tip.

The first plane of data at $X = .3$ inches behind the canard tip shows a relatively concentrated region of low total pressure inboard and above the canard tip (Figure 11a). The point of minimum pressure marks the center of the canard leading edge separation vortex. Outboard of this is another low-pressure region located above the canard tip, marking the center of the canard tip vortex. These two vortices in such close proximity create a saddle-like structure when plotted in three dimensions (total pressure plotted orthogonally to the Y and Z spacial dimensions. Both vortices are rotating in a clockwise sense when looking into the free stream. The low-pressure regions located seven inches inboard are the result of fuselage-canard interactions because of the lack of well-designed fairing.

As we move aft in Figures 11b through 11h we see the local total pressure and C_{TOTAL} coefficient increasing as viscous effects reduce the magnitude of velocity gradients in the flow. The integrated total pressure deficit, of course, remains the same.

The relative strengths of the canard tip and separation vortices are evidenced by the magnitudes of the C_{TOTAL} pressure coefficient and also by the relative movements of the vortex centers. The movement of the canard tip vortex in a clockwise fashion about a point close to the separation vortex center shows the separation vortex is much stronger, inducing more movement in the tip vortex than it can induce in the separation vortex.

In Figures 11e through 11h we see a new structure forming at the bottom and moving outboard as we go aft. This is the wing leading edge separation vortex. The entire structure could not be mapped due to geometric limitations on the traverse mechanism. Figures 11g and 11h show the wing separation vortex is asymmetrical with a small flow structure located inboard. We do not know the cause of this small structure which consistently appears. We suggest that the leading edge separation vortex on a highly swept wing needs to be studied in greater detail.

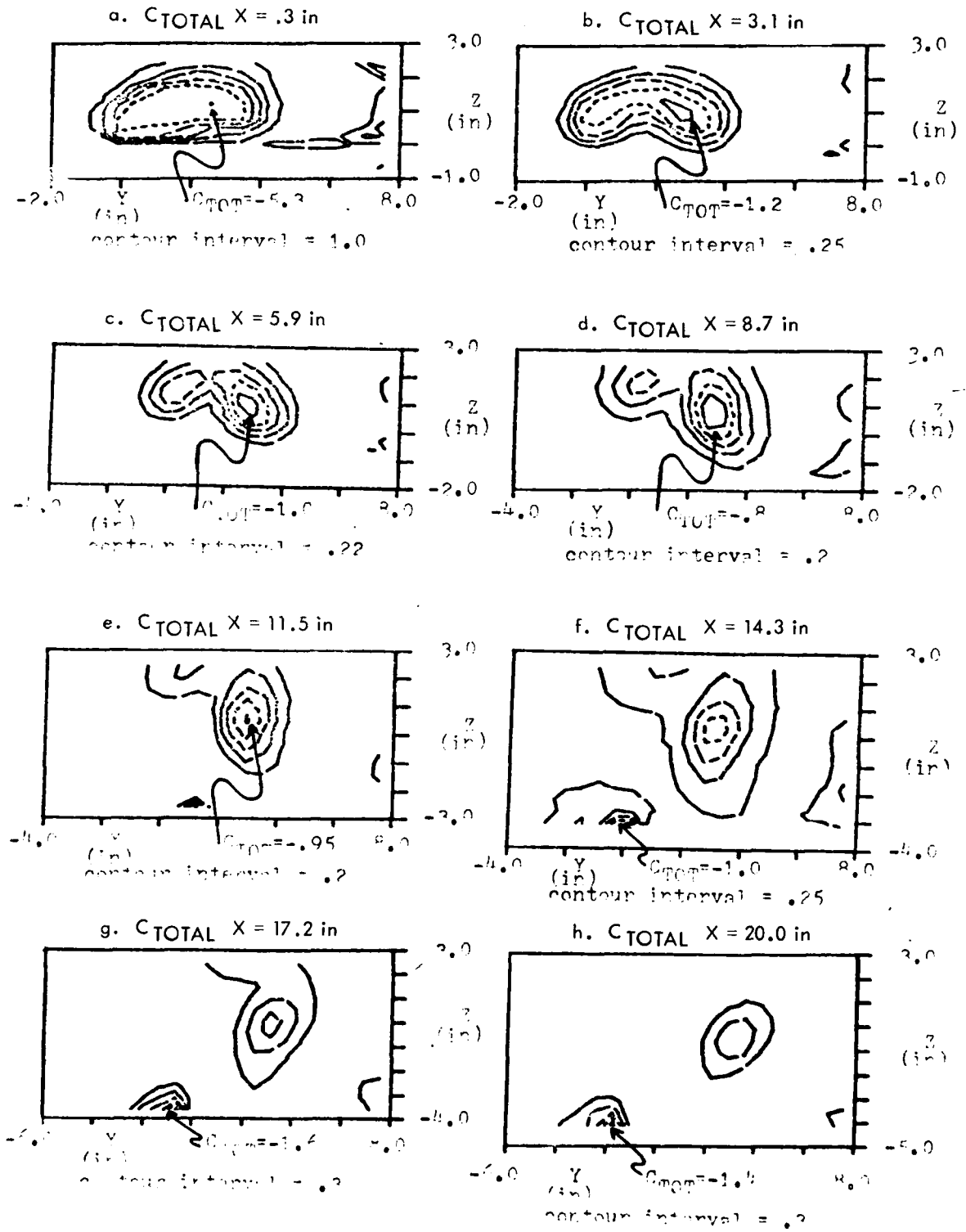


Figure 11. Total Pressure Coefficient

Nowhere in Figures 11a through 11g do we see the effects of the trailing vorticity shed from the canard trailing edge as a result of changes in the spanwise load distribution. It may be that the expected feature has a characteristic dimension that is much smaller than the resolution limit of the probe. This also needs to be studied in more detail.

The approximate locations of the centers of the canard tip and separation vortices versus X are given in Table 1. As we go aft the canard tip vortex goes up and inboard,

Table 1
CANARD VORTEX CENTER LOCATION

MIDDLE CANARD ALPHA = 11°				
	TIP		SEPARATION	
X	Y	Z	Y	Z
.3	.5	.7	2.7	1.2
3.1	.4	1.0	2.7	1.0
5.9	.2	1.3	2.7	.9
8.7	.2	1.7	2.8	.9
11.5	.3	2.1	2.9	.6
14.3	-	-	3.1	.4
17.2	-	-	3.1	0.0
20.0	-	-	3.1	-.5

while the separation vortex goes down. This downward movement is approximately half the angle of attack.

The local static pressure and static pressure coefficient are inversely related to the magnitude of local velocity. Examining Figure 12a, we see a low-pressure and thus high-velocity flow structure at the Y and Z coordinates (3.5, 1.9). Just below and inboard exists a relatively high-pressure, low-velocity structure forming a "static pressure doublet." One possible explanation for this structure is that the low-velocity region represents the vortex core with its region of rigid body rotation. If the high velocity represents the edge of the viscous-potential flow boundary, by theory it should encircle the vortex core. The fact that it does not suggests the answer may be that the characteristic of the flow structure is less than the resolution limit of the probe. This may also be causing the discrepancy between the center of the low-velocity region and the center of the total pressure loss. The resolution limit needs to be quantified.

An interesting feature of the static pressure map is the linear, high-pressure/low-velocity ridge located between points (0, .3) and (3.5, .3). This appears to be the wake of the shed vorticity from the canard trailing edge because of changes in the spanwise load distribution. If we examine static pressures on a line perpendicular to this structure we see a low-pressure/high-velocity region, a high-pressure/low-velocity wake, and a low-pressure/high-velocity region below. This classic wake structure is quickly dissipated as we go aft because of viscous effects.

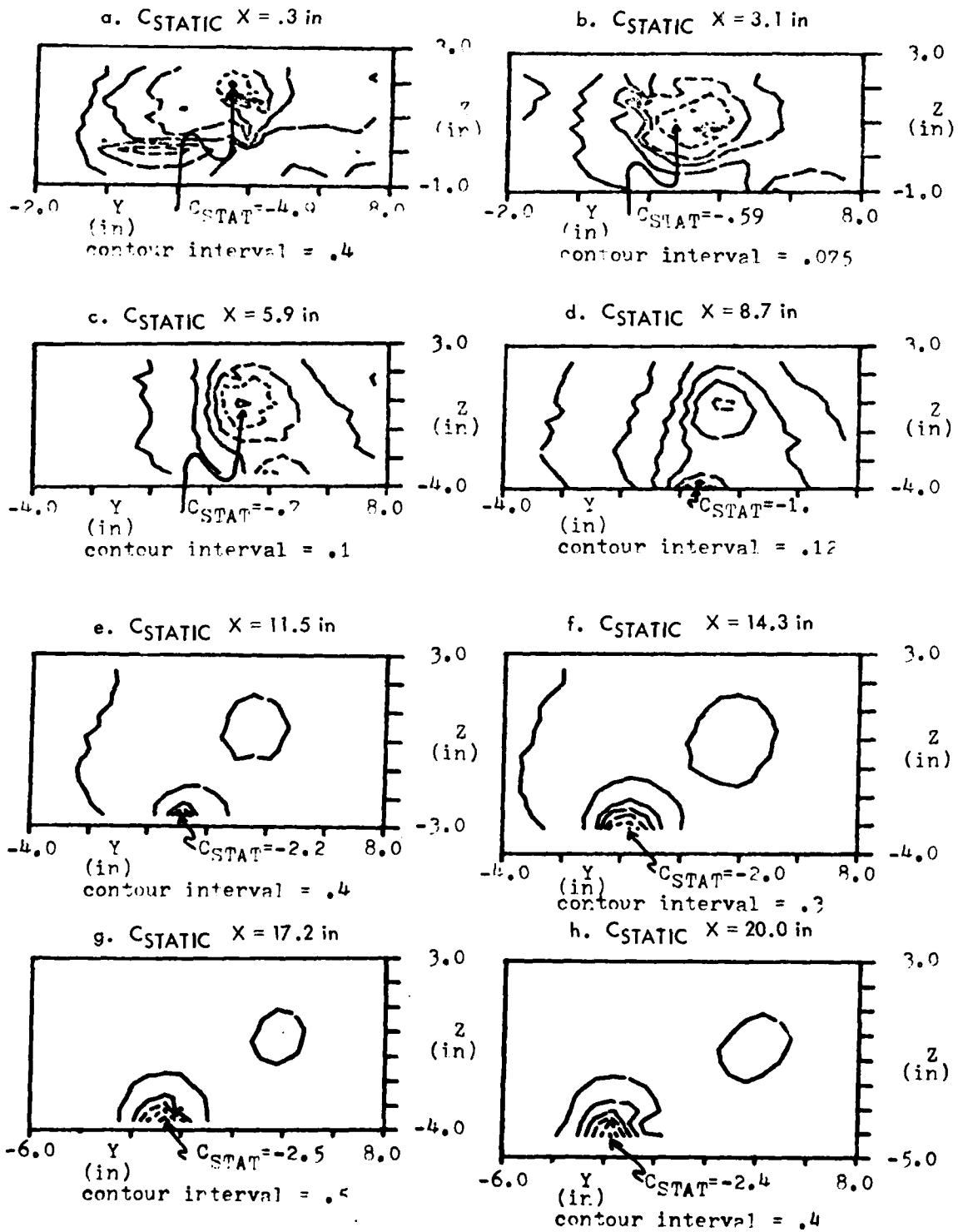


Figure 12. Static Pressure Coefficient

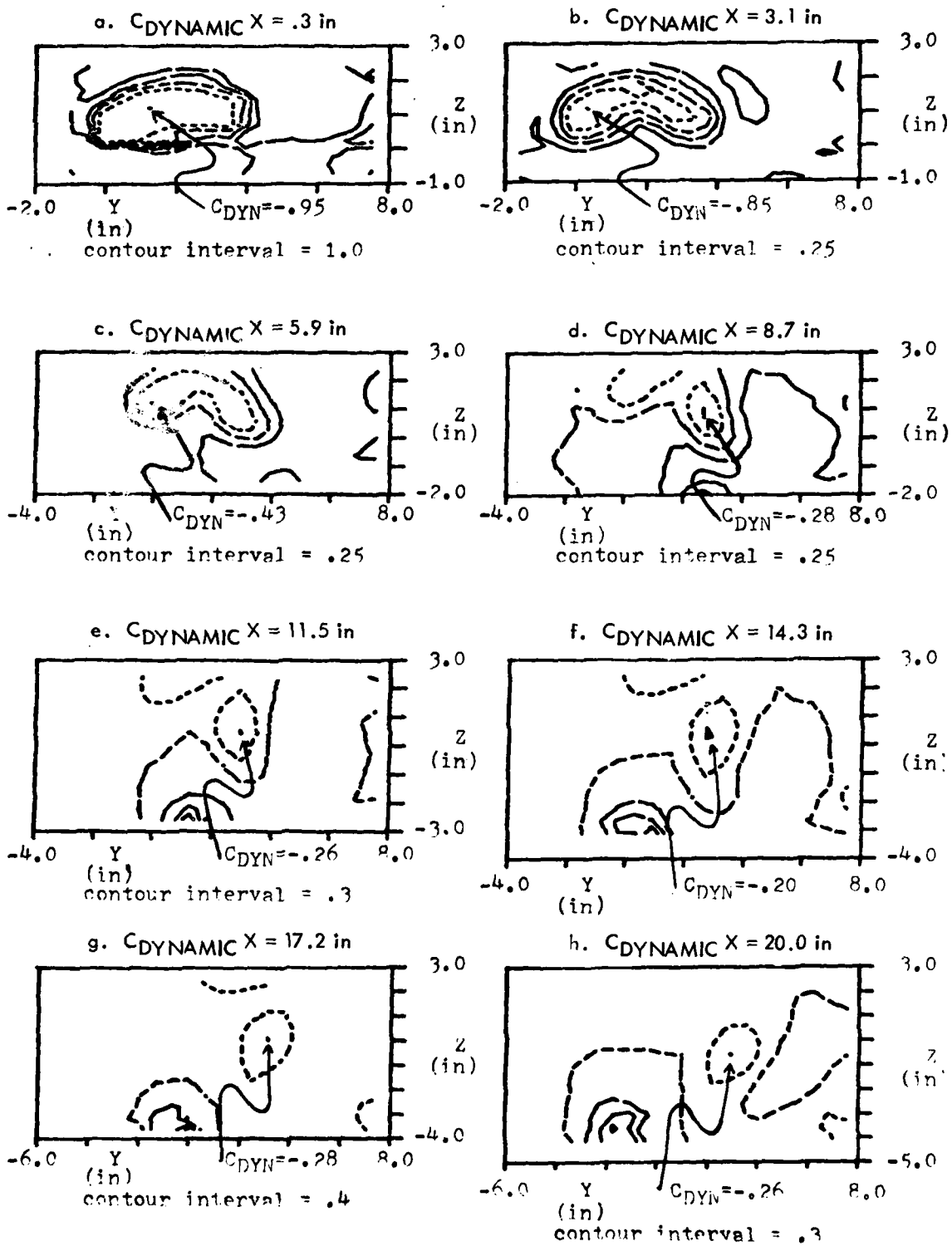


Figure 13. Dynamic Pressure Coefficient

Examining the rest of Figure 12, we see that the major features of the flow are the canard leading edge separation vortex in the center and the wing separation vortex below it. A third feature that deserves comment is the shape of the static pressure contours outboard of the vortices, which is essentially a series of parallel lines. This means the flow velocity inboard is higher than outboard in a regular fashion. This is due to the induced flow field of the 60-degree swept wing. The inboard portion of each figure is above the wing surface while the outboard portion is in front of the leading edge. We expect the velocity above the wing to be higher than the induced velocity in front of the leading edge.

The local dynamic pressure is presented in Figure 13 as contour plots of the dynamic pressure coefficient. Since this coefficient is simply the difference of the total and static pressure coefficients, it shows the features of both. Figure 13a illustrates the effect of the linear canard wake ridge observed in Figure 12a. The high and low "static pressure doublet" causes only very slight modification to the upper right side of the total pressure structure of Figure 11a. Figures 13b through 13h behave as expected.

Two other canard wakes were mapped with the canard at 0 inches and 2.75 inches above the plane of the wing. Since these wakes gave very similar results to the middle canard, we will summarize the total pressure data by giving the coordinates of the canard leading edge separation vortex and tip vortex in Tables 2 and 3. The origin of the coordinate system for all three tables is the same.

Table 2
CANARD VORTEX CENTER LOCATION

LOW CANARD ALPHA = 11°				
X	TIP		SEPARATION	
	Y	Z	Y	Z
.3	.4	-.3	2.1	0.0
3.1	.2	-.1	2.1	.3
5.9	0.0	.4	2.2	.3
8.7	.1	.8	2.5	0.0
11.5	.5	1.4	2.7	-.2
14.3	-	-	3.0	-.5
17.2	-1.8	1.8	3.0	-1.0
20.0	-	-	3.0	-1.3

Table 3
CANARD VORTEX CENTER LOCATION

HIGH CANARD ALPHA = 11°				
X	TIP		SEPARATION	
	Y	Z	Y	Z
.2	-1.0	2.3	2.1	2.6
3.1	-.4	2.6	2.5	2.4
5.9	0.0	2.8	2.8	2.1
8.8	-	-	3.0	1.8
11.7	-	-	3.0	1.6
14.6	-	-	3.0	1.6
17.4	-	-	3.0	1.3
20.3	-	-	3.2	1.0

VI. Conclusions

We have documented the development and use of a new technique of conducting flow field surveys using a seven-hole probe. These surveys allow the calculation of most of the important flow field parameters, including local static and total pressures. This technique was used to survey the canard wake of three separate models at subsonic incompressible speeds. Our results allow us to locate the canard wakes passing above the wing surface. They also indicate a possible discrepancy of location of wakes depending on the type of data examined, that is, static, total, or dynamic pressure. The relative accuracy of the method is undetermined as is the resolution limit of the probe and the frequency response of the apparatus. The tests were run only at incompressible flow velocities. Despite these criticisms, a valuable educational and research technique for quantitative flow field visualization has been developed.

References

1. Gallington, R. W. "Measurement of Very Large Flow Angles With Non-Nulling Seven-Hole Probes." Aeronautics Digest - Spring/Summer 1980, USAFA-TR-80-17, USAF Academy, Colorado.
2. Clancy, L. J. Aerodynamics. New York: John Wiley & Sons, 1975.
3. Panton, R. L., W. L. Oberkampf, and N. Soskic. "Flight Measurements of a Wing Tip Vortex." Journal of Aircraft, Vol. 17, No. 4 (1980), Article No. 80-4030.
4. Kulfan, R. M. "Wing Airfoil Effects on the Development of Leading-Edge Vortices." AIAA Paper, 79-1675.

Appendix A

This appendix contains the user instructions for VOLCAL.FTN, TOPWNG.FTN, COEF7.FTN, and SCALAR.FTN. All the left-justified capitalized lines are either responses to or replies from the PDP-11/45 computer.

VOLCAL.FTN USER'S MANUAL

ENTER A HEADING FOR THE GRAPHS GENERATED BY SCALAR.FTN. DESCRIBE THE MODEL CONFIGURATION, THE ANGLE OF ATTACK, AND ANY OTHER DESIRED INFORMATION. MAX LENGTH IS 40 CHARACTERS.

The user now enters a heading such as

ALPHA = 11 MIDDLE CANARD, SWEEPED BACK WING

The computer then prints out what is entered and asks if it is correct. If correct, Y is entered. If incorrect, N is entered and the computer again requests the title information.

ENTER XA, YA, ZA

The computer asks for the X, Y, and Z coordinates for corner point A. Figure A-1 shows the location of points A through H. The dimensions of each coordinate are

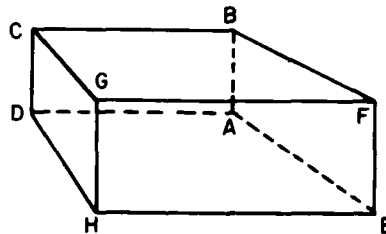


Figure A-1. Measurement Volume

in inches and are referenced to the (0,0,0) point at the outboard tip of the middle canard. Point A is the lower right corner of the volume as referenced to the front of the model.

ENTER XB, YB, ZB

⋮
⋮
⋮
⋮

ENTER XH, YH, ZH

ARE THESE CORRECT? (Y OR N)

If N is entered, the computer asks for the coordinates again.

ENTER THE DESIRED NUMBER OF PLANES OF DATA IN THE X DIRECTION, THE NUMBER OF POINTS DESIRED IN THE Y DIRECTION (OUT THE CANARD TIP), AND THE DESIRED NUMBER OF POINTS IN THE Z DIRECTION, RESPECTIVELY. USE REAL FORMAT.

We used four planes of data in the X direction, 20 points in the Y direction, and 14 points in the Z direction. The input was thus:

USAFA-TR-81-4

4,20,14

The computer then prints out the values entered above and asks if they are correct. If N is entered, then it will go back and ask the above question again. The program now executes to completion.

TOPWNG.FTN USER'S MANUAL

ENTER VOLUME.DAT VERSION NUMBER

The user now enters the version number of VOLUME.DAT that corresponds to the model configuration being tested.

ENTER TEMP, PATM (USE REAL FORMAT)

The user enters the room temperature (°F) and the room pressure (in. Hg). After the temperature and pressure are entered, the computer prints them out and asks if they are correct.

START TUNNEL AND ENTER GO WHEN READY

The user starts the tunnel and enters GO when the air is stabilized at the desired velocity.

ENTER WHAT VELOCITY THE RUN IS AT AND ANY OTHER INFORMATION UP TO A TOTAL OF 20 CHARACTERS LONG YOU WISH TO HAVE IN THE GRAPH TITLE

The user enters something similar to

VEL = +100 FPS

The computer prints out the above and checks if it is correct. If incorrect, the user enters N and the computer asks for it again.

THE NEXT PLANE THAT IS RUN IS AT X = .3. DO YOU WANT TO RUN THIS PLANE OF DATA? IF YOU DO, MOVE THE PROBE TO THE DISPLAYED X VALUE AND ENTER GO. IF YOU WANT ANOTHER PLANE, THEN ENTER NO.

The user acts accordingly. As soon as GO is entered, the program will start taking data. When a plane is completed, the following message is printed out on the screen if there is another plane of data to be taken.

MOVE TRAVERSE MECHANISM TO NEXT X VALUE, X = 3.1.
ENTER GO WHEN READY TO CONTINUE RUN.

As soon as GO is entered, the program takes another plane of data. The computer carriage returns when it completes the last plane of data.

COEF7.FTN USER'S MANUAL

ENTER WNGMAP.DAT VERSION NUMBER

The user enters the version number of the WNGMAP.DAT data file to be reduced.

SCALAR.FTN USER'S MANUAL

DO YOU WANT AN HP-4662 HARDCOPY?

If the user wants a hard copy, he sets up the 4662 printer with the paper, defines the borders (if needed), and enters Y. N is entered if the user wants the graph

USAFA-TR-81-4

displayed on the screen.

ENTER CONTUR.DAT VERSION NUMBER

The user enters the corresponding version number of the plane of data to be displayed.

ENTER VALUE FOR Z COORDINATE DATA

1 CA
2 CB
:
:
:
:
:
13 CDYN

The user enters the number of the data to be displayed.

ENTER A1,A2,A3,S1,S2,S3

The user enters 0, 120, 90, .4, .4, .4, 1 if an axonometric projection is desired or 0, 90, 0, .4, .4, .4 if a contour projection is desired. The three .4's are the scaling factors. Changing these will change the size of the graph.

If a contour projection is selected, the computer will print out:

ZMIN	ZMAX	INC
-1.235	.243	.215

DO YOU WISH TO CHANGE LIMITS?

If more or less intervals are desired, the user enters Y. If the given intervals are satisfactory, N is entered. If Y is entered, the computer will print out:

ENTER ZLOW, ZMAX, ZINC

The user now enters the required information such as

-1.2, .2, .3

The program now plots the graph either on the terminal screen or on the 4662 flat bed pen plotter.

EXAMINING A RULE OF THUMB FOR THE RELATION BETWEEN
CAMBER AND ZERO-LIFT ANGLE OF ATTACK

E.J. Jumper*

Abstract

This paper examines the rule of thumb that states that an airfoil's zero-lift angle of attack is roughly equal in degrees to minus the magnitude of the percent camber. The examination consists of looking at coefficient-of-lift versus angle-of-attack curves for selected NACA airfoils and comparing this experimentally-determined zero-lift angle-of-attack data with that predicted by the rule of thumb. Thin-airfoil theory is also employed to examine the validity of the rule. Finally, the paper presents an example of how the rule can be used to help interpret data by relating the rule's use in interpreting wind tunnel data obtained for a Kline-Fogleman airfoil.

I. Introduction

In engineering disciplines there are certain relationships that hold in such a general way that they are referred to as rules of thumb. As Webster would define it, a rule of thumb is a general principle regarded as roughly correct and helpful but not intended to be scientifically accurate. In this paper I am going to examine a rule of thumb I found in an introductory aerodynamics text by Clancy (Ref. 1). This rule of thumb states that an airfoil's zero-lift angle of attack is roughly equal in degrees to minus the magnitude of the percent camber.

Figure 1 shows a typical coefficient-of-lift, C_l , versus angle-of-attack, α , curve for an airfoil with positive camber. Notice that the airfoil must be placed at a negative α before C_l is equal to zero. The angle at which C_l equals zero is called the zero-lift angle of attack, α_{L0} . Referring to Figure 2, camber is the maximum distance from the mean camber line to the chord line. This distance is indicated by z_c in Figure 2. The camber is usually specified as a percent of the length of the chord line, c . Thus, a camber of four percent, for example, would mean that z_c was equal to $0.04c$ and would be considered positive (concave up) unless otherwise stated. Using our rule of thumb and the example of the four-percent camber airfoil, we would expect to find α_{L0} for this airfoil roughly equal to -4 degrees.

A cursory examination of C_l/α data from Abbott and Doenhoff (Ref. 2) for various airfoils seems to verify the rule, but how far can we push it? This paper examines the applicability of the rule by taking a closer look at the Abbott and Doenhoff airfoil data and by examining a theoretical treatment of the effect of camber on α_{L0} using thin-airfoil theory. Finally, the paper presents an example of using the rule as a tool for interpreting experimental data. The example involves looking at a so-called Kline-Fogleman airfoil.

*Major, USAF, Associate Professor of Aeronautics, DFAN

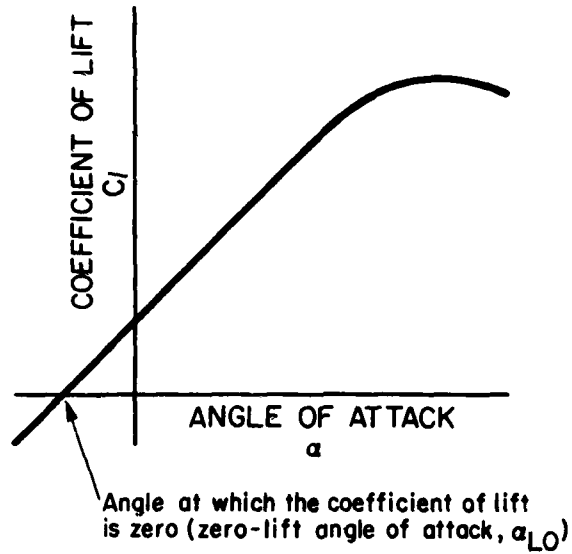


Figure 1. Typical Coefficient-of-Lift Versus Angle-of-Attack Curve for an Airfoil with Positive Camber

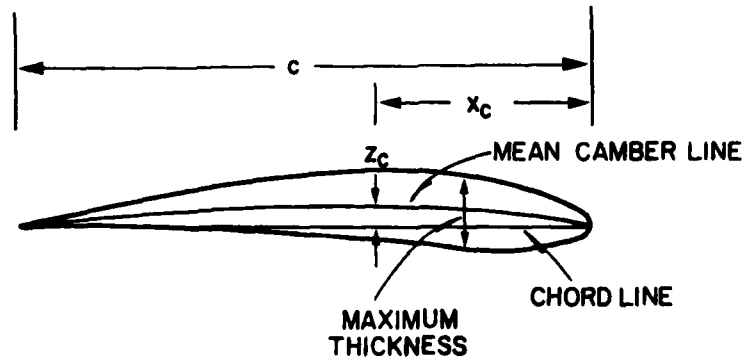


Figure 2. Airfoil Nomenclature

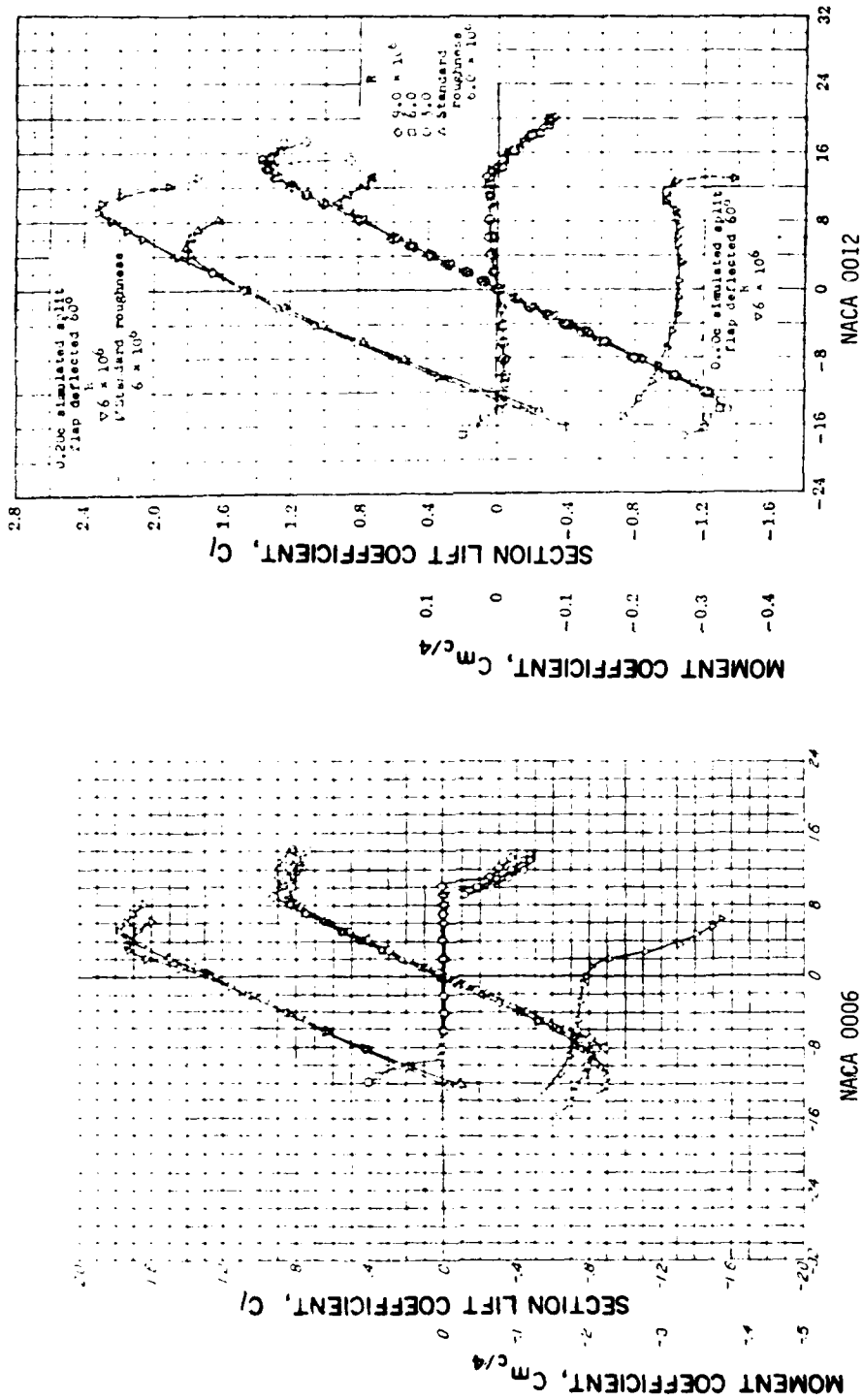
II. Empirical Examination of the Effect of Camber on α_{L0}

The most accessible airfoil data for examining the extent of applicability of the rule of thumb relating camber and α_{L0} is found in Ref. 2. In this reference is a large sample of NACA airfoil data assembled by Abbott and Doenhoff. Of the set of data, the NACA four- and five-digit series are easiest to interpret in terms of determining the camber. In the four-digit NACA series, the first digit gives the maximum camber of the airfoil in percent of the chord (percent camber), the second number gives the location of the maximum camber in tenths of chord, and the last two numbers give the maximum thickness in percent of chord. Thus an NACA 4415 designated airfoil describes a wing section that has a maximum camber of 0.04c, located at 0.4c measured from the leading edge of the airfoil, and a maximum thickness of 0.15c, where c is the chord length. Similarly, in the NACA five-digit series, the first digit again indicates the percent camber, but the next two numbers represent twice the percent of chord of the location of maximum camber, and the last two digits again indicate the thickness. Thus, an NACA 23012 designated airfoil describes a wing section which has a maximum camber of 0.02c, located at 0.15c (.30/2) from the leading edge with a maximum thickness of 0.12c.

If we now look at some coefficient-of-lift (C_l) versus angle-of-attack (α) curves (C_l/α curves) gathered from wind tunnel tests, we can examine the applicability of the rule of thumb. Let us first look at the case of a symmetrical airfoil, that is, one that has no camber. Figure 3 shows two examples of symmetrical airfoils - the NACA 0006 and the NACA 0012 (Ref. 2). As both the rule and common sense would predict, the zero percent cambered airfoil has zero degrees of shift in the zero-lift angle of attack. Now look at Figures 4, 5, and 6 which show C_l/α data for airfoils that have one, two, and four percent camber respectively (Ref. 2). Note that our rule of thumb correctly predicts α_{L0} over a wide range of percent thickness (ranging from 8 percent to 24 percent). One should also note, however, that in all of these cases the location of the maximum camber is at 0.4c.

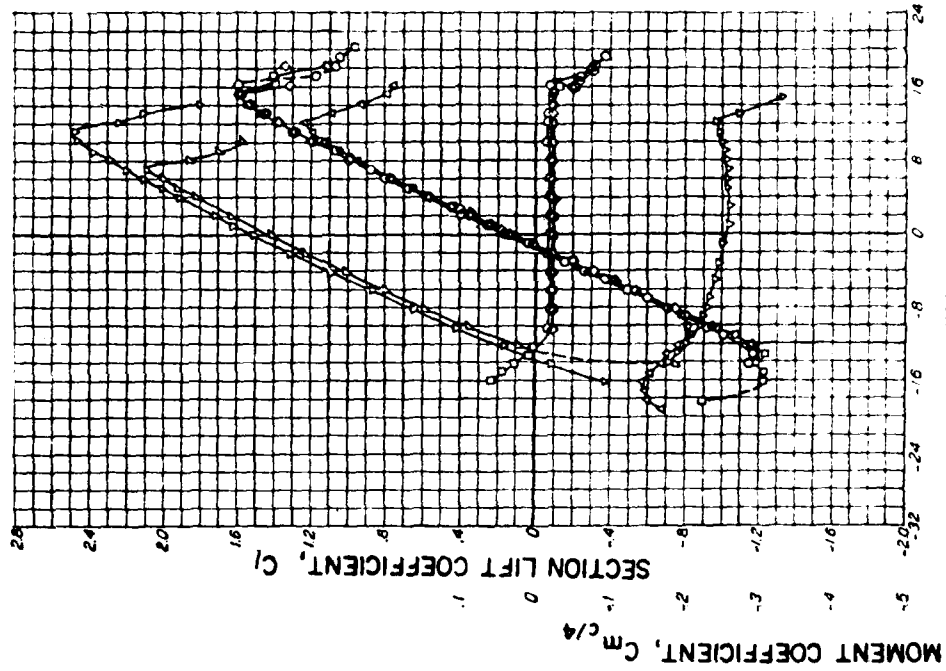
If we examine data from the same source (Ref. 2) at maximum camber locations other than 0.4c, we begin to note some disagreement between the α_{L0} predicted by the rule of thumb and the data. As the maximum camber location moves further forward of the 0.4c location, we see that the rule overpredicts the magnitude of $|\alpha_{L0}|$. For example, Figure 7 shows the effect of moving the maximum camber forward by 0.25c to 0.15c. Here the rule overpredicts the magnitude of $|\alpha_{L0}|$ by 25 percent. For Two-percent camber, the curve shifts to the left only about 1.5 degrees, or about -0.75 degrees/percent, instead of -1.0 degrees/percent predicted by the rule.

To examine the effect of moving the maximum camber aft of the 0.4c location, we must go to airfoil designations which do not indicate camber directly by their number designation. Of the NACA-designated airfoils reported by Abbott and Doenhoff, those with a camber line designation of NACA a = 0 and 0.1, maximum camber occurs at 0.3c for a = 0.4 at 0.4c, for a = 0.5 and 0.6 at 0.45c, and for a = 0.7, 0.8, 0.9, and 1.0

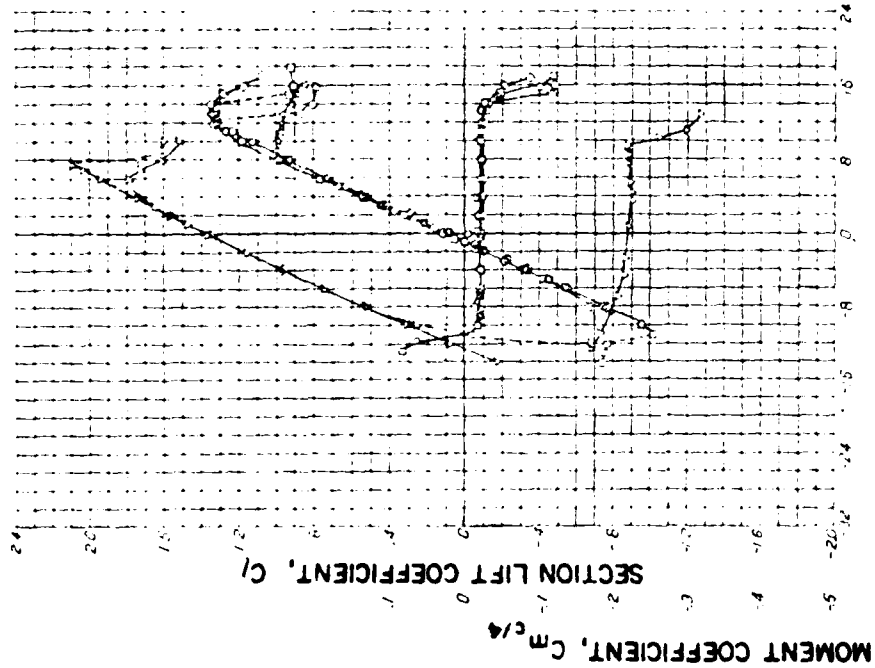


SECTION ANGLE OF ATTACK, α_0 (degrees)

Figure 3. NACA 0006 and NACA 0012



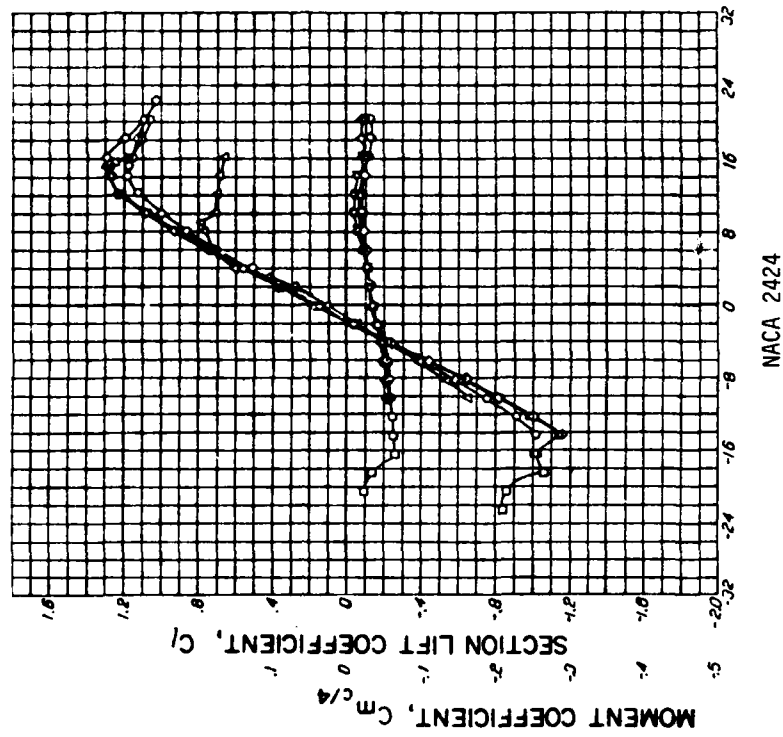
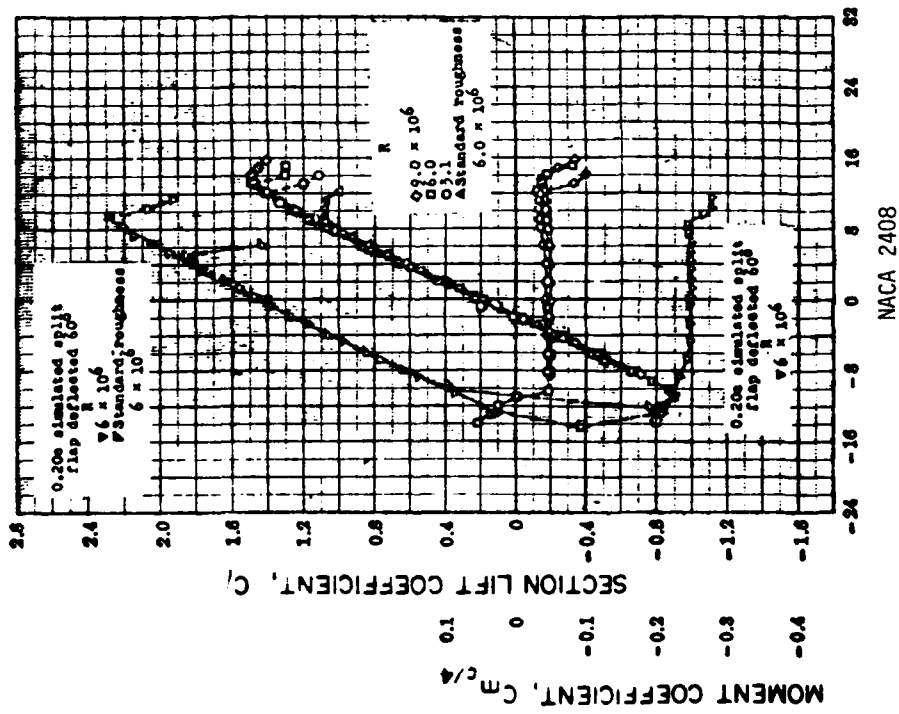
NACA 1412



NACA 1408

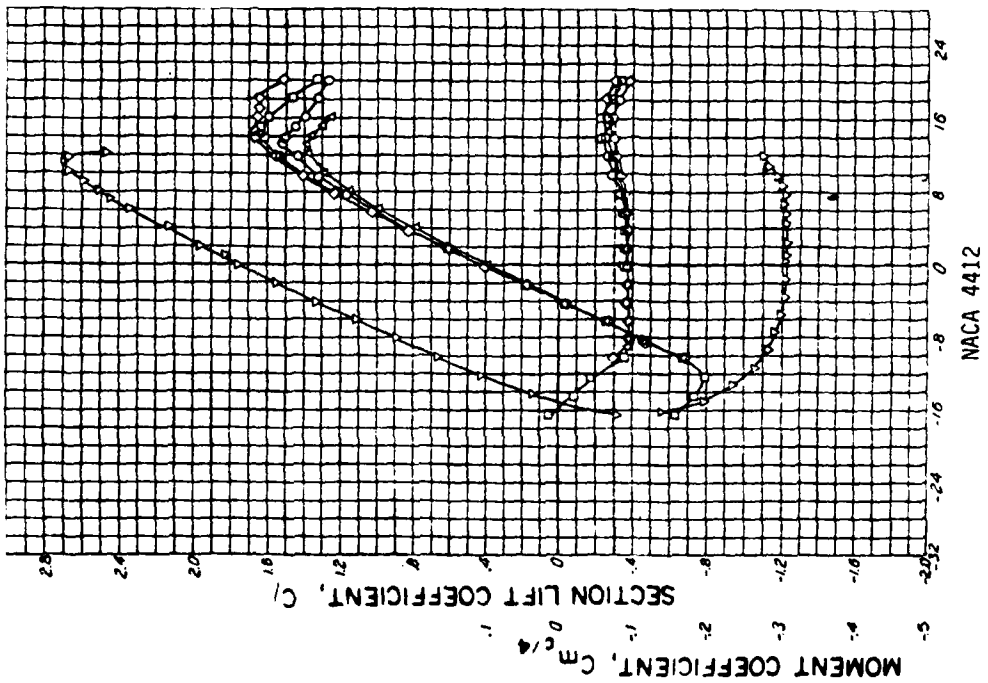
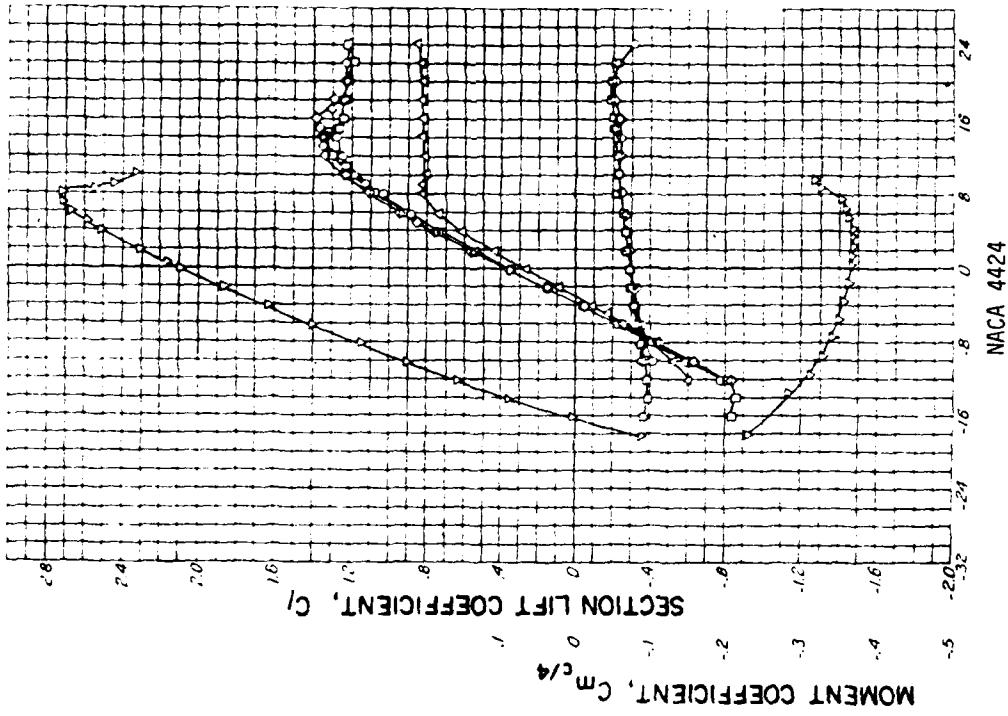
SECTION ANGLE OF ATTACK, α_0 (degrees)

Figure 4. NACA 1408 and NACA 1412



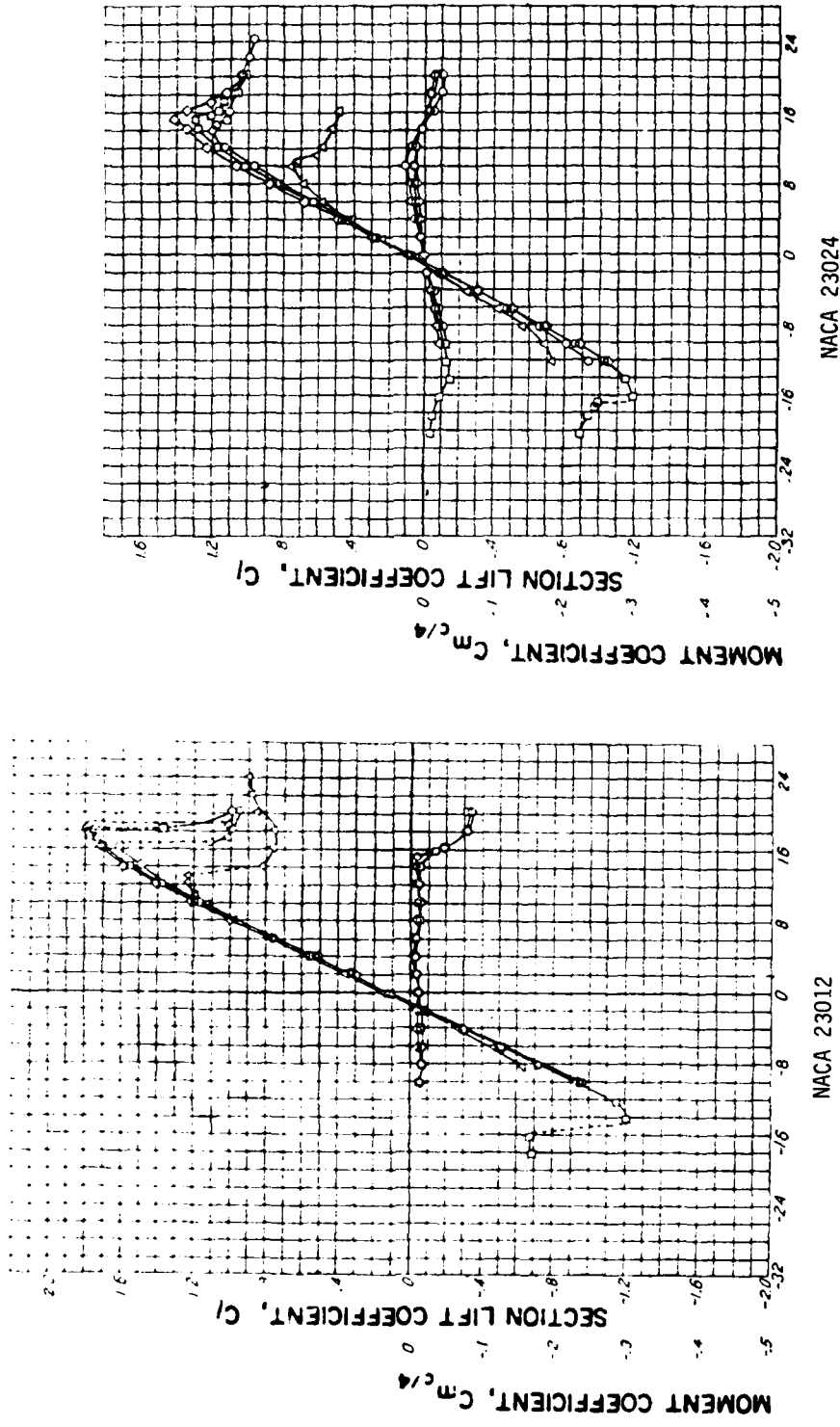
SECTION ANGLE OF ATTACK, α_0 (degrees)

Figure 5. NACA 2408 and NACA 2424



SECTION ANGLE OF ATTACK, α_0 (degrees)

Figure 6. NACA 4412 and NACA 4424



SECTION ANGLE OF ATTACK, α_0 (degrees)

Figure 7. NACA 23012 and NACA 23024

at 0.5c. In the series which have an "a" designation, consisting of a two-digit, subscript-, three-digit number, we have an indirect indicator of the percent camber. Of the last three digits, the first indicates the design coefficient of lift (C_{l_i}) in tenths so that an NACA 65₃ - 212 (a = 0.6) airfoil has a design lift coefficient, C_{l_i} , of 0.2 (the last two numbers are the percent maximum thickness). The "a" designator (i.e., a = 0.6) refers to a specific mean camber line distribution which is enumerated in Ref. 2, based on a design coefficient of 1.0. As mentioned before in the a = 0.6 case, maximum camber occurs at 0.45c, but further, the camber at that point is 0.0737c for C_{l_i} for a design coefficient of 1.0. To get the maximum camber for C_{l_i} 's different than 1.0, one need only multiply the maximum camber for the $C_{l_i} = 1.0$ case by the C_{l_i} in question. Thus, for the example where $C_{l_i} = 0.2$, the maximum camber would be 0.01474c (i.e., 0.2×0.0737) or 1.474 percent.

Using the determination criteria above for camber and location of maximum camber, we can now examine the effect of maximum camber located aft of the 0.4c location. As Figure 8 shows, for zero camber there is zero shift in α_{LO} . Figure 9 shows data for

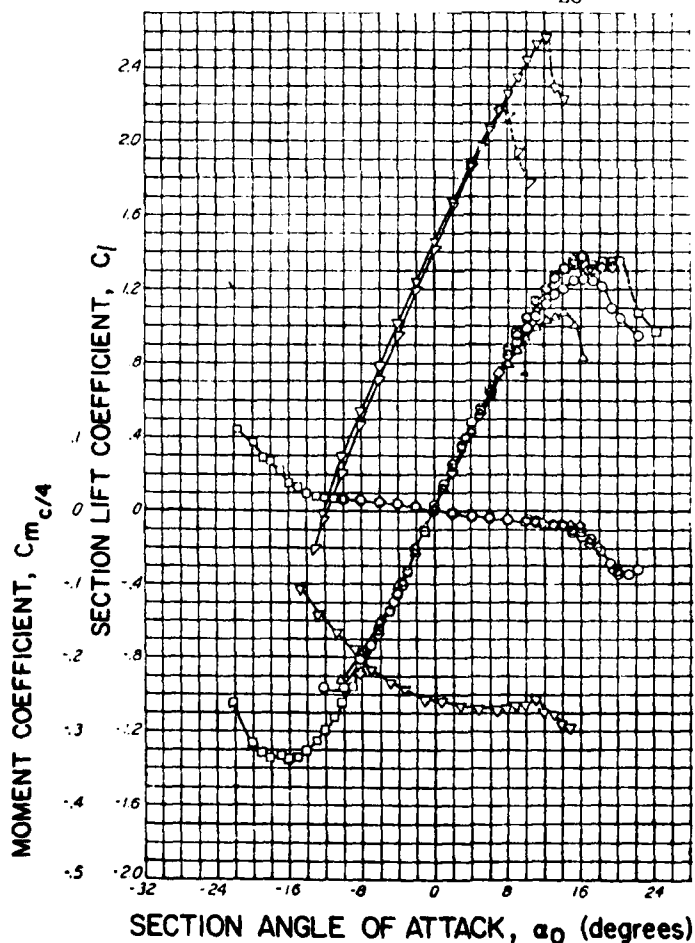


Figure 8. NACA 65₂ - 018 (a = 1.0)

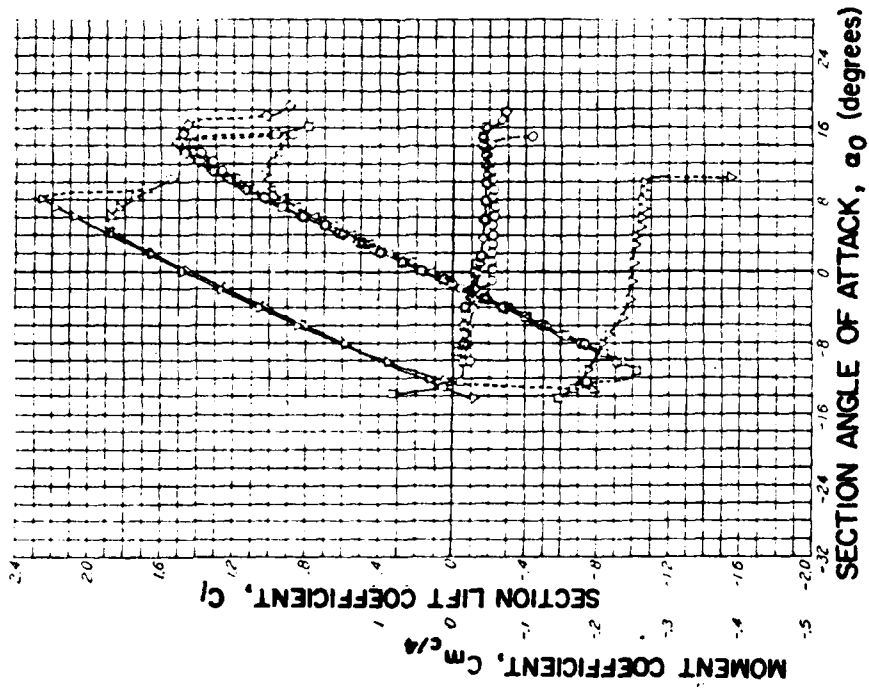


Figure 9. NACA 651 - 212 ($a = 0.6$)

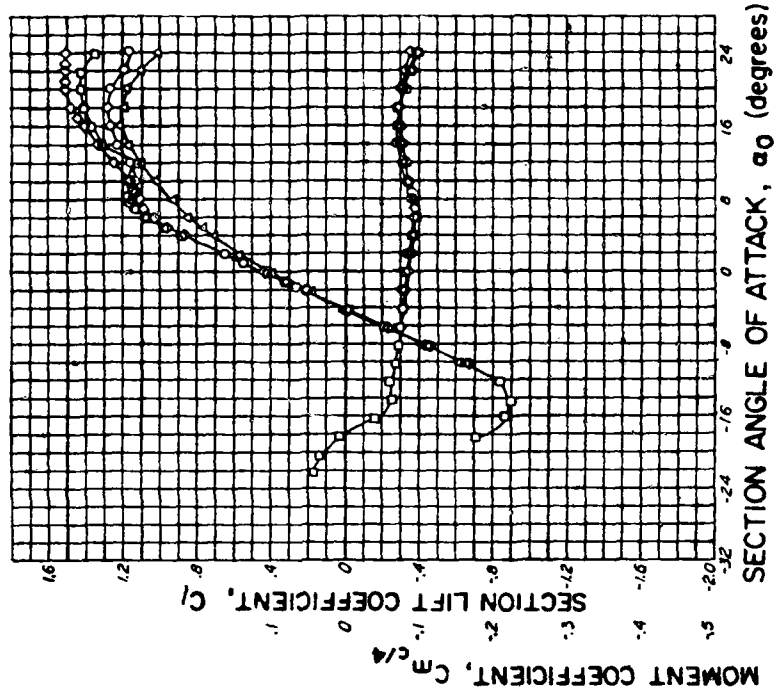


Figure 10. NACA 653 - 618 ($a = 0.5$)

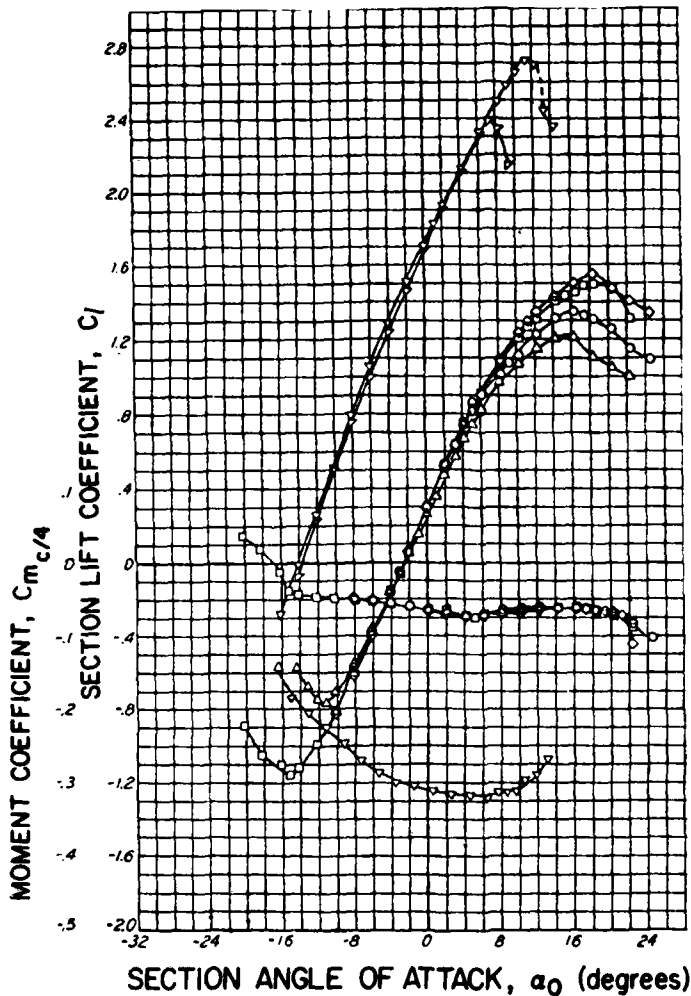


Figure 11. NACA 65₃ - 418 ($a = 1.0$)

1.474 percent camber at 0.45c. Here the rule seems to work. Figure 10 shows data for 4.422 percent camber at 0.45c. Again, the rule applies. Figure 11 shows that for maximum camber at 0.5c and camber of 2.948 percent, the rule still holds.

So, according to data for standard NACA wing sections, the rule seems quite accurate for maximum camber locations between 0.4c and 0.5c from the leading edge, and it appears to be less accurate as the maximum camber point nears the leading edge.

Examination of the data for modified NACA airfoils (Ref. 3) and special airfoils like the GAW(1) (Ref. 4) seem to support the rule of thumb. Further, since these airfoils have maximum camber locations near the mid-chord location, the rule of thumb seems to generally apply for wing sections whose maximum camber is near the mid-chord location. Implications of maximum camber locations further aft are addressed in the next section.

III. Theoretical Examination of the Effect of Camber on α_{L0}

A theoretical examination of the rule of thumb can be made by using thin-airfoil theory. In this theory a wing is represented by a camber line whose distribution is given by z , the distance from the chord line to the camber line, which is a function of x , the distance along the chord line measured from the leading edge (see Figure 12).

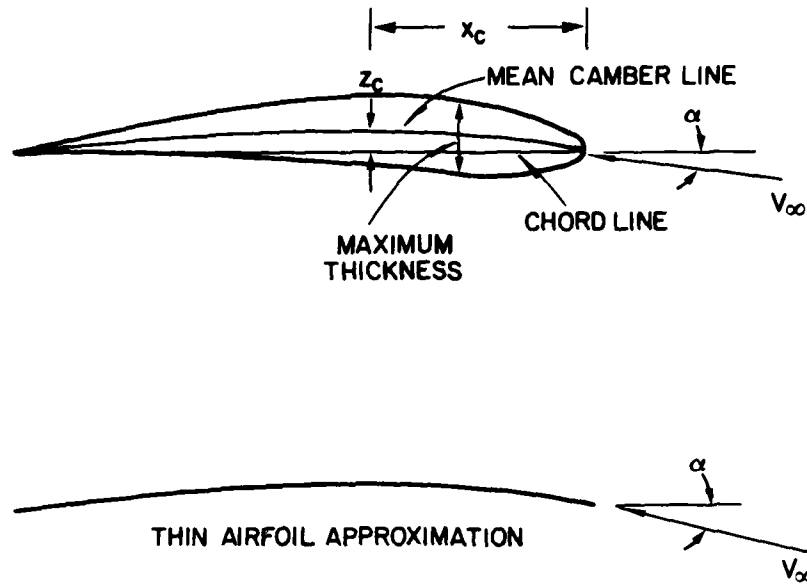


Figure 12. Airfoil Nomenclature and Same Airfoil in Thin-Airfoil Theory

This camber line represents the wing, and the angle of attack, α , is the same angle between the chord line and the relative wing as for the actual airfoil. If we further represent the distance x in terms of a geometric function of a convenient angle θ so that

$$x = \frac{1}{2}c (1 - \cos \theta) \quad , \quad (1)$$

where c is again the chord length; then, according to thin-airfoil theory, the coefficient of lift, C_l , is given by (Ref. 5):

$$C_l = 2\pi \left[\alpha + \frac{1}{\pi} \int_0^\pi \frac{dz}{dx} (\cos \theta - 1) d\theta \right] \quad , \quad (2)$$

where dz/dx is the slope of the camber line at the x location corresponding to θ . Clearly Eqn. (2) tells us that the zero-lift angle of attack, α_{L0} (i.e., the angle of attack

at which $C_l = 0$), must be

$$\alpha_{L0} = -\frac{1}{\pi} \int_0^\pi \frac{dz}{dx} (\cos\theta - 1) d\theta \quad (3)$$

Thus, if we know z as a function of x (thus θ) we can either calculate α_{L0} analytically from Eqn. (3) or, if we are given z in tabular form, we can calculate α_{L0} using an appropriate numerical approximation of Eqn. (3).

The simplest case to examine is the case for a parabolic camber distribution centered at x_c equal to $0.5c$ (the analysis is reproduced here from Ref. 5 for tutorial purposes) so that

$$z = 4 z_c \left[\frac{x}{c} - \left(\frac{x}{c} \right)^2 \right] \quad (4)$$

Eqn.(4) is represented graphically in Figure 13. By changing z_c we can represent all

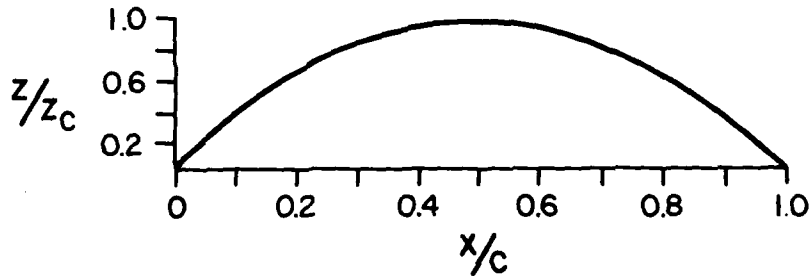


Figure 13. Parabolic Camber Distribution

percent cambers of this camber distribution. The slope of the camber line is obtained by differentiating Eqn. (4):

$$\frac{dz}{dx} = 4 \frac{z_c}{c} \left(1 - 2 \frac{x}{c} \right) \quad (5)$$

or by substituting x in terms of θ by using Eqn. (1):

$$\frac{dz}{dx} = 4 \frac{z_c}{c} \cos\theta \quad (6)$$

If we then substitute Eqn. (6) into Eqn. (3), we have:

$$\alpha_{L0} = -\frac{1}{\pi} \int_0^\pi 4 \frac{z_c}{c} \cos\theta (\cos\theta - 1) d\theta \quad (7)$$

Finally, when we integrate Eqn. (7), we obtain α_{L0} as a function of z_c so that

$$\alpha_{L0} = -2 \frac{z_c}{c} \quad (8)$$

We should keep in mind that Eqn. (8) gives α_{L0} in radians, so that in the generic sense Eqn. (8) tells us that α_{L0} is -1.146 degrees/percent of camber. For this camber distribution then, the rule of thumb is off by only 15 percent.

We can also generically examine the rule of thumb for the NACA four-digit series (on which no wind tunnel data is readily available) by using a crude numerical integration of Eqn. (3). If we assume that the camber line is made up of straight segments arranged according to tabular camber distributions given in Ref. 2, then we can write Eqn. (3) as follows:

$$\alpha_{L0} = -\frac{1}{\pi} \int_0^\pi \frac{dz}{dx} (\cos\theta - 1) d\theta = -\frac{1}{\pi} \sum_{i=1}^n \left(\frac{dz}{dx} \right)_i \int_{\theta_{i-1}}^{\theta_i} (\cos\theta - 1) d\theta \quad (9)$$

or

$$\alpha_{L0} = -\frac{1}{\pi} \sum_{i=1}^n \left\{ \left(\frac{dz}{dx} \right)_i \left[(\sin\theta_i - \theta_i) - (\sin\theta_{i-1} - \theta_{i-1}) \right] \right\} \quad (10)$$

Since Ref. 2 gives the tabular distributions for six-percent camber (all the others are direct-ratio multiples, i.e., four percent would require multiplying all camber values by 4/6), I used these as the generic cases. Using Table I, I computed α_{L0} according to Eqn. (10) for the 62__, 63__, 64__, 65__, 66__, and 67__ distributions. The results were -0.834 degrees/percent, -0.8933 degrees/percent, -0.9633 degrees/percent, -1.039 degrees/percent, -1.138 degrees/percent, and -1.204 degrees/percent for maximum camber at 0.2c, 0.3c, 0.4c, 0.5c, 0.6c, and 0.7c respectively. Notice that the general trend we observed earlier when examining experimental data of decreasing accuracy of the rule as the maximum camber location moved forward is preserved in the theoretical calculations. Further, we can now see that as the location of maximum camber moves aft of the mid-chord, the rule again begins to err. The rule is most accurate between maximum camber locations of 0.4c to 0.6c. Since this is the location of maximum camber for most wings (Ref. 2), it seems the rule is good for most wings.

IV. Applying the Rule of Thumb to the Interpretation of Experimental Data

Some years ago several of my students examined the aerodynamic characteristics of a cusped airfoil (Ref. 6 and 7). At that time an airfoil known as a Kline-Fogleman had appeared in the news as having exceptional aerodynamic characteristics. The Kline-Fogleman airfoil apparently is any airfoil which has a discontinuous lower surface (Ref. 8); the airfoil the students tested was of this classification. The findings were not particularly spectacular or even important, but they did serve to demonstrate the power of using the rule of thumb to interpret trends in data that at first appear somewhat odd.

Table 1 (Ref. 2)
CAMBER DISTRIBUTIONS FOR SELECTED NACA 6--- AIRFOILS

x (percent c)	NACA 62---		NACA 63---		NACA 64---		NACA 65---		NACA 66---		NACA 67---	
	z	dz/dx										
0	0	0.60000	0	0.40000	0	0.30000	0	0.24000	0	0.20000	0	0.17143
1.25	0.726	0.56250	0.489	0.38333	0.369	0.29062	0.296	0.23400	0.247	0.19583	0.212	0.16837
2.5	1.406	0.52500	0.958	0.36667	0.726	0.28125	0.585	0.22800	0.490	0.19167	0.421	0.16531
5.0	2.625	0.45000	1.833	0.33333	1.406	0.26250	1.140	0.21600	0.958	0.18333	0.827	0.15918
7.5	3.656	0.37500	2.625	0.30000	2.039	0.24375	1.665	0.20400	1.406	0.17500	1.217	0.15306
10	4.500	0.30000	3.333	0.26667	2.625	0.22500	2.160	0.19200	1.833	0.16667	1.592	0.14694
15	5.625	0.15000	4.500	0.20000	3.656	0.18750	3.060	0.16800	2.625	0.15000	2.296	0.13469
20	6.000	0	5.333	0.13333	4.500	0.15000	3.840	0.14400	3.333	0.13333	2.939	0.12245
25	5.977	-0.00938	5.833	0.06667	5.156	0.11250	4.500	0.12000	3.958	0.11667	3.520	0.11020
30	5.906	-0.01875	6.000	0	5.625	0.07500	5.040	0.09600	4.500	0.10000	4.041	0.09796
40	5.625	-0.03750	5.878	-0.02449	6.000	0	5.760	0.04800	5.333	0.06667	4.898	0.07347
50	5.156	-0.05625	5.510	-0.04898	5.833	-0.03333	6.000	0	5.833	0.03333	5.510	0.04898
60	4.500	-0.07500	4.898	-0.07347	5.333	-0.06667	5.760	-0.04800	6.000	0	5.878	0.02449
70	3.656	-0.09375	4.041	-0.09796	4.500	-0.10000	5.040	-0.09600	5.625	-0.07500	6.000	0
80	2.625	-0.11250	2.939	-0.12245	3.333	-0.13333	3.840	-0.14400	4.500	-0.15000	5.333	-0.13333
90	1.406	-0.13125	1.592	-0.14694	1.333	-0.16667	2.160	-0.19200	2.625	-0.22500	3.333	-0.26667
95	0.727	-0.14062	0.827	-0.15918	0.958	-0.18333	1.140	-0.21600	1.406	-0.26250	1.833	-0.33333
100	0	-0.15000	0	-0.17143	0	-0.20000	0	-0.24000	0	-0.30000	0	-0.40000

The wing section shown in Figure 14 served as a model for several series of tests. The section was constructed by modifying an NACA 0015 with a vertical cut located at the quarter-chord point and going from the lower surface to the chord line. This cut

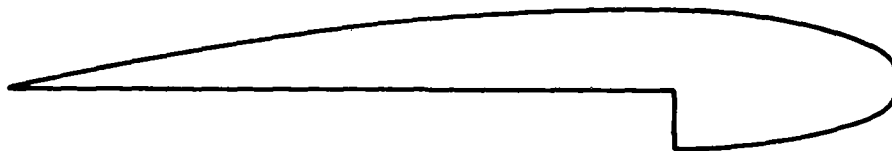


Figure 14. Cusped Airfoil Formed By Modifying an NACA 0015 Wing Section

was joined by a cut from the trailing edge along the chord line. In this paper I will refer to this section configuration as a cusped airfoil. All tests were accompanied by a test of an unmodified NACA 0015 airfoil for comparison purposes.

In these series of tests two types of planforms were used. The first was a finite span on which endplates could be attached. This planform was mounted on a force balance so that aerodynamic forces could be measured directly. Figure 15 shows selected data representative of the coefficient of lift versus angle of attack for this planform.

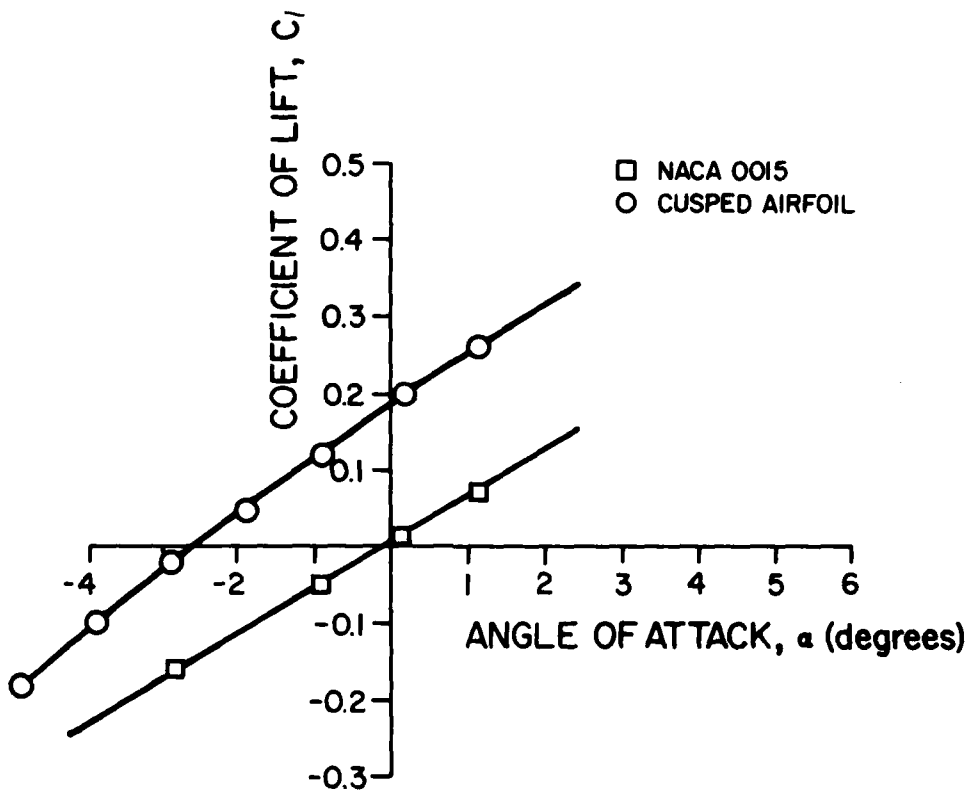


Figure 15. Data for NACA 0015 and Cusped Airfoil with Endplates (Ref. 6)

The second planform spanned the entire width of the wind tunnel so that the data obtained could be interpreted as two-dimensional. Pressure ports located at various points distributed along the chord direction on the upper and lower surfaces of the wing provided the information necessary to plot the coefficient of pressure, C_p , versus chordwise location as distance from leading edge, x , divided by chord length, c , or x/c . By appropriate integration of these plots one of the results we obtained was coefficient-of-lift versus angle-of-attack plots. Figure 16 shows a plot of selected data representative of these data.

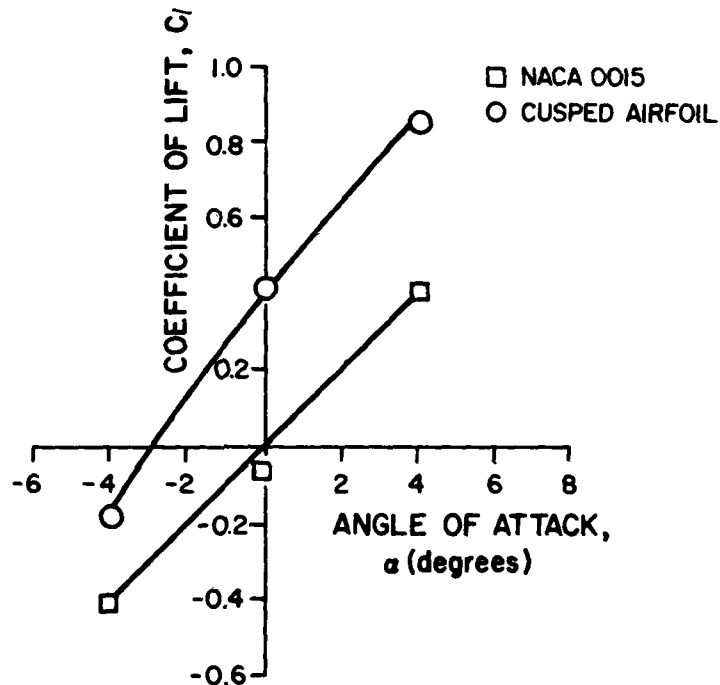


Figure 16. Two-Dimensional Data for NACA 0015 and Cusped Airfoil (Ref. 7)

Rather than interpret Figures 15 and 16 as absolute or definitive, it is instructive to look at what appears to be odd trends, which at first glance seem to defy a simple explanation. If we examine Figure 15 we see that the cusped airfoil has an α_{L0} which is negative. From our own rule of thumb we realize that this implies camber (unless otherwise stated, we mean positive camber when we say camber). In fact, we might even be tempted to say the camber is about 2.7 percent; but for the present let us not speculate on the amount of camber. The supposition that the wing has camber comes as no surprise since the wing actually does have camber. From geometric considerations only, the amount of camber is about 4.5 percent. What is interesting is that the $C_{l/\alpha}$ slope of the cusped wing is steeper than that of the NACA 0015. One might also note that the slope of the cusped wing is not a straight line but rather decreases as α increases (this can be seen most easily by placing a straight-edge along the curve). The slope is only

4.3 per radian, which is not unusual when compared with the two-dimensional limit of 5.7 per radian (2π is the theoretical two-dimensional slope, but in practice we find that the slope is only 5.7). I say not unusual in the sense that we might think that the cusped configuration somehow interferes with the performance of the endplates.

Things become really interesting when we look at Figure 16. First, as a disclaimer of sorts, let me start by admitting the difficulty of obtaining C_l data by integrating C_p versus x/c plots, as evidenced by the value of C_l at $\alpha = 0$ for the NACA 0015 data. So there is bound to be some error bar which I have not included on the plot. However, for the sake of instilling some confidence in the data, let me point out a few positive aspects. First, the plot of the NACA 0015 duplicates the data from Ref. 2 for the same section (which includes the $C_{l,\alpha}$ slope of 5.7 per radian). Second, the zero-lift intercept, α_{L0} , for the cusped airfoil is close to that of Figure 15. Finally, the decreasing slope with increasing angle of attack, noted for the data of Figure 15, is again duplicated in the data of Figure 16. Now let me point out that the slope of the cusped airfoil exceeds the two-dimensional limit! (It is, in fact, as high as 8.2 per radian at $\alpha = -4$ degrees, which exceeds even the theoretical limit of 2π per radian.) One might be tempted to claim we have stumbled on a wing which defies our present understanding of aerodynamics.

Let us see how our rule of thumb might be helpful in interpreting what is actually going on. Figure 17, which is an enlarged portion of Figure 16 with lines added at vari-

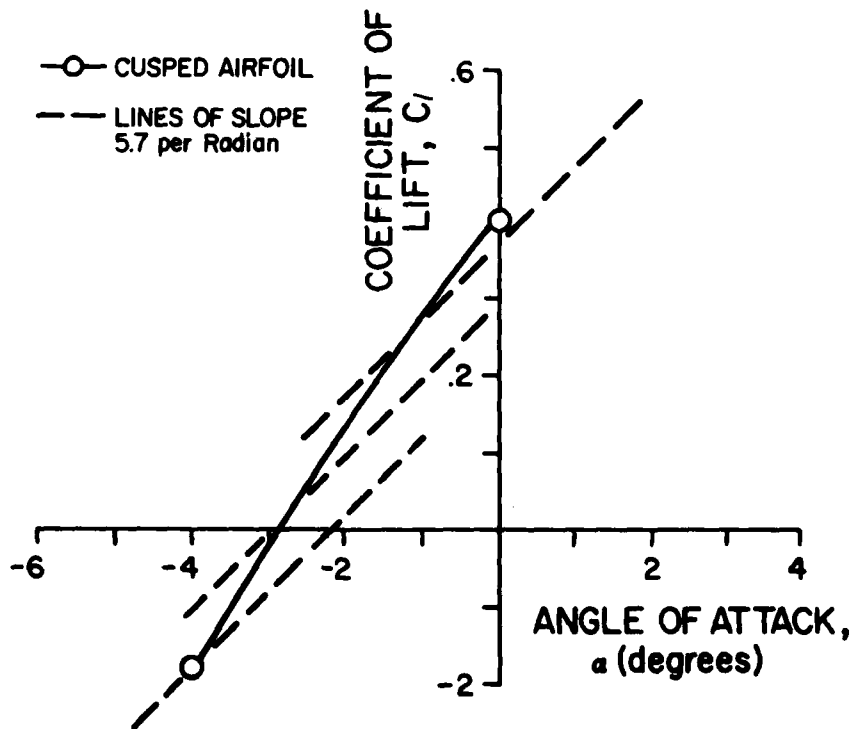
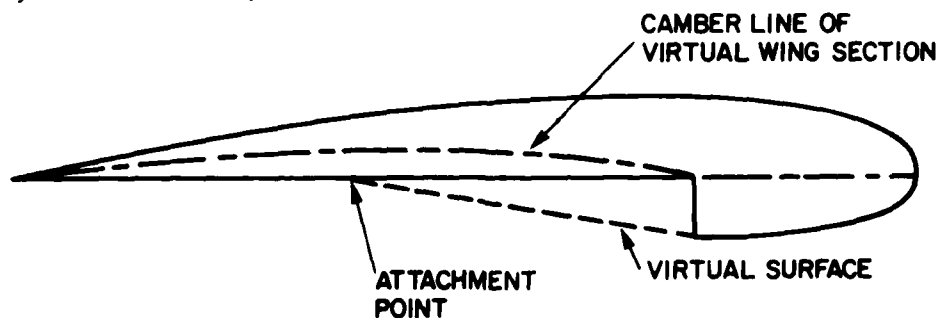


Figure 17. Enlarged Portion of Figure 16 with Lines of Constant Slope Added

ious locations, is helpful in this regard. Each of the additional lines has a slope 5.7 per radian, which is the practical two-dimensional limit. Examining the data presented in Figure 16 in light of our rule of thumb seems to imply that the cusped wing section is acting as a variable camber airfoil, with camber increasing with angle of attack.

Based on this interpretation, we went back to the wind tunnel and located flow re-attachment points by attaching tufts along the chord-wise direction in the cusped region of the wing. Our conclusion was that the attachment point moved forward with increasing angle of attack. If we could interpret the streamline of the attachment point as a virtual wing surface, then the wing was indeed acting as a variable camber airfoil. This explanation seems much more satisfying, and we have a way of checking the validity of the virtual surface interpretation.

Figure 18 shows the attachment point for $\alpha = 0$ degrees. Note also that a line is faired in from the attachment point to the lower surface of the airfoil just at the cut forming the cusp. The actual surface, coupled with the faired line, should approximate the virtual wing section representing the airfoil the potential flow field thinks it is encountering. This new shape allows us to locate the virtual camber line also shown in Figure 18. The maximum camber for the virtual section of Figure 18 is approximately 3.5 percent at $0.6c$. According to our rule of thumb*, this would correspond to an α_{LO} of approximately -4.0 degrees, which in turn would imply a C_l of approximately 0.4 at $\alpha = 0$ degrees. This compares extremely well with our measured C_l at $\alpha = 0$ degrees. Thus the case for assuming a virtual wing section seems well justified. (This experimental justification of using a potential flow solution around a virtual wing section induced by the separated flow region in which we have trapped vortices tends to lend credibility to modeling techniques by Rossow - Ref. 9.)



Maximum camber of virtual wing ~ 3.5 percent located at approximately $0.6c$

Figure 18. Cusped Wing Section Showing Attachment Point for $\alpha = 0$ Degrees with Virtual Wing Section Faired In

*Recall from Section III that for maximum camber located at $0.6c$, the more exact rule is -1.138 degrees/percent, which gives $\alpha_{LO} \cong -4$ degrees.

V. Conclusion

We have examined the rule of thumb which says that the zero-lift angle of attack of a cambered airfoil shifts to the left by approximately the magnitude in degrees of the percent camber. In doing so, we found that the rule can be applied with little error to maximum camber locations of 0.4c to 0.6c measured from the leading edge. Further, we can extend the usefulness of the rule by noting that if α_{LO} exceeds (in magnitude) the rule, then we can assume the maximum camber is located aft of 0.6c; and if α_{LO} is less (in magnitude) than that predicted by the rule, we can assume the maximum camber location is forward of 0.4c. I think it is clear from the example presented here that using the rule of thumb in the interpretation of causes for unexpected (or expected) experimental results can be of great benefit.

References

1. Clancy, L. J. Aerodynamics. New York: John Wiley and Sons, 1975, p. 64.
2. Abbott, I. H. and A. E. von Doenhoff. Theory of Wing Sections Including a Summary of Airfoil Data. New York: Dover Publications, 1959.
3. Hicks, R. M. and E. T. Schairer. Effects of Upper Surface Modification on the Aerodynamic Characteristics of NACA 63.-215 Airfoil Section. NASA TM-78503, 1978.
4. Kohlman, D. L. "Drag Reduction Through Higher Wing Loading." Aeronautics Digest - Spring 1978. USAFA-TR-78-6, USAF Academy, Colorado, July 1978, p. 14-26.
5. Kuethe, A. M. and C. Y. Chow. Foundations of Aerodynamics: Bases of Aerodynamic Design. New York: John Wiley and Sons, 1976.
6. Markl, D. C. and C. V. Spencer. Unpublished laboratory report. Aeronautics Department, USAF Academy, Colorado 80840, December 1978.
7. Bierschback, A. C., Jr. and W. M. Bresley. Unpublished laboratory report. Aeronautics Department, USAF Academy, Colorado 80840, May 1977.
8. Kline, R. Private communication. 9 Oriole Rd., Yonkers, NY 10701.
9. Rossow, V. J. "Lift Enhancement by an Externally Trapped Vortex." AIAA Paper, 77-672. Presented at the AIAA 10th Fluid and Plasma Dynamics Conference, Albuquerque, NM, June 1977.

EXPERIMENTAL AERODYNAMIC EFFECTS OF THREE-DIMENSIONAL
SQUARE CROSS-SECTION MISSILES AT MODERATE ANGLES OF ATTACK

T.R. Yechout*, G.J. Zollars**, and D.C. Daniel***

Abstract

Subsonic aerodynamic force and moment characteristics have been determined for a parametric family of missiles with square cross-sections. The geometric variables considered in this experimental study were body cross-section corner radius, nose planform and fin planform. Data were obtained for missiles with and without fins for angles of attack from 0 to 30 degrees at roll angles of 0, 22.5, and 45 degrees. Surface oil-flow patterns were also recorded. The results clearly show the strong influence of body cross-section corner radius on the aerodynamic forces and moments.

I. Introduction

Recently the possibility of using rectangular or square cross-section bodies as missiles or submunition dispensers has received increasing attention. This interest is due primarily to the increased packing efficiency that results from the rectangular shape as compared to missiles with circular cross-sections. This packing efficiency gain is due to two factors: (1) the ease of packing rectangular modular components and (2) greater useable volume for a given frontal area. What must be determined, however, is whether this well-recognized packing advantage is out-weighed by possible detrimental aerodynamic effects. Unfortunately, only a limited amount of aerodynamic information exists which could support preliminary design or analyses of missiles with square cross-sections, especially those requiring moderate amounts of maneuverability. These limited studies include the two-dimensional work by Pohlhamus (Ref. 1 and 2) and the more recent, very high angle of attack work by Clarkson et al (Ref. 3).

To overcome this data deficiency, the Air Force Armament Laboratory and the Air Force Academy are conducting a two-phase research program to analyze the aerodynamic characteristics of missiles having square cross-sections. The first phase of the program is concerned with measuring the experimental forces and moments on square missile shapes for a wide range of geometries, orientations, and flow conditions. Photographic documentation of surface oil-flow patterns which define the shear stress distribution along the missile surface are also recorded. The second phase of the program is concerned with detailed flow-field measurements. This paper presents partial results from the first phase of the above program. Included is a brief discussion of the wind tunnel facility used in the investigation, information on the wind tunnel models, major force and moment results, representative oil-flow results, and detailed discussion of the results.

II. Wind Tunnel Facility

The data for this investigation were obtained in the subsonic wind tunnel of the

*Major, USAF, Assistant Professor of Aeronautics, DFAN

**Captain, USAF, Instructor of Aeronautics, DFAN

***Associate Fellow AIAA, Research Manager, Air Force Armament Laboratory

United States Air Force Academy (Ref. 4). This facility is a continuous flow, closed-circuit facility which has a test section of two feet by three feet and is capable of operation at a Mach number range of $0.04 \leq M_\infty \leq 0.35$ at atmospheric pressure. At the maximum operating condition, the tunnel is capable of obtaining a unit Reynolds number of 1.6 million per foot. The facility is used for research projects as well as educational experiments and demonstrations.

III. Wind Tunnel Models

The various model components used in this investigation are shown in Figure 1. This figure depicts the four bodies, each with a different cross-section corner radius; the



two noses, a blunted-tangent ogive, and a pointed-tangent ogive; and one each of the three sets of fins that were used. As illustrated by the figure, the four bodies used ranged from perfectly round (B4) to perfectly square (B1). All components were made of aluminum.

The normalized body corner radii (r/b) values investigated were 0.0, 0.1, 0.2, and 0.5. These bodies are depicted in Figure 1 as B1, B2, B3, and B4 respectively. Each body section was 12 inches long and had a width (diameter) of 2 inches.

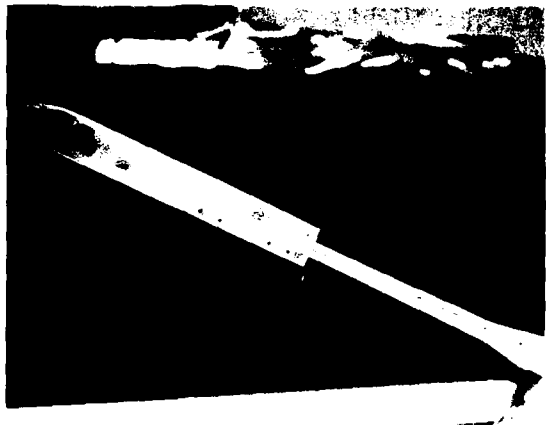
The blunted-tangent ogive nose (N1) shown in Figure 1 was 3 inches in length. The pointed-tangent ogive nose (N2) was 4 inches long.

The three sets of fins were designated as F1, F2, and F3. They had aspect ratios (based on exposed semi-span) of 0.47, 0.67, and 0.34 respectively. Fins F1 and F3 had an exposed semi-span of 1.25 inches and root lengths of 4 inches and 6 inches respectively.

Fin F2 had an exposed semi-span of 1.5 inches and a root length of 3 inches.

The four bodies, two noses, and three sets of fins were used to make various configurations of the missile model. Each configuration was then labeled according to the component nomenclature shown in Figure 1. For instance, the square-body, blunt-nose, and three-inch length fin configuration was noted as BINIF2. An assembled model, mounted in the wind tunnel, is shown in Figures 2a and 2b. As can be seen from Figure 2b, the fins are mounted in a standard cruciform arrangement at the corners of the body.

(a) Finless



(b) Finned

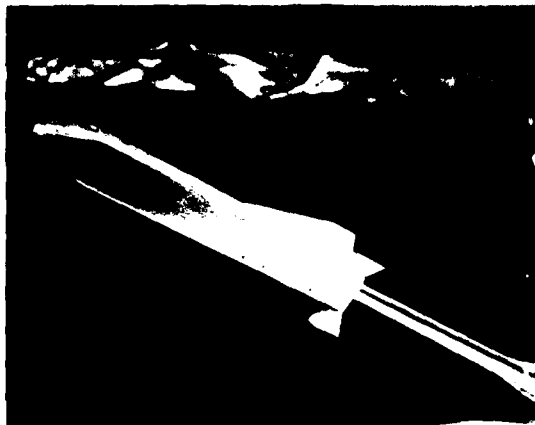


Figure 2. Finless and Finned Wind Tunnel Model

In addition to the models described above, a smaller half-scale version of model N1B3F1 was also fabricated. This model was used for scale comparison experiments in the subsonic wind tunnel, and it also will be used in future experiments to investigate Reynolds number and Mach number effects.

IV. Results

The primary results obtained were six component forces and moments which were taken using an internally-mounted strain gauge balance. The accuracy of the balance was plus or minus 0.5 percent of full load output. It was mounted 6.97 inches forward of the rear of the model (3.428 inches forward in the half-scale model). The aerodynamic force and moment coefficients were calculated using the diameter and area of the circular cross-section body (B4).

The six-component data were taken in two-degree increments from 0 to 30 degrees total angle of attack at roll orientations of 0, 22.5, and 45 degrees. The free stream Mach number was approximately 0.3 for all tests; the unit Reynolds number was approximately 1.3 million per foot for all tests.

The aerodynamic forces and moments on the model without fins were obtained for all nose, body, and orientation combinations. For the model with fins, data were obtained

for configurations using nose N1 and fin F1 with all bodies. All three-fin configurations were also tested using nose N1 and body B3 at all orientation combinations.

In addition to the force and moment data, surface oil-flow patterns were obtained for various body-fin combinations. These data were taken for total angles of attack of 15 and 30 degrees at roll orientations of 0, 22.5, and 45 degrees.

V. Discussion of Results

The results of these wind tunnel tests are presented and discussed in the following paragraphs.

A. Aerodynamic Force and Moment Results

Missile Without Fins: These force and moment results are shown in Figures 3 through 10. Figure 3 shows the variation of normal-force coefficient with angle of attack for each of the four bodies with the blunt nose. As can be seen from this figure,

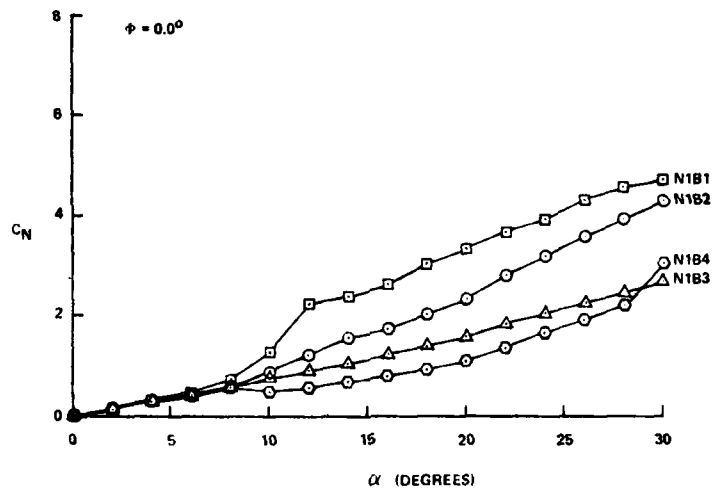


Figure 3. Variation of Normal-Force Coefficient with Angle of Attack for Finless Body

the effects of body cross-section corner radius are very noticeable, particularly above 10 degrees angle of attack. The normal-force coefficient for the body with the perfectly square cross-section (B1) is approximately 125 percent higher than that for the circular body (B4) at 28 degrees angle of attack. It is also interesting to note that at the higher angles of attack the normal-force coefficients of the body with the normalized corner radii of 0.2 (B3) are close in value to the circular body (B4), whereas the values for the body with normalized corner radii of 0.1 (B2) are closer to the perfectly square body (B1). This nonlinear behavior is depicted further in Figure 4, which shows the variation of normal-force coefficient with body corner radius for discrete angles of attack of 10, 12, and 26 degrees.

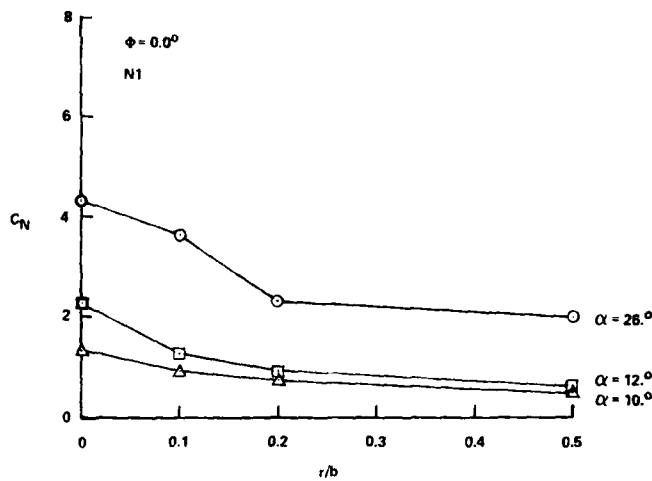


Figure 4. Variation of Normal-Force Coefficient with Body Corner Radius for Finless Body

The body cross-section corner radius also has a slight effect on axial-force coefficient as shown in Figure 5. Here, the axial-force coefficient decreases with increasing corner radius. This is due primarily to the fact that the frontal area is also decreasing with increasing cross-section corner radius.

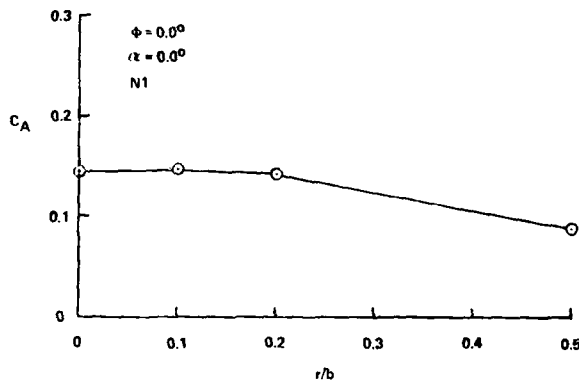


Figure 5. Variation of Axial-Force Coefficient with Body Corner Radius for Finless Body

The variation of side-force coefficient with angle of attack is shown in Figure 6. As would be expected for circular cross-section bodies of the fineness ratio investigated here, there is little evidence of side-force build-up at the higher angles of attack with the exception of body N1B1. This is the perfectly square body ($r/b = 0.0$). It has a side-force coefficient of approximately 0.5 at 30 degrees angle of attack. This value is approximately 10 percent of the normal-force coefficient generated by this body at that angle of attack and is felt to be of little significance.

An interesting scale effect result is given in Figure 7. This figure depicts the

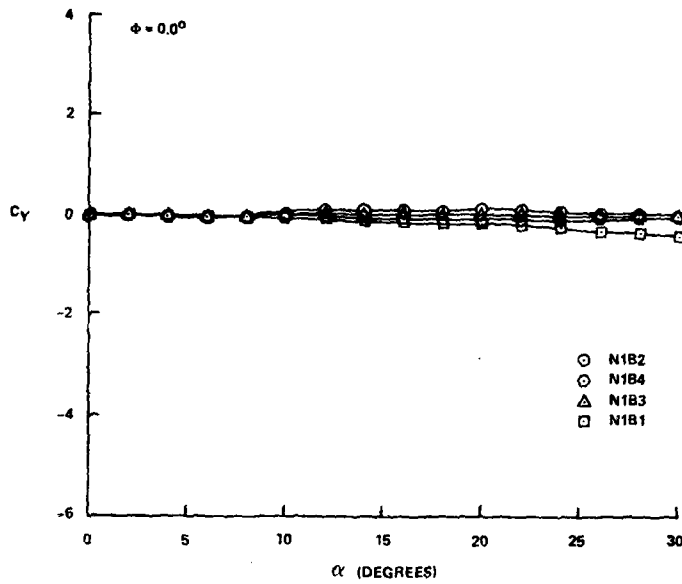


Figure 6. Variation of Side-Force Coefficient with Angle of Attack for Finless Body

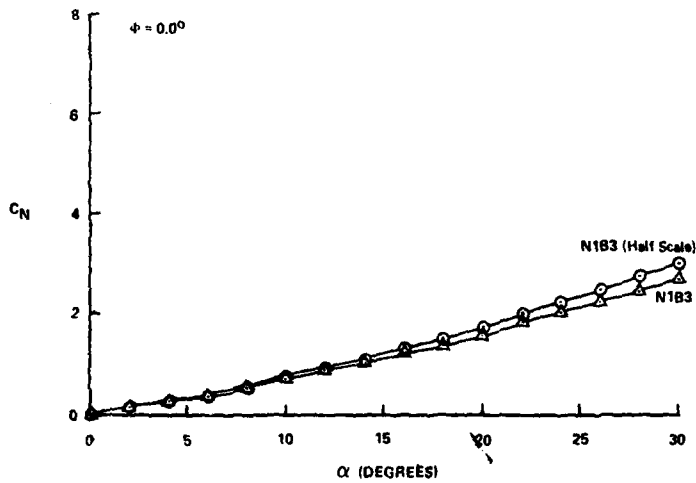


Figure 7. Scale Effects on Normal-Force Coefficient for Finless Body

variation of finless missile normal-force coefficient with angle of attack for body N1B3 and the half-scale equivalent of this body. The normal-force coefficient for the half-scale model is increasingly larger from approximately 6 degrees angle of attack upward. This is probably due to the fact that the separating boundary layer does not scale geometrically as the models do.

Some effects of nose planform on the aerodynamics are shown in Figures 8, 9, and 10. Figure 8 shows the variation in normal-force coefficient with angle of attack for

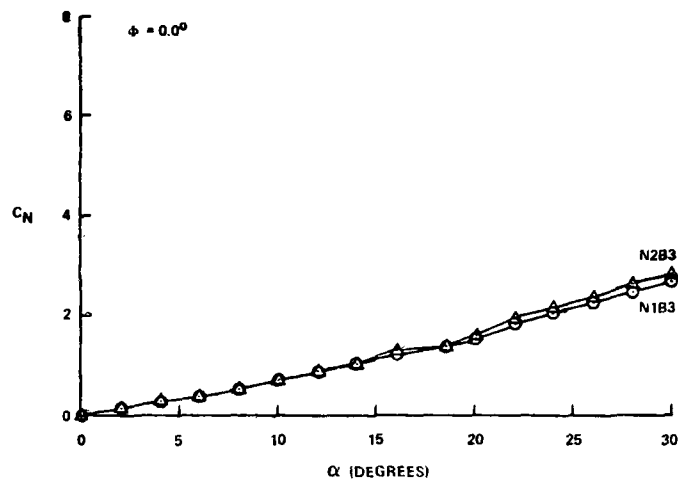


Figure 8. Nose Planform Effects on Normal-Force Coefficients for Finless Body

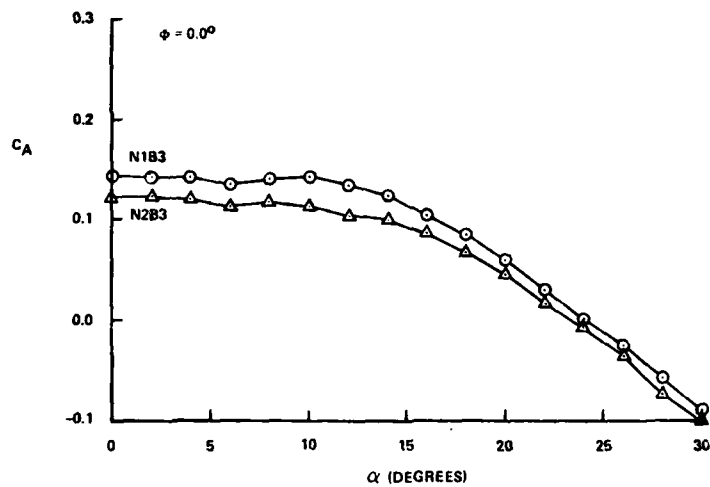


Figure 9. Nose Planform Effects on Axial-Force Coefficient for Finless Body

the blunted- and pointed-tangent ogive noses affixed to body B3. The longer pointed nose results in a slightly higher normal-force at the higher angles of attack. Figure 9 shows the variation in axial-force coefficient with angle of attack for the two noses. The trends are as expected, with the sharp-nosed body having a lower value at zero angle of attack, and the difference between them diminishing as angle of attack increases. Finally, the variation in side-force coefficient with angle of attack for the two noses is shown in Figure 10. There is essentially no difference in the two results.

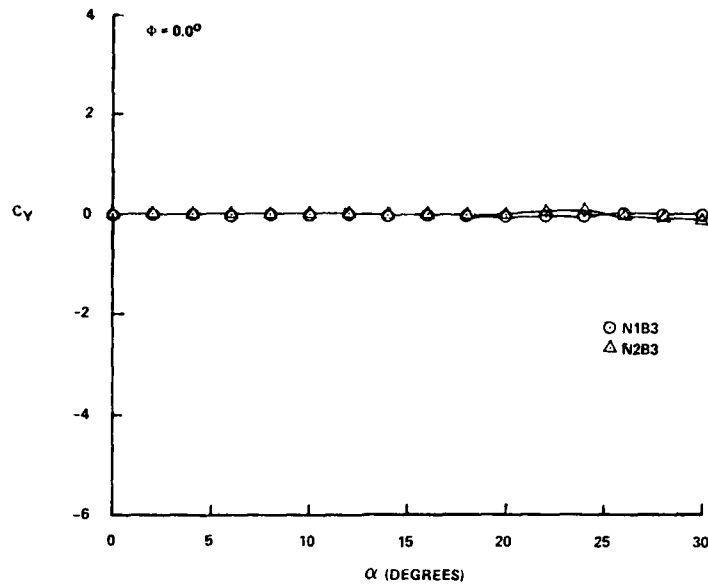


Figure 10. Nose Planform Effects on Side-Force Coefficient for Finless Body

Missile With Fins: The force and moment test results are shown in Figures 11 through 14. Figure 11 shows the variation of normal-force coefficient with angle of attack for each fin combination affixed to the same body. The finless missile values of normal-force coefficient are also shown for reference. As can be seen from the results in Figure 11, the finned combination N1B3F3 produces the highest value of normal-force coefficient for the configurations presented in this figure. This is due to the fact that fin F3 has the largest surface area. Fins F1 and F2, having essentially the same area

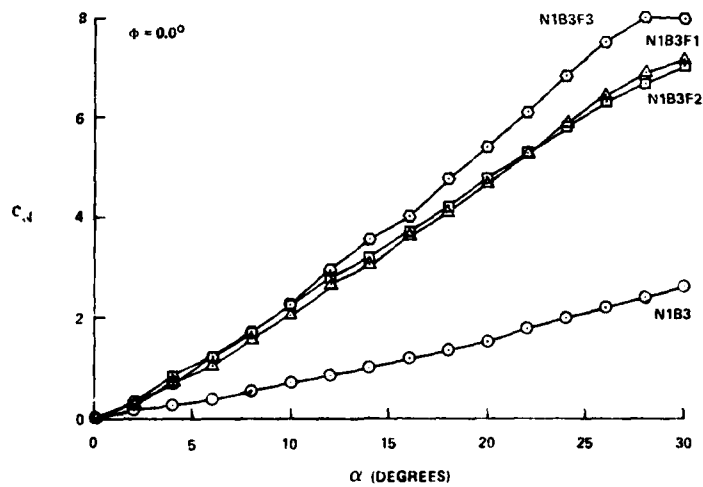


Figure 11. Variation of Normal-Force Coefficient with Angle of Attack for Body B3 with Fins

as each other, produce essentially the same results, albeit lower than F3.

Some interesting effects of the body cross-section corner radius for the missile-with-fins combinations are shown in Figure 12. In this case, results are presented for

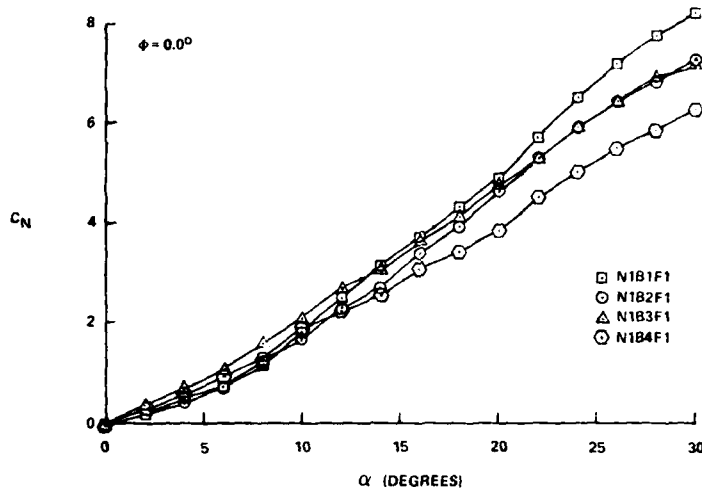


Figure 12. Effect of Corner Radius on Normal-Force Coefficient for Bodies with Fin Set F1

configurations having the same nose (N1) and fins (F1), but affixed to bodies of different cross-section corner radius. As was the case for the finless missile results, the perfectly square body (B1) produces higher values of normal-force coefficient at the higher angles of attack than the other bodies. It is very interesting to note, however, that the variation from body to body is not nearly as pronounced as it was in the finless missile case (Figure 3). The fins, being a major lift-producing device, tend to reduce significantly the effects of corner radius on normal-force coefficient for body-fin

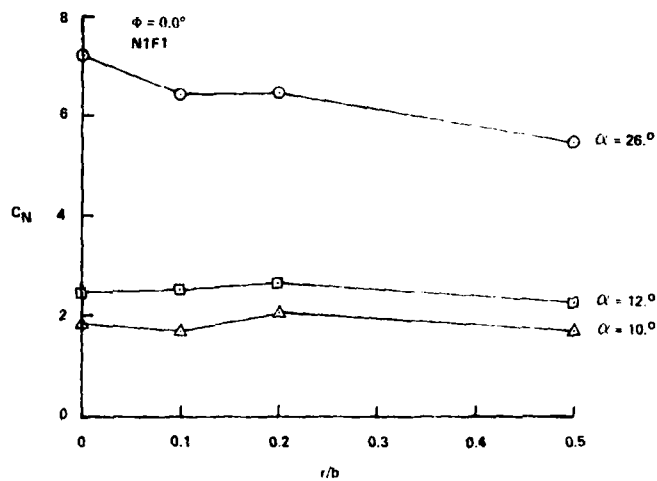


Figure 13. Variation of Normal-Force Coefficient with Corner Radius for Bodies with Fins

geometries. This is demonstrated further in Figure 13, where variations of finned missile normal-force with body cross-section corner radius are shown for three discrete angles of attack.

Rolling-moment test results are presented in Figures 14a, b, and c. These results show the variation in rolling-moment coefficient with total angle of attack for fixed roll angles of 0, 22.5, and 45 degrees. The vehicle geometries considered are again the nose N1 and fins F1 affixed to bodies of different cross-section corner radius. As

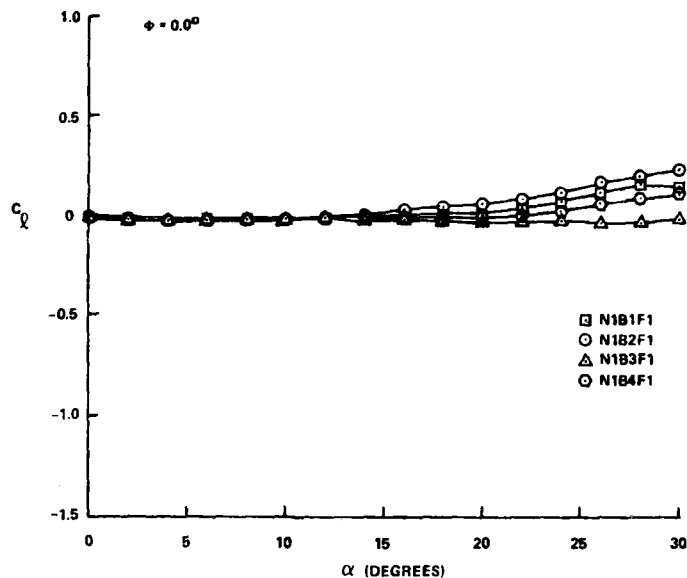


Figure 14a. Variation of Rolling-Moment Coefficient with Total Angle of Attack ($\phi = 0.0^\circ$) for Bodies with Fin Set F1

can be seen from these results, the corner radii have some small effect on the rolling moment at the higher angles of attack when the vehicle has a symmetric roll orientation, i.e., 0 or 45 degrees. The effect for the asymmetric roll orientation ($\phi = 22.5$ degrees), as shown in Figure 14b, is pronounced. For this condition, the rolling moment for the configurations with the more square bodies (N1B1F1 and N1B2F1) is large at the high angles of attack and has a positive sign. The rolling-moment coefficient for configuration N1B3F1, which has a normalized body cross-section corner radius of 0.20, stays near zero throughout the angle of attack range. The configuration with the circular body cross-section, N1B4F1, has a rolling moment completely unlike the others; at the higher angles of attack it has large negative values. This interesting behavior is probably related to flow separation from the model at these high angles of attack and by the immersion of the fins in the leeside body vortices. In fact, as will be shown in the next section, the magnitude of the corner radius does strongly affect the flow separation line(s) on the body, and hence the circumferential location of the body vortices.

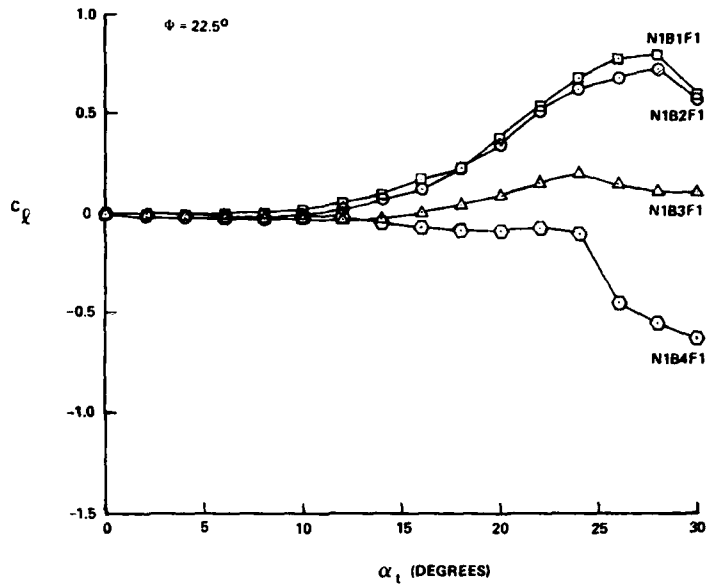


Figure 14b. Variation of Rolling-Moment Coefficient with Total Angle of Attack ($\phi = 22.5^\circ$) for Bodies with Fin Set F1

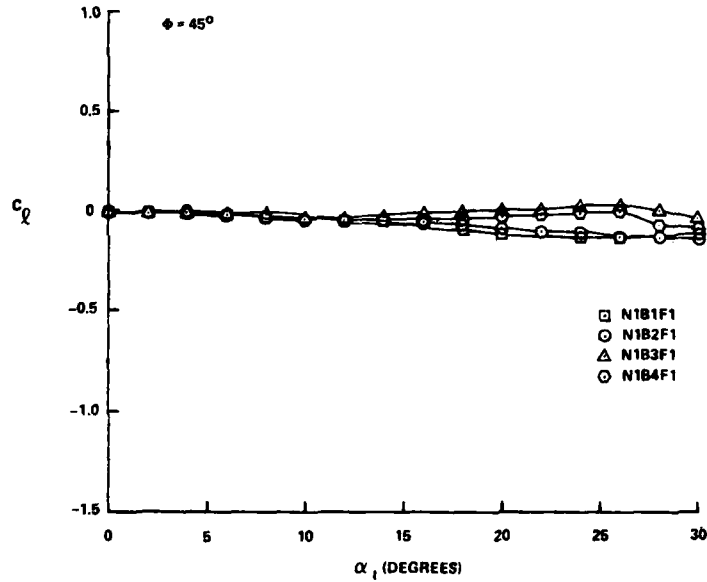


Figure 14c. Variation of Rolling-Moment Coefficient with Total Angle of Attack ($\phi = 45^\circ$) for Bodies with Fin Set F1

B. Surface Oil-Flow Results

Surface oil-flow patterns were obtained for various body-fin configurations during the course of the experiments described in this paper. Some of the more signifi-

cont of these patterns are shown in Figures 15 and 15.

Figure 15 shows the oil-flow patterns that were obtained for the configurations with nose N1 and fins F1 affixed to the four bodies of different cross-section corner radius. The view of this figure is of the side of the model that would have been toward the observer when the wind tunnel test was run. The angle of attack for these runs was 30 degrees. Review of this figure reveals that the separation patterns for configurations N1B1F1 and N1B2F1 (Figure 14a, b) are very similar forward of the fins. The flow



Figure 15. Oil Flow Patterns. (a) $\alpha_t = 30^\circ$, $\phi = 0^\circ$ (N1B1F1);
 (b) $\alpha_t = 30^\circ$, $\phi = 0^\circ$ (N1B2F1); (c) $\alpha_t = 30^\circ$, $\phi = 0^\circ$ (N1B3F1);
 (d) $\alpha_t = 30^\circ$, $\phi = 0^\circ$ (N1B4F1)

seems to separate immediately as it comes around the bottom corners; at that point there is a clearly defined counter-flow region on the side of each configuration, followed by a reattachment line which moves diagonally down the body from the bottom surface, near the shoulder of the nose, to the top surface just in front of the fins. The flow

along the side of configuration N1B3F1 is not at all like that of the first two configurations. In this case, the flow seems to separate and reattach almost immediately as it comes around the bottom corner. The separation pattern for the configuration with the circular cross-section, N1B4F1, is as expected.

Figure 16 shows oil-flow patterns that were obtained for the same configurations and total angle of attack as above, but for a roll angle of 22.5 degrees. The side of the model that is shown in this figure was photographed at the completion of the test after the model had been rolled 157.5 degrees to facilitate the photography. To help eliminate confusion, a schematic of the cross-flow plane during and after the experiment is shown in Figure 17. It can be seen from Figure 16a and b that these two bodies again create very similar separation patterns. From this one would expect the rolling moments for both of these models to be very similar. As was shown previously in Figure 14b, that

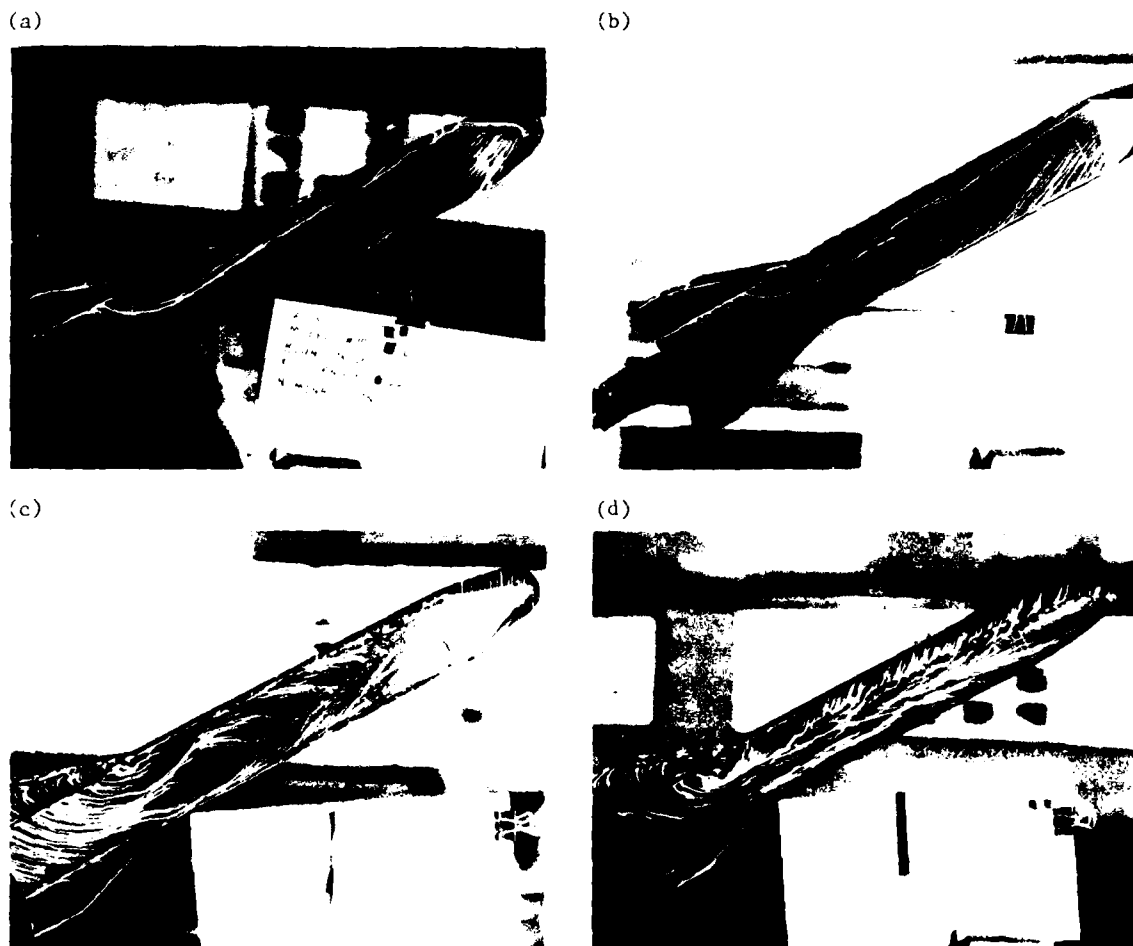


Figure 16. Oil Flow Patterns. (a) $\alpha_L = 30^\circ$, $\beta = 22.5^\circ$ (N1B1F1);
 (b) $\alpha_L = 30^\circ$, $\beta = 22.5^\circ$ (N1B2F1); (c) $\alpha_L = 30^\circ$, $\beta = 22.5^\circ$ (N1B3F1);
 (d) $\alpha_L = 30^\circ$, $\beta = 22.5^\circ$ (N1B4F1)

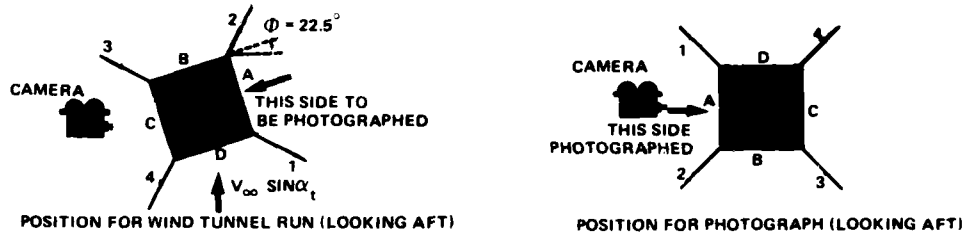


Figure 17. Roll Orientation for Oil Flow Patterns ($\phi = 22.5^\circ$)

is the case. The separation pattern for configuration N1B3F1, as shown in Figure 16c, is quite different from the first two configurations. The separation line is not nearly as clearly defined and appears to have moved further around the body. The net result as shown in Figure 14b is a near-zero rolling moment. This could be due to the fact that the body vortex essentially passes between fins 1 and 2 as shown in Figure 17. The final oil-flow results are shown in Figure 16d for the configuration with the circular cross-section. Here the typical twin separation lines appear for bodies of this type. This totally different separation pattern has resulted in completely different rolling moment characteristics for this body at this particular orientation. This is no doubt due to completely different fin loadings that resulted from the shift in the separation lines.

VI. Conclusion

Aerodynamic force, moment, and oil-flow results have been presented for a parametric family of missiles with square cross-sections. Particular attention has been given to the effects of body cross-section corner radius. This parameter has been shown to have a very strong effect on finless missile normal-force coefficient and a lesser, but still noticeable effect on finned missile normal-force coefficient. Body cross-section corner radius was also shown to have a strong effect on the circumferential location of the flow separation line on the body at combined-roll and high angle-of-attack orientations. The location of this separation line can in turn affect both the magnitude and sense of the rolling-moment coefficient.

The results presented in this paper are part of a continuing research program devoted to aerodynamics of missiles with square cross-sections. Future research will emphasize Reynolds number effects and flow-field measurements.

VII. Acknowledgements

The authors wish to express their appreciation to Mr. Paul R. Mackin and Mr. Scott R. Swinsick for their assistance in preparing the figures used in this paper. We are also indebted to our colleagues: Captain Thomas Bolick and Captain Glynn Sisson, who provided software support; and Mr. Charles Meadows, Mr. Claude Hollenbaugh, and Mr. Fred Jane, who provided technical support in conducting this experiment.

Symbols

b	Body Cross-Section Width (Square Missile) Body Cross-Section Diameter (Round Missile)
C_A	Axial-Force Coefficient
C_N	Normal-Force Coefficient
C_Y	Side-Force Coefficient
C_l	Rolling-Moment Coefficient
C_m	Pitching-Moment Coefficient
C_n	Yawing-Moment Coefficient
M_∞	Free Stream Mach Number
r	Body Cross-Section Corner Radius
V_∞	Free Stream Velocity
α	Angle of Attack
α_t	Total Angle of Attack
ϕ	Roll Angle

References

1. Pohlhamus, E. C., E. W. Geller, and K. J. Grunwald. "Pressure and Force Characteristics of Noncircular Cylinders as Affected by Reynolds Number with a Method Included for Determining the Potential Flow About Arbitrary Shapes." NASA TR R-46, 1959.
2. Pohlhamus, E. C. "Effect of Flow Incidence and Reynolds Number on Low-Speed Aerodynamic Characteristics of Several Noncircular Cylinders with Applications to Directional Stability and Spinning." NASA TR R-29, 1959.
3. Clarkson, M. H., G. N. Malcolm, and G. T. Chapman. "A Subsonic, High Angle-of-Attack Flow Investigation at Several Reynolds Numbers." AIAA Journal, Vol. 16, No. 1, January 1978, pp. 53-60.
4. "Subsonic and Trisomic Wind Tunnel Facilities." Department of Aeronautics, United States Air Force Academy, Colorado 80840.

USAFA-TR-81-4

SECTION II

Instrumentation and Hardware

CALIBRATION OF SEVEN-HOLE PROBES
SUITABLE FOR HIGH ANGLES IN SUBSONIC COMPRESSIBLE FLOWS

A.A. Gerner and C.L. Maurer*

Abstract

This paper illustrates, by example, a method for calibrating seven-hole probes to measure local total and static pressures and relative flow angles of up to 70 degrees in subsonic compressible flows. To conserve air in our blowdown wind tunnel, we used the method of Latin Squares to statistically sample a large and otherwise unmanageable data set, thereby reducing to a minimum the number of data points required to construct a polynomial fit to the data. The three-variable third order polynomials found to represent the probe calibration permit all the desired output quantities to be found explicitly from pressures measured on the probe in an unknown flow field. This method determines the flow angle to within ± 2 degrees with 95 percent certainty.

I. Introduction

Many present and future aircraft designs are beginning to employ such devices as leading-edge strakes, forward-swept wings, and canards. These devices have demonstrated the potential for enhancing aircraft maneuverability and control by producing strong vortices. Some modern aircraft, such as the Concorde, actually rely on vortices and complex flows to create lift. However, in some instances, primary and secondary vortices can interact unfavorably, causing separation and loss of lift on portions of a wing. To be sure, these vortex-laden flow fields are quite intricate and difficult to analyze. Flow visualization techniques offer a way to gain insight into vortex interactions, but suffer from their inability to provide quantitative information. To overcome this limitation, small probes can be inserted directly into the flow stream to gather meaningful pressure information. Historically, non-nulling five-hole probes have been used to determine local total and static pressures at a particular point in a flow, as well as flow directions up to 40 degrees relative to their axis. Nevertheless, it is not inconceivable for the local flow angles of strong vortices to exceed 60 degrees. For this reason, the Air Force Academy, under a grant from NASA-Ames, has developed a unique seven-hole probe. In addition to local total and static pressure measurements, these probes have demonstrated the ability to determine flow angles up to 80 degrees relative to their axis. When combined with a computerized data acquisition system, they are capable of taking data at a rate of nearly two data points per second, much faster than nulling probes which require considerable time to balance probe tip pressures before each pressure measurement can be taken.

In addition, these probes are very small (about one-tenth of an inch in diameter), so they do not significantly disturb the flow they are measuring. But because of this small size, they suffer from inherent manufacturing defects. As a result, each probe must be calibrated before it can be a useful measuring device. Gallington describes such a calibration procedure (Ref. 1) which is both fast and effective, but is only valid

*Cadets, USAF Academy

for incompressible flows. This constraint effectively restricts the probes to surveying flows with free-stream Mach numbers of 0.3 and below (Ref. 2). However, the mere presence of a body in an airflow causes the flow to accelerate in certain regions, resulting in local velocities greater than the free-stream velocity. In addition, local flow velocities in vortex fields are likely to exceed those of the free stream too. As a result, even though the free-stream conditions are slow enough to justify an incompressible flow assumption, the local flow conditions might in fact be compressible. The purpose of this report then is to develop a power series calibration scheme which accurately determines the actual flow conditions from pressures measured on the probe in compressible flows.

Because of the similarities in compressible and incompressible theory, we begin our discussion by developing fully the incompressible calibration theory. Then, by analogy, we expand this theory to obtain the desired form of the calibration suitable for compressible flow. Next, we describe the apparatus and procedures we used to calibrate a probe in subsonic compressible flow, and finally, we discuss the results of that calibration.

II. Incompressible Flow Theory

To simplify our discussion on the calibration of seven-hole probes in compressible flow, we will begin with a background in the theory of incompressible flow calibrations. Much of the information presented in the following sections is drawn from the work of Gallington (Ref. 1). Readers wishing further information on the theory of incompressible probe calibrations are highly encouraged to consult this reference.

Axis System for Low Flow Angles

To begin our discussion of calibration theory, we restrict our treatment to low flow angles; typically, those values for which the angle between the velocity vector of the flow stream and the probe's axis are less than 30 degrees. The more familiar reference system for low flow angles measures velocity vectors in terms of the angle of attack, α , and the angle of sideslip, β . However, in choosing our reference system, we adopted the tangential reference system illustrated in Figure 1. In this system, α_T is taken to be the projection on the vertical plane of the angle between the velocity vector and the probe's axis. And to preserve symmetry, β_T is defined as the projection on the horizontal plane of the angle between the probe's axis and the relative wind. For this reason, the tangential reference system differs slightly from the α - β system, but will be used to evaluate the low angle flow properties.

Pressure Coefficients for Low Flow Angles

For low flow angles it is desirable to define dimensionless pressure coefficients which utilize all seven measured probe pressures and are sensitive to changes in flow angularity with respect to the probe's x-axis. From Figure 2, one such pressure coeffi-

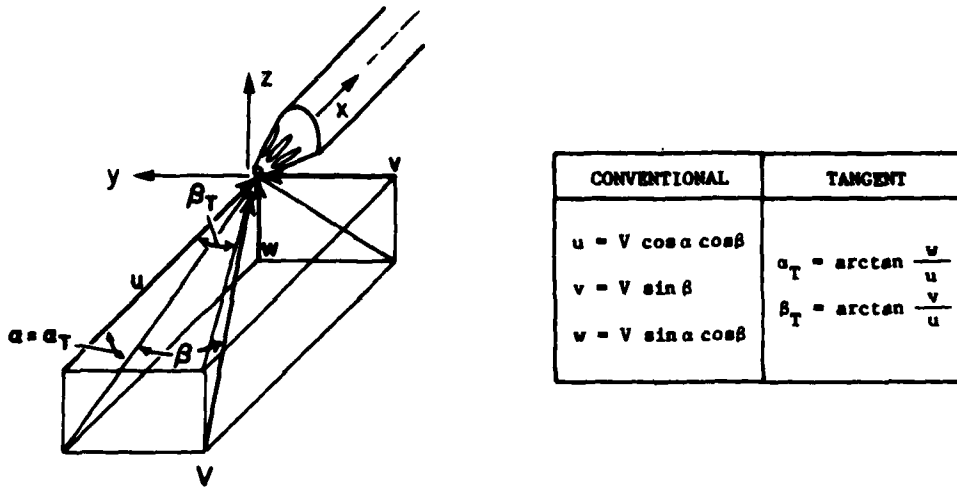


Figure 1. Low Angle Reference System

cient sensitive to changes in angle of attack in the x-z planes is defined as:

$$C_{\alpha_1} = \frac{P_4 - P_1}{P_7 - \bar{P}_{1-6}} \quad (1)$$

where the numerator measures changes in flow angularity based on the differences in opposite port pressures, and the denominator nondimensionalizes the term with the apparent dynamic pressure. This pseudo-dynamic pressure is obtained from the difference between the central port pressure, P_7 , which approximates the total pressure at low angles, and the average of the six surrounding pressures, \bar{P}_{1-6} , which collectively approximates the static pressure. From the definition of this pressure coefficient, it is easy to see that two other possibilities also exist: one which measures the pressure differential

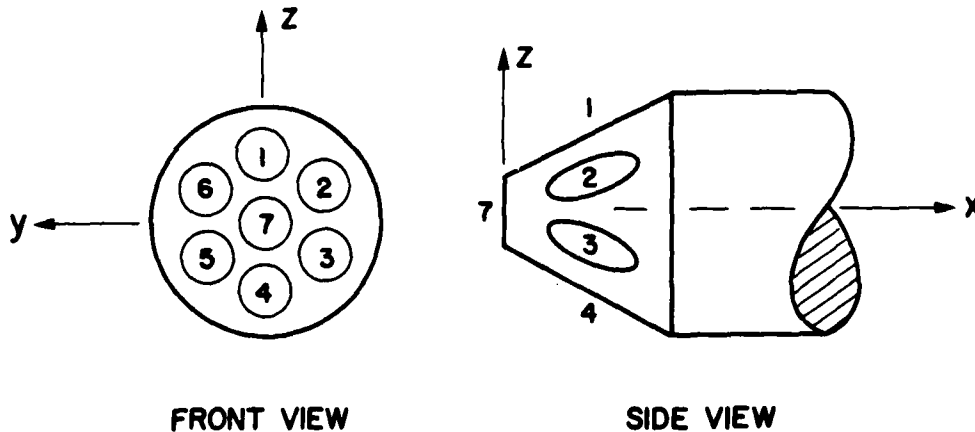


Figure 2. Port Numbering Convention and Principal Axes

between ports three and six, and the other, which measures the pressure differential between ports two and five. The complete set of these pressure coefficients include:

$$C_{\alpha_1} = \frac{P_3 - P_1}{P_7 - \bar{P}_{1-6}}, \quad C_{\alpha_2} = \frac{P_3 - P_6}{P_7 - \bar{P}_{1-6}}, \quad C_{\alpha_3} = \frac{P_2 - P_5}{P_7 - \bar{P}_{1-6}} \quad (2)$$

But before these coefficients can be of any use to us, they must be resolved into the $\alpha_T - \beta_T$ reference system. This is done by weighing the contribution of each coefficient in Eqns. (2) along the respective axis, which results in the following two equations:

$$C_{\alpha} = \frac{1}{3} (2C_{\alpha_1} + C_{\alpha_2} - C_{\alpha_3}) \quad , \quad C_{\beta} = \frac{1}{\sqrt{3}} (C_{\alpha_2} + C_{\alpha_3}) \quad (3)$$

The first equation defining C_{α} contains all three coefficients of Eqns. (2). In particular, C_{α_1} has the greatest significance, which only makes sense since it lies directly along the axis of interest. The equation defining C_{β} only takes into account the last two coefficients of Eqns. (2), assigning to each an equal significance. The fact that C_{α_1} is not included in this equation again makes sense, since it is directly aligned with the α_T -direction, ideally making it insensitive to changes in the perpendicular β_T -direction. In summary, the procedure of obtaining C_{α} and C_{β} requires two tasks. First, determine C_{α_1} , C_{α_2} , and C_{α_3} from the seven measured pressures using Eqns. (2) and then substitute these intermediate quantities into Eqns. (3) for the desired coefficients.

Having defined the two angular pressure coefficients, it is now appropriate to discuss the remaining low angle pressure coefficients, C_o and C_q , defined as:

$$C_o = \frac{P_7 - P_{oL}}{P_7 - \bar{P}_{1-6}} \quad , \quad C_q = \frac{P_7 - \bar{P}_{1-6}}{P_{oL} - P_{\infty L}} \quad (4)$$

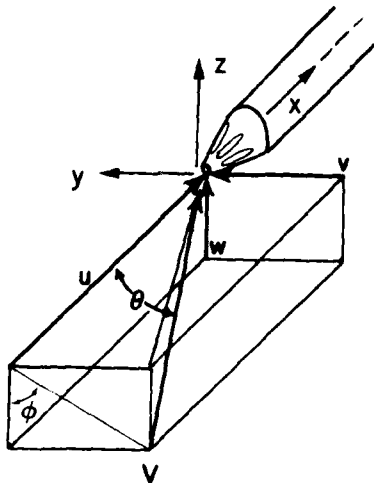
C_o is the apparent total pressure coefficient and functions as a correction factor to convert actual pressures measured by the probe to accurate values of local total pressure. From the numerator, it is seen that the coefficient measures the difference between the pseudo-total pressure measured by the probe, P_7 , and the actual total pressure. Just as with Eqn. (1), the coefficient is nondimensionalized by the denominator, which is a measure of the apparent dynamic pressure as previously described.

C_q functions much like C_o , but instead of correcting probe pressures to total pressure, C_q relates these pressures to the actual dynamic pressure. In this coefficient, the numerator represents the probe's approximation of dynamic pressure while the denominator consists of the actual dynamic pressure.

Axis System for High Flow Angles

Up to this point, our discussion has been limited to a description of the pressure coefficients used for flow angles below 30 degrees. Yet, the real advantage of using a seven-hole probe lies in its ability to determine flow angles as high as 80 degrees to the probe's x-axis.

A reference system better suited to high angle measurement than the tangential system is the polar reference system, which measures flow angularities in terms of θ and ϕ and is shown in Figure 3. In this system, θ , the pitch angle, is the angle the velocity vector makes with respect to the probe's x-axis; and ϕ , the roll angle, describes the azimuthal orientation of the velocity vector in the y-z plane, measured counterclockwise from the negative z-axis as viewed from the front. Although a singularity exists directly along the x-axis, this does not represent any problems in high angle measurement and



POLAR	TANGENT
$u = V \cos\theta$	$\alpha_T = \arctan \frac{w}{u}$
$v = V \sin\theta \sin\phi$	
$w = V \sin\theta \cos\phi$	$\beta_T = \arctan \frac{v}{u}$

Figure 3. High Angle Reference System

is avoided entirely by switching to the tangential reference system at low angles.

Pressure Coefficients for High Flow Angles

At low angles of attack, all seven of the measured probe pressures are used to form the pressure coefficients. However, at high angles of attack, as illustrated in Figure 4, the flow tends to detach over the downstream portions of the probe. Pressure ports lying in this separated region are insensitive to changes in flow angularity; consequently, it is not feasible to use their pressures in a meaningful coefficient. As a result, the pressure coefficients for high angle measurements must be defined so that they include only the pressures from ports in attached flow.

Typically, the separation points of a cylinder in turbulent flow are over 100 degrees from the frontal stagnation point (Ref. 3). And for a conical body, such as the probe tip,

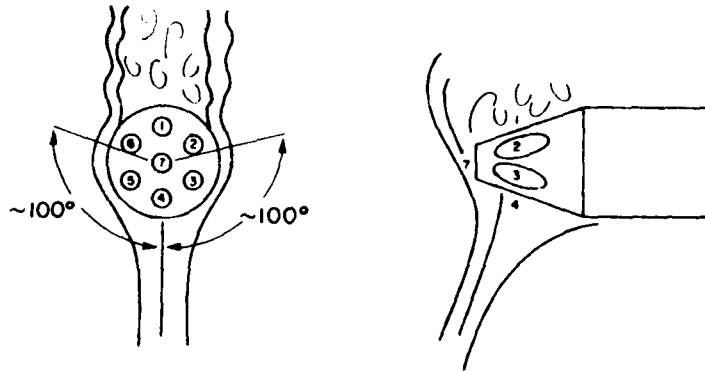


Figure 4. Flow Over Probe at High Angle of Attack

the flow is likely to remain attached longer. In addition, the u-velocity component is also likely to extend the separation points. Thus, for the condition depicted in Figure 4, pressure ports three, four, five, and seven lie in reliably attached flow; port one is in separated flow; and the disposition of ports two and six is uncertain. Using only those ports in attached flow, a coefficient sensitive to the angle of pitch is defined as:

$$C_{\theta_4} = \frac{P_4 - P_7}{P_4 - \frac{P_3 + P_5}{2}} \quad (5)$$

Following the same rationale as in the low angle case, the numerator measures changes in θ based on the differences in opposing port pressures. In this example, P_7 , the smaller of the two pressures, is subtracted from P_4 . Here again, the coefficient is nondimensionalized by dividing through with the apparent dynamic pressure. This pseudo-dynamic pressure is determined from the difference between the peripheral port pressure, P_4 , which at high angles approximates the total pressure, and the average of P_3 and P_5 , which when taken together are relatively independent to changes in roll and approximate the static pressure.

Using a similar argument, a coefficient which changes in proportion to roll angle is appropriately defined:

$$C_{\phi_4} = \frac{P_3 - P_5}{P_4 - \frac{P_3 + P_5}{2}} \quad (6)$$

The numerator of Eqn. (6) is sensitive to changes in ϕ , in that as the velocity vector rolls in either direction, the windward pressure rises and the leeward pressure falls. In this way, the difference between the two pressures varies significantly for variations

in roll, yet the average of their sums remains relatively constant. Once more, the coefficient is nondimensionalized with the same denominator as in the previous case.

Obviously, the above two coefficients are only valid for a narrow range in roll angle about port four. That is, as we rotate the velocity vector to either side of port four, the region of separated flow approaches either port five or three. Therefore, to insure that all pressures are taken from ports in attached flow, we restrict Eqns. (5) and (6) to roughly a 60-degree pie-shaped sector centered on port four. In this way, six pie-shaped sectors are summarily defined for high angle measurement, such that each has its own set of coefficients based on the pressures in attached flow. The remaining angular pressure coefficients are defined with the same method used to develop Eqns. (5) and (6), resulting in the following set of equations:

$$\begin{aligned}
 C_{\theta_1} &= \frac{P_1 - P_7}{P_1 - \frac{P_2 + P_6}{2}} & , & & C_{\phi_1} &= \frac{P_6 - P_2}{P_1 - \frac{P_6 + P_2}{2}} \\
 C_{\theta_2} &= \frac{P_2 - P_7}{P_2 - \frac{P_1 + P_3}{2}} & , & & C_{\phi_2} &= \frac{P_1 - P_3}{P_2 - \frac{P_1 + P_3}{2}} \\
 C_{\theta_3} &= \frac{P_3 - P_7}{P_3 - \frac{P_2 + P_4}{2}} & , & & C_{\phi_3} &= \frac{P_2 - P_4}{P_3 - \frac{P_2 + P_4}{2}} \\
 C_{\theta_4} &= \frac{P_4 - P_7}{P_4 - \frac{P_3 + P_5}{2}} & , & & C_{\phi_4} &= \frac{P_3 - P_5}{P_4 - \frac{P_3 + P_5}{2}} \\
 C_{\theta_5} &= \frac{P_5 - P_7}{P_5 - \frac{P_4 + P_6}{2}} & , & & C_{\phi_5} &= \frac{P_4 - P_6}{P_5 - \frac{P_4 + P_6}{2}} \\
 C_{\theta_6} &= \frac{P_6 - P_7}{P_6 - \frac{P_5 + P_1}{2}} & , & & C_{\phi_6} &= \frac{P_5 - P_1}{P_6 - \frac{P_5 + P_1}{2}}
 \end{aligned} \tag{7}$$

Similarly, the C_{θ} and C_{ϕ} coefficients are developed with the same rationale used to derive their low angle counterparts; the only difference resides in the choice of the pressures which are roughly equivalent to total and static pressures. These pressures, of course, vary in relation to the sector a particular coefficient describes. The complete set of these coefficients include:

$$\begin{aligned}
 C_{O1} &= \frac{P_1 - P_{OL}}{P_1 - \frac{P_2 + P_6}{2}} & , & & C_{Q1} &= \frac{P_1 - \frac{P_2 + P_6}{2}}{P_{OL} - P_{\infty L}} \\
 C_{O2} &= \frac{P_2 - P_{OL}}{P_2 - \frac{P_3 + P_1}{2}} & , & & C_{Q2} &= \frac{P_2 - \frac{P_3 + P_1}{2}}{P_{OL} - P_{\infty L}} \\
 C_{O3} &= \frac{P_3 - P_{OL}}{P_3 - \frac{P_4 + P_2}{2}} & , & & C_{Q3} &= \frac{P_3 - \frac{P_4 + P_2}{2}}{P_{OL} - P_{\infty L}} \\
 C_{O4} &= \frac{P_4 - P_{OL}}{P_4 - \frac{P_5 + P_3}{2}} & , & & C_{Q4} &= \frac{P_4 - \frac{P_5 + P_3}{2}}{P_{OL} - P_{\infty L}} \\
 C_{O5} &= \frac{P_5 - P_{OL}}{P_5 - \frac{P_6 + P_4}{2}} & , & & C_{Q5} &= \frac{P_5 - \frac{P_6 + P_4}{2}}{P_{OL} - P_{\infty L}} \\
 C_{O6} &= \frac{P_6 - P_{OL}}{P_6 - \frac{P_1 + P_5}{2}} & , & & C_{Q6} &= \frac{P_6 - \frac{P_1 + P_5}{2}}{P_{OL} - P_{\infty L}}
 \end{aligned}
 \tag{8}$$

Division of Angular Space

Having defined a host of coefficients for low and high angles and for various sectors around the probe, a question arises as to when a particular set of coefficients should be used. To arbitrarily assign angular cut-offs, based on probe symmetries, would be naive since actual data might suggest better division lines. With this in mind, a better scheme for locating the sector division lines is based on the isobars depicted in Figure 5. This method defines seven sectors, the central low angle sector and the six high angle periphery sectors, and allocates data points to a given sector based on the highest port pressure measured on the probe.

Polynomial Power Series Expansion

Once the data points are allocated to the proper sector with its corresponding pressure coefficients, a fourth order polynomial expansion is used to solve for the desired quantities. In two variables (i.e., using the two angular pressure coefficients) this

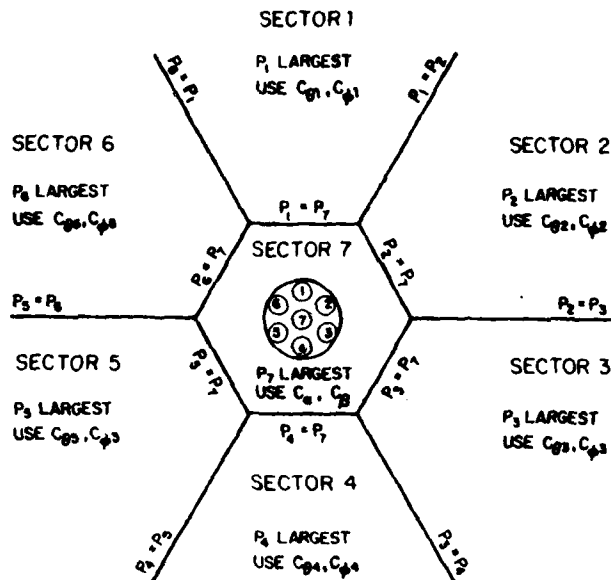


Figure 5. Division of Angular Space

expansion takes on the following form:

	Order of Terms
$A_i = K_1^A +$	0th
$K_2^A C_{\alpha_i} + K_3^A C_{\beta_i} +$	1st
$K_4^A C_{\alpha_i}^2 + K_5^A C_{\alpha_i} C_{\beta_i} + K_6^A C_{\beta_i}^2 +$	2nd (9)
$K_7^A C_{\alpha_i}^3 + K_8^A C_{\alpha_i}^2 C_{\beta_i} + K_9^A C_{\alpha_i} C_{\beta_i}^2 + K_{10}^A C_{\beta_i}^3 +$	3rd
$K_{11}^A C_{\alpha_i}^4 + K_{12}^A C_{\alpha_i}^3 C_{\beta_i} + K_{13}^A C_{\alpha_i}^2 C_{\beta_i}^2 + K_{14}^A C_{\alpha_i} C_{\beta_i}^3 + K_{15}^A C_{\beta_i}^4$	4th

where A is either α_T , β_T , C_θ or C_ϕ for low angles and θ , ϕ , C_θ or C_ϕ for high angles, with the subscript denoting the ith such quantity. The K's are the calibration coefficients, with the superscripts denoting the quantity to which a particular set of K's belong, and the subscripts identifying the coefficient of a particular term in the power series expansion. Note that in the high angle case, the C_α 's and C_β 's are replaced by C_θ 's and C_ϕ 's respectively. In matrix notation for "n" data points of a particular sector, a set of Eqn. (9)'s are represented as:

$$\begin{bmatrix} A_1 \\ A_2 \\ A_3 \\ \cdot \\ \cdot \\ \cdot \\ A_n \end{bmatrix} = \begin{bmatrix} 1 & C_{\alpha_1} & C_{\beta_1} & C_{\alpha_1}^2 & C_{\alpha_1} C_{\beta_1} & C_{\beta_1}^2 & \cdot & \cdot & \cdot & \cdot & C_{\beta_1}^4 \\ 1 & C_{\alpha_2} & C_{\beta_2} & C_{\alpha_2}^2 & C_{\alpha_2} C_{\beta_2} & C_{\beta_2}^2 & \cdot & \cdot & \cdot & \cdot & C_{\beta_2}^4 \\ 1 & C_{\alpha_3} & C_{\beta_3} & C_{\alpha_3}^2 & C_{\alpha_3} C_{\beta_3} & C_{\beta_3}^2 & \cdot & \cdot & \cdot & \cdot & C_{\beta_3}^4 \\ \cdot & \cdot \\ \cdot & \cdot \\ \cdot & \cdot \\ 1 & C_{\alpha_n} & C_{\beta_n} & C_{\alpha_n}^2 & C_{\alpha_n} C_{\beta_n} & C_{\beta_n}^2 & \cdot & \cdot & \cdot & \cdot & C_{\beta_n}^4 \end{bmatrix} \begin{bmatrix} K_1^A \\ K_2^A \\ K_3^A \\ \cdot \\ \cdot \\ \cdot \\ K_{15}^A \end{bmatrix} \quad (10)$$

But to simplify further discussion, Eqn. (10) is rewritten as:

$$[A] = [C][K] \quad (11)$$

In this form, the n x 1 A-matrix contains n values of the flow parameters of interest, the n x 15 C-matrix contains the expanded angular pressure coefficients for each of the n flow parameters, and the 15 x 1 K-matrix contains the calibration coefficients for the particular flow parameter of interest.

Determining the Calibration Coefficients

During the calibration process, the quantities within the A-matrix are set up by the experimenter in terms of the known tunnel conditions, and the terms within the C-matrix are determined from the measured probe pressures. A calibration procedure, therefore, involves the calculation of the unknown K-matrix. This calculation is performed by rearranging Eqn. (11) to solve for the unknown calibration coefficients. With matrix algebra, this is performed according to the procedure outlined by Netter and Wasserman (Ref. 4):

First multiply each side of Eqn. (11) by the transpose of the C-matrix:

$$[C]^T [A] = [C]^T [C][K] = [C^T C][K] \quad (12)$$

Next multiply each side by the inverse of the recently created C^TC-matrix:

$$[C^T C]^{-1} [C]^T [A] = [C^T C]^{-1} [C^T C][K] \quad (13)$$

Realizing that the product of a matrix and its inverse results in the identity matrix, Eqn. (13) simplifies to yield a solution for the unknown K-matrix in terms of the known C- and A-matrices:

$$[K] = [C^T C]^{-1} [C]^T [A] \quad (14)$$

This technique determines the calibration coefficients by a least squares curve fit to the experimental data.

Determining the Desired Flow Properties

Once the calibration coefficients are determined, the calibration process is complete. The probe is ready to be inserted in an unknown flow field and the desired flow properties determined. Once in the flow field, the probe's measured pressure readings allow us to determine the angular pressure coefficients; these coefficients are then manipulated to fill the C-matrix of Eqn. (10). Since the K-matrix is already known, the desired flow properties in the A-matrix are then determined explicitly. For a particular condition, the solutions for the desired flow properties take on the following functional forms:

Inner Sector (low flow angles)

$$\begin{aligned} \alpha_T &= f(C_\alpha, C_\beta) = K_1^{\alpha_T} + K_2^{\alpha_T} C_\alpha + K_3^{\alpha_T} C_\beta + \dots + K_{15}^{\alpha_T} C_\beta^4 \\ \beta_T &= f(C_\alpha, C_\beta) = K_1^{\beta_T} + K_2^{\beta_T} C_\alpha + K_3^{\beta_T} C_\beta + \dots + K_{15}^{\beta_T} C_\beta^4 \\ C_o &= f(C_\alpha, C_\beta) = K_1^C + K_2^C C_\alpha + K_3^C C_\beta + \dots + K_{15}^C C_\beta^4 \\ C_q &= f(C_\alpha, C_\beta) = K_1^C + K_2^C C_\alpha + K_3^C C_\beta + \dots + K_{15}^C C_\beta^4 \end{aligned} \quad (15)$$

Outer Sectors (high flow angles)

$$\begin{aligned} \theta &= f(C_{\theta_n}, C_{\phi_n}) = K_1^\theta + K_2^\theta C_{\theta_n} + K_3^\theta C_{\phi_n} + \dots + K_{15}^\theta C_{\phi_n}^4 \\ \phi &= f(C_{\theta_n}, C_{\phi_n}) = K_1^\phi + K_2^\phi C_{\theta_n} + K_3^\phi C_{\phi_n} + \dots + K_{15}^\phi C_{\phi_n}^4 \\ C_{\theta_n} &= f(C_{\theta_n}, C_{\phi_n}) = K_1^{C_{\theta_n}} + K_2^{C_{\theta_n}} C_{\theta_n} + K_3^{C_{\theta_n}} C_{\phi_n} + \dots + K_{15}^{C_{\theta_n}} C_{\phi_n}^4 \\ C_{\phi_n} &= f(C_{\theta_n}, C_{\phi_n}) = K_1^{C_{\phi_n}} + K_2^{C_{\phi_n}} C_{\theta_n} + K_3^{C_{\phi_n}} C_{\phi_n} + \dots + K_{15}^{C_{\phi_n}} C_{\phi_n}^4 \end{aligned} \quad (16)$$

Once the local total and dynamic pressure coefficients are specified, it is possible to determine the local total and dynamic pressures. This is accomplished by rearranging Eqns. (4) in the case of the inner sector, and Eqns. (8) in the case of the outer sectors, thereby solving for the desired pressures. This calculation involves the polynomial result for C_o or C_q and the seven measured probe pressures. As an example, the inner sector equations for local total and dynamic pressures are derived as follows:

Recalling that

$$C_o = \frac{P_7 - P_{oL}}{P_7 - \bar{P}_{1-6}} \quad \text{and} \quad C_q = \frac{P_7 - \bar{P}_{1-6}}{P_{oL} - P_{\infty L}} \quad (4)$$

the local total and dynamic pressures are then solved by manipulating Eqns. (4); thus:

$$P_{oL} = P_7 - C_o (P_7 - \bar{P}_{1-6}) \quad P_{oL} - P_{\infty L} = \frac{P_7 - \bar{P}_{1-6}}{C_q} \quad (17)$$

The same procedure is extended to determine the local total and dynamic pressures in the outer sectors.

III. Extension to Compressible Flow

Up to this point we have discussed the form of a calibration procedure which is only valid for incompressible flow. This is so because the calibration coefficients depend directly upon the angular pressure coefficients, which as pressure coefficients are themselves dependent upon Mach number (Ref. 5). As such, seven-hole probes with the present method of calibration are limited to surveying flows within the incompressible regime. This restriction is lifted easily enough with the inclusion of an additional pressure coefficient representative of compressibility. Consequently, the number of variables in the polynomial curve fit is increased from two (for incompressible flow) to three (for compressible flow).

Determining a Coefficient of Compressibility

Just like the angular pressure coefficients (C_α and C_β or C_θ and C_ϕ), the compressibility coefficient (hereafter denoted C_M) must be nondimensional and determined strictly from pressures measured on the probe. In addition, C_M must have the feature that it approaches zero at very low Mach numbers. That is, at very low Mach numbers all terms bearing a compressibility coefficient should be insignificant in the power series expansion. This, in effect, brings us back to an incompressible power series expansion in two variables, where the significant terms only contain the angular pressure coefficients. A further constraint requires the compressibility coefficient to approach a finite value in the hypersonic limit. In other words, for very high Mach numbers, large changes in Mach number should have a negligible effect on the compressibility coefficient. This reflects a limitation shared by all pressure probe methods in that Mach number becomes indeterminate at hypersonic speeds (Ref. 1). These requirements are satisfied by modeling the compressibility coefficient after the dynamic to total pressure ratio depicted

in Figure 6. This figure is idealized for isentropic flow; as such, it is not useful for flow speeds much beyond Mach one. However, since our calibration is limited to sub-sonic speeds, the isentropic idealization is valid through the sonic limit.

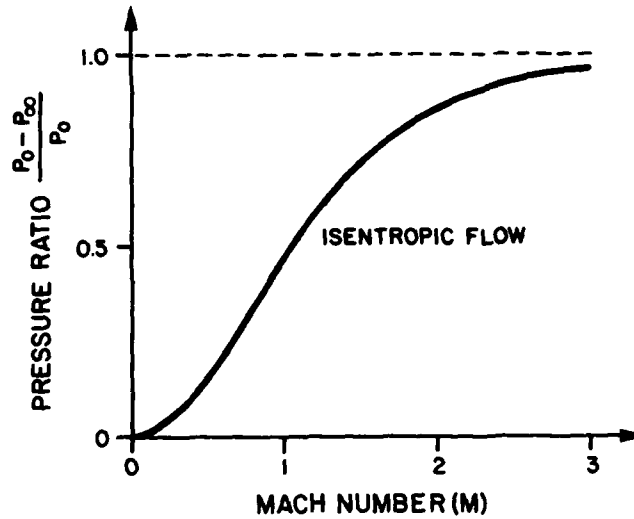


Figure 6. Compressibility Effects as a Function of Mach Number

To develop a compressibility coefficient from probe measured pressures, we need to represent the total and dynamic pressures from probe measured pressures. For the low angle case, a pseudo-total pressure is approximated by P_7 with a pseudo-dynamic pressure approximated by $P_7 - \bar{P}_{1-6}$. Thus, for the inner sector, a compressibility coefficient in terms of the dynamic to total pressure ratio is modeled by:

$$C_{M7} = \frac{P_7 - \bar{P}_{1-6}}{P_7} \quad (18)$$

The compressibility coefficients for each of the outer sectors are modeled in a similar manner; these outer sector coefficients include:

$$C_{M1} = \frac{P_1 - \frac{P_6 + P_2}{2}}{P_1}$$

$$C_{M2} = \frac{P_2 - \frac{P_1 + P_3}{2}}{P_2}$$

$$C_{M3} = \frac{P_3 - \frac{P_2 + P_4}{2}}{P_3}$$

69

$$C_{M4} = \frac{P_4 - \frac{P_3 + P_5}{2}}{P_4}$$

$$C_{M5} = \frac{P_5 - \frac{P_4 + P_6}{2}}{P_5}$$

(19)

$$C_{M6} = \frac{P_6 - \frac{P_5 + P_1}{2}}{P_6}$$

Selection of Data Points

Typical incompressible probe calibrations take approximately 80 data points in two variables (C_α and C_β) for each of the seven sectors (Ref. 1). This results in a total of about 560 data points for a complete calibration. To extend this present scheme into yet another dimension (Mach number) would create a data set of intractable proportions. Consequently, it is necessary to represent the data set with a sample of more manageable proportions. In addition, this sample must be chosen such that the density of chosen data points throughout the data set is homogenous. In other words, the sample must be an accurate representation of the data set, otherwise the calibration routine will not offer consistent accuracy throughout the range of data.

A method of ensuring a homogenous, yet random, sample of a three-dimensional parameter space is suggested by Cochran and Cox (Ref. 6). The technique is known as the method of Latin Squares, an example of which is shown in Figure 7. The plan depicted in this figure is a 3 x 3 square which actually represents a three-dimensional parameter space; one variable along the vertical axis, a second variable along the horizontal axis, and the third variable denoted by the letters along the axis going into the page. This square is better visualized in Figure 8, where it is shown in three dimensions instead

A	B	C
B	C	A
C	A	B

Figure 7. 3 x 3 Latin Square Plan

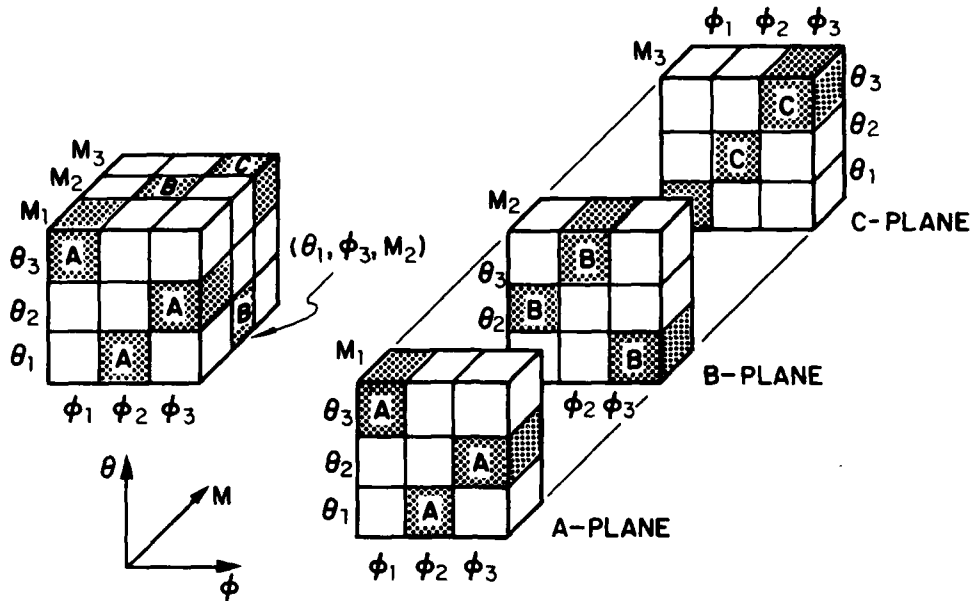


Figure 8. 3 x 3 Latin Square Shown in Three Dimensions

of the two-dimensional rendition of Figure 7. The 3 x 3 x 3 cube represents the entire parameter space, and each sub-cube represents a discrete data point within the entire data set. In Figure 7, the A's denote the data points to be selected in the A-plane (i.e., the plane in which the third variable, Mach number, is held constant), the B's denote the points selected in the B-plane, and so on. In this way, the entire data set is sampled by the points which appear as the shaded cubes in Figure 8. The unique feature of this sampling technique is that no matter from which axis direction the cube is viewed, the entire frontal space will appear covered by data points, one point deep; that is, no two points will appear to overlap each other. Furthermore, in any given plane where one variable is held constant, every value of the remaining two variables is sampled exactly once. Consequently, the method of Latin Squares guarantees a homogenous density of data points comprising the sample of the representative data set. Of course, the technique of Latin Squares is not limited to a 3 x 3 plan, but can be expanded to a 12 x 12 plan if desired; however, the more common plans range between the 5 x 5 and 8 x 8 squares (Ref. 6). This is true because as plan size increases, the ratio of points sampled to total points in the data set decreases. To illustrate, the 3 x 3 square of Figure 7 samples a 27-point data set with nine points, whereas a 10 x 10 square uses 100 points to sample a 1000-point set. Accordingly, the 3 x 3 Latin Square samples 33 percent of the entire data set, while the 10 x 10 Latin Square samples only 10 percent of the complete set. Nevertheless, a 3 x 3 square describes a given parameter space with only 27 data points, while a 10 x 10 square divides the same parameter space into

1000 discrete data points. Thus, a larger Latin Square represents a given parameter space with greater resolution, but samples the resulting data set with a smaller percentage of points. The experimenter, therefore, is faced with a *compromise* in choosing the Latin Square best suited to his needs.

For reasons to be discussed later, we selected a 6 x 6 Latin Square (shown in Figure 9) for each sector. This gives us a data set with six different values for each of the three variables θ , ϕ , and M , for a total of 216 data points per sector. Using the sampling technique of Latin Squares, each 216-point data set is represented by a sample of 36 points. As such, a total of 256 data points will be experimentally tested in all seven sectors for a complete calibration of the probe.

A	B	C	D	E	F
B	F	D	C	A	E
C	D	E	F	B	A
D	A	F	E	C	B
E	C	A	B	F	D
F	E	B	A	D	C

Figure 9. 6 x 6 Latin Square Plan

Polynomial Power Series Expansion in Three Variables

In the incompressible calibration, a fourth order polynomial expansion in two variables was used for a total of 15 terms with 15 corresponding calibration coefficients. By adding a third variable to the calibration, the number of terms in the fourth order expansion jumps from 15 to 35 with 35 corresponding calibration coefficients. In order to obtain a valid estimation of standard deviation, a surplus of about 20 data points over the number of calibration coefficients is necessary (Ref. 1). This sets the required number of data points for a given sector at 55; however, our sample size has already been constrained to 36 points due to the selection of a 6 x 6 Latin Square. It is possible to take more than one 36-point Latin Square sampling within the 216-point data set, but in the interest of keeping the total number of points required for a complete calibration down to a manageable number, so that time spent in the wind tunnel can be minimized, we elect to limit each of the seven samples to 36 data points. As a result, a fourth order curve fit is no longer feasible; consequently, the polynomial expansion is

reduced to the next lowest order.

A third order polynomial expansion in three variables requires 20 calibration coefficients. This leaves us with a 16 data point surplus, which is sufficient to calculate a valid standard deviation. Using the same format as Eqn. (9), a third order expansion in three variables takes on the following form:

$$\begin{aligned}
 A_i = K_1^A + & \hspace{15em} \text{Order of Terms} \\
 & \hspace{15em} \text{0th} \\
 & K_2^A C_{\alpha_i} + K_3^A C_{\beta_i} + K_4^A C_{M_i} + \hspace{10em} \text{1st} \\
 & K_5^A C_{\alpha_i}^2 + K_6^A C_{\beta_i}^2 + K_7^A C_{M_i}^2 + K_8^A C_{\alpha_i} C_{\beta_i} + K_9^A C_{\alpha_i} C_{M_i} + K_{10}^A C_{\beta_i} C_{M_i} + \hspace{2em} \text{2nd} \quad (20) \\
 & \left. \begin{aligned}
 & K_{11}^A C_{\alpha_i}^3 + K_{12}^A C_{\beta_i}^3 + K_{13}^A C_{M_i}^3 + K_{14}^A C_{\alpha_i}^2 C_{\beta_i} + K_{15}^A C_{\alpha_i}^2 C_{M_i} + \\
 & K_{16}^A C_{\alpha_i} C_{\beta_i}^2 + K_{17}^A C_{\beta_i}^2 C_{M_i} + K_{18}^A C_{\alpha_i} C_{M_i}^2 + K_{19}^A C_{\beta_i} C_{M_i}^2 + K_{20}^A C_{\alpha_i} C_{\beta_i} C_{M_i}
 \end{aligned} \right\} \text{3rd}
 \end{aligned}$$

where A is either α_T , β_T , C_O , or C_q for the inner sector and θ , ϕ , C_O , or C_q for the outer sectors, with the subscript denoting the *i*th such quantity. The K's are the calibration coefficients, where the superscript denotes the quantity to which a particular set of K's belong, and the subscripts identify the coefficient of a particular term in the power series expansion. In the case of an outer sector, the C_{α} 's and C_{β} 's are replaced by C_{θ} 's and C_{ϕ} 's, respectively.

Determination of Mach Number

As stated previously, this experiment limits its scope to surveying Mach numbers slightly below sonic flow on down to incompressible flow. Consequently, there are no shocks ahead of the probe and the isentropic flow relation applies:

$$\frac{P_{\infty}}{P_o} = \left[1 + \frac{\gamma-1}{2} M^2 \right]^{\frac{-\gamma}{\gamma-1}} \quad (21)$$

Rearranging Eqn. (21) and deriving Mach number in terms of the dynamic to total pressure yields:

$$M = \sqrt{\frac{2}{\gamma-1} \left(\left[1 - \frac{P_o - P_{\infty}}{P_o} \right]^{\frac{1-\gamma}{\gamma}} - 1 \right)} \quad (22)$$

And since we know C_O , C_q , and the seven probe pressures, we can explicitly determine the local Mach number from the dynamic to total pressure ratio. For the inner sector, this ratio is determined from Eqns. (4) and the seven probe pressures:

$$\frac{P_{oL} - P_{\infty L}}{P_{oL}} = \left[C_q \left(\frac{P_7}{P_7 - \bar{P}_{1-6}} - C_o \right) \right]^{-1} \quad (23)$$

Analogous equations for the outer sectors are developed in the same way, except that Eqns. (8) and the appropriate probe pressures are used instead. During calibration, the actual values of Eqn. (23) and its outer sector counterparts are known from the measured tunnel conditions. Solving Eqn. (21) in terms of the dynamic to total pressure ratio as a function of Mach number gives us:

$$\frac{P_{oL} - P_{\infty L}}{P_{oL}} = 1 - \left[1 + \frac{\gamma-1}{2} M_L^2 \right] \frac{\gamma}{1-\gamma} \quad (24)$$

Thus, if the total and static pressures cannot be measured directly, we can still determine the dynamic to total pressure ratio if only the Mach number is known. By noting the difference between Eqns. (23) and (24), we can estimate how accurately our polynomial curve fit determines the Mach number for the inner sector; similar arguments are also extended to the outer sectors.

Estimating Accuracy of the Curve Fit

Providing there are approximately twenty more data points than the number of calibration coefficients, it is statistically feasible to calculate a global estimate of the accuracy of the curve fit for each of the flow parameters. This is done by computing the standard deviation of the difference between the experimental data and the polynomial prediction of that data. For flow angles and Mach number, the following relation applies (Ref. 7):

$$\sigma(A) = \sqrt{\frac{1}{n} \sum_{i=1}^n (A_{EXP_i} - A_{POLY_i})^2} \quad (25)$$

where σ is the standard deviation; n , the total number of data points; and A , the desired flow parameter.

Even though the total and dynamic pressures are determined from C_o and C_q , the accuracies of these pressures are not representative of the accuracies obtained for C_o and C_q . To estimate the uncertainty in determining the total and dynamic pressures (for the inner sector, for example) requires the defining equations, Eqns. (17), and applying to them the method of Kline and McClintock (Ref. 8). Then, by taking the standard deviation of these uncertainties and nondimensionalizing them with the dynamic pressure, we arrive at the following estimates for the accuracies of these pressures:

$$\frac{\sigma(P_{oL})}{P_{oL} - P_{\infty L}} \approx \bar{C}_{qn} \sigma(C_o) \quad (26)$$

$$\frac{\sigma(P_{oL} - P_{\infty L})}{P_{oL} - P_{\infty L}} \approx \frac{\sigma(C_q)}{\bar{C}_q} \quad (27)$$

where \bar{C}_{qn} is the average value of this coefficient for a given sector denoted by "n".

Providing the errors between the actual values and the polynomial predictions of those values are normally distributed, there is a 68.3 percent probability that the polynomial prediction will fall within one standard deviation of the actual value. And at 1.96σ , this certainty is increased to 95 percent.

IV. Apparatus and Calibration Procedure

Probe Geometry

The seven-hole probe was constructed at the Air Force Academy by packing seven properly-sized stainless steel tubes into a larger stainless steel tube as shown in Figure 10. Although the inner seven tubes have an outside diameter of only 0.028 inches with a .005-inch wall thickness, accurate alignment is reasonably insured since the tubes can only pack in one unique way. Once assembled in this arrangement, the tubes are then soldered together and machined to provide the 25-degree half angle at the tip.

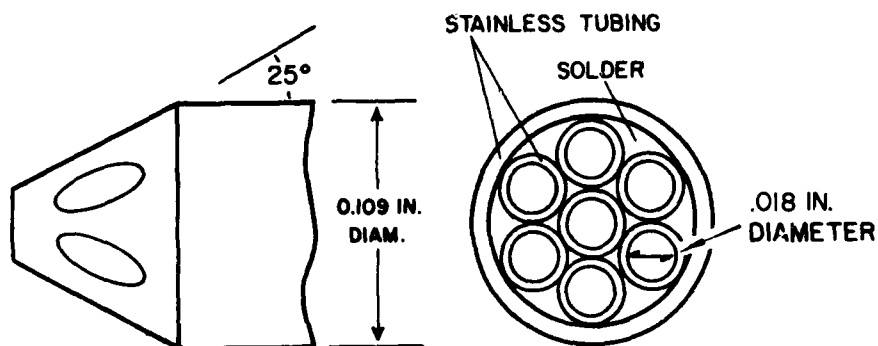


Figure 10. Probe Geometry

Probe Mounting Hardware

The test facility we used has a variable position sector capable of traversing 25 degrees in either direction for a total sweep of 50 degrees. Yet, for a complete calibration of the probe, a range of 0 through 80 degrees is necessary. Consequently, we constructed two stings (see Figure 11): a 15-degree bent sting for low angle measurements from -10 to 40 degrees angle of pitch, and a 55-degree bent sting for high angle measurements from 30 to 80 degrees angle of pitch. In addition, both stings were designed to permit the tip of the probe to pivot about a fixed point in the center of the tunnel.

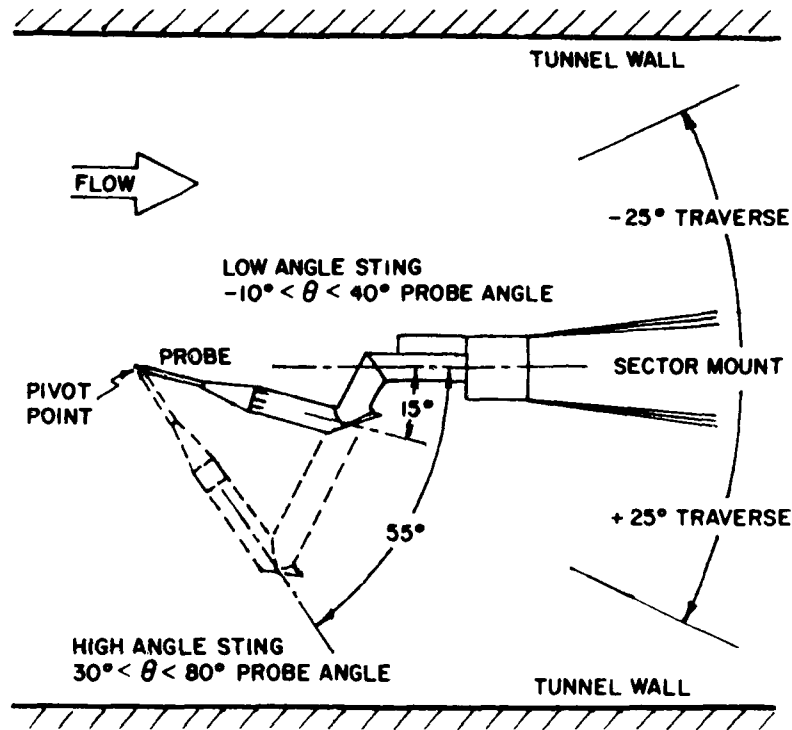


Figure 11. Sting Geometry

This insured uniform flow over the tip, despite changes in the angle of pitch.

Referring to Figure 12, each sting has 36 holes drilled in the front face. These holes are evenly spaced at 10-degree intervals and circumscribe a complete circle in roll. In this way, roll angle is accurately set by engaging the alignment pin on the probe holder with the alignment hole on the sting's face.

Data Point Selection

Since there are a total of 36 discrete roll angles, we are allowed to test six different roll angles in each outer sector. This is the primary reason why we chose the 6 x 6 Latin Square. Although the technique of Latin Squares allows us to conveniently sample large data sets, there are some drawbacks associated with seven-hole probe calibration. Primarily, we can no longer test the entire range of data and then allocate the data to a given sector based on the highest port pressure. Instead, we must determine beforehand which points will be tested and the sector they belong to. As a result, we are forced to draw the angular cutoffs for each sector without knowing where they actually lie.

In terms of angle of pitch, experience with incompressible calibrations has shown that 30 degrees is the smallest angle at which almost all points still fall in the outer

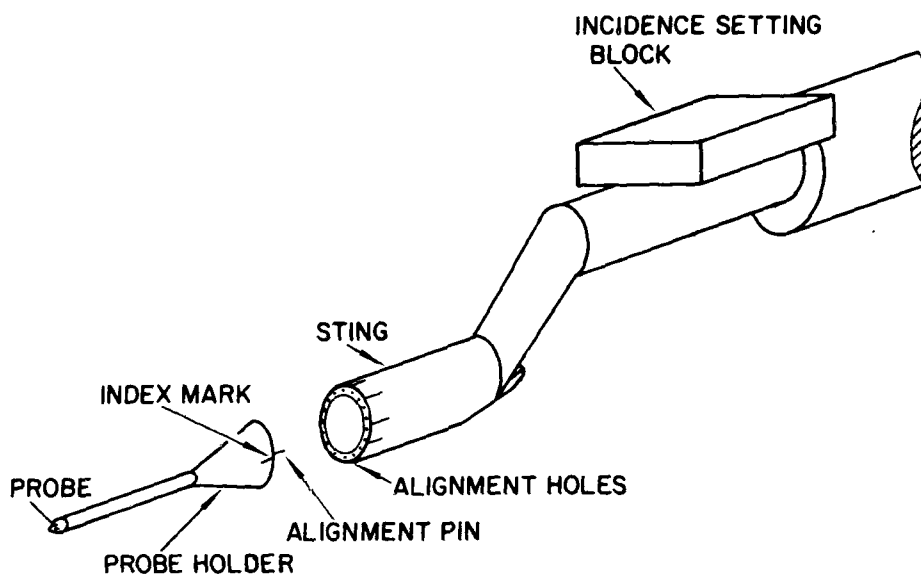


Figure 12. Probe, Holder, and Sting Assembly

sectors. Consequently, we selected 30 degrees as the lower limit of high angle measurement. And to match the number of roll measurements with an equal number of pitch settings, we measured pitch from 30 to 80 degrees in 10-degree increments for the outer sectors. Specifying the roll angles for each sector, however, presented some difficulties. Assuming a perfectly constructed probe, the outer sector boundaries, formed by the isobars between two adjacent peripheral ports, are coincident with a roll angle on which data is taken. This predicament is illustrated in Figure 13a for sector four. In this example, it is uncertain whether the points along the $\phi = 330$ degrees line belong in sector four or five, or whether the points on the $\phi = 30$ degrees line belong in sector three or four. To resolve this problem, we rotated the probe 5 degrees and then permanently fixed it to the holder in this position. From Figure 13b we see that the isobars have shifted off the points and that each sector has six clearly defined roll angles. Realistically, the probe is not constructed perfectly, causing the isobars to deviate from their ideal positions. But even so, the isobars can deviate up to 5 degrees in either direction before the points of one sector fall in another sector. At this point, one might ask if the probe can be accurately calibrated with the given offset. In actuality, the offset makes no difference. Since only the probe was rotated, leaving the index mark of the probe unchanged, the calibration process will interpret the pressures in terms of the roll angle set by the index mark. An alternative to the offset technique would use the roll angles between those presently measured (i.e., 5, 15, 25 . . . 355 degrees); however, this is an option we choose not to take.

Now that we've determined the angular coordinates of the data points to be taken in

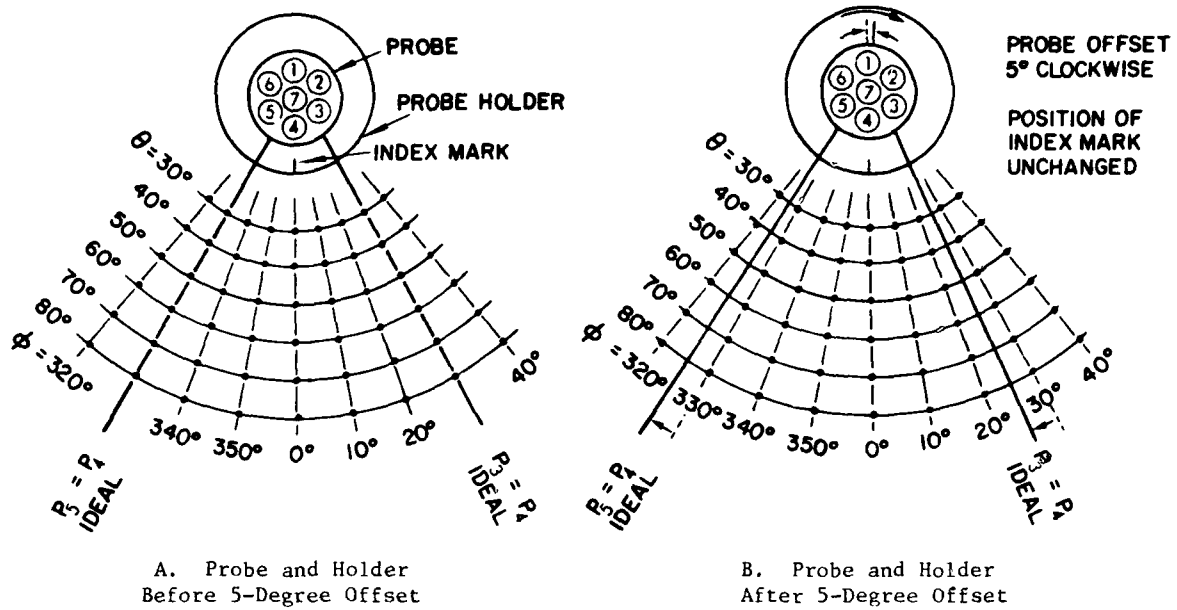


Figure 13. Probe and Holder Before and After Offset for Sector Four

the outer sectors, it's time we considered the inner sector. Since we cannot evenly represent the inner sector with a square matrix in θ and ϕ , we simply covered the parameter space with an even density of 36 data points. The values of pitch angle were 8, 16, and 24 degrees, with roll angles selected to insure a uniform distribution. The 6 x 6 Latin Square matrix was then systematically filled with these ordered pairs. Although data were taken in terms of pitch and roll, these angles were converted to angles of attack and sideslip prior to calibration calculations.

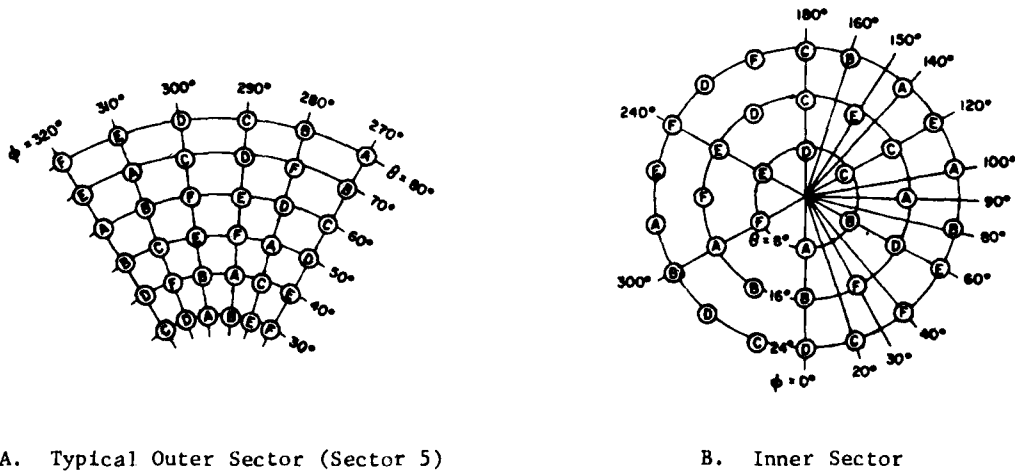


Figure 14. Distribution of Data Points

Since the angular coordinates of all data points are known, the last task is to determine the Mach number at which each is sampled. The Mach numbers for each of the six letters in the Latin Square of Figure 9 are: A, $M = 0.37$; B, $M = 0.45$; C, $M = 0.53$; D, $M = 0.66$; E, $M = 0.77$; F, $M = 0.91$. The resulting distribution of data points, and the Mach number each was tested at, can be inferred from Figure 14, which depicts the inner sector and a typical outer sector.

Test Procedure and Software

The experiment was conducted in the 1 x 1 foot blowdown wind tunnel at the United States Air Force Academy. All pressure measurements were made with a Scanivalve Corporation Model T Scanivalve and pressure transducer, calibrated by a Wallace and Tiernan sonar manometer digital U-tube. Data were collected and reduced by a Digital PDP 11/45 computer and LPS-11 Laboratory Peripheral System.

Before any data were taken, the test conditions had to be set for each run. Angle of pitch was set first with a Gunner's quadrant. The quadrant was clamped to the sting's incidence setting block (refer to Figure 12) and set to the desired angle of pitch minus the angle of the elbow on the sting (either 15 or 50 degrees). Next, the sector was hydraulically positioned to level the quadrant. Since the sector normally has a tendency to drift between runs, we froze the mechanism by driving it against blocks. Shims were used to fine tune the adjustments. Using this technique, the pitch was set to within ± 0.0112 degrees of the desired angle, and without drift. Once set, the pitch was not changed until all points at that angle were taken. The roll angle was set by pulling the spring-loaded probe forward to clear the alignment pin, then rotating it to the desired setting and engaging it into the new position. For a complete 360-degree revolution, the probe was first rotated counterclockwise (as viewed from the front) from 0 to 180 degrees in 10-degree increments. Next, it was rotated clockwise to the 190-degree position. And finally, the probe was rotated counterclockwise from 190 to 350 degrees in 10-degree increments. This subjected the tubes to a maximum twist of 180 degrees. After setting the roll angle, the tunnel was closed by a hydraulic ram and bolted shut. Mach number was then set by manually adjusting the tunnel's inner geometry with a series of hand cranks on the outside of the tunnel.

Prior to each run, the above variables were verified and input into the computer by a program titled TRISHP. Once the input conditions were set, air was blown, and after a few seconds to acquire steady-state conditions, data were recorded. Following this, the tunnel was reopened and the process repeated for a new data point. Typically, each run took about ten minutes to set up. Consequently, tests ran for over a week to acquire all 256 data points.

After all data were taken, a second program titled TRICAL performed the matrix operations, determined the calibration coefficients, and estimated the accuracy of the polynomial expansions in fitting the known data. Having done this, the probe calibration

is complete.

V. Discussion

The primary purpose of this experiment is to create a power series curve fit which accurately determines the actual flow conditions from pressures measured on the probe. The best way to evaluate the performance of the curve fit is to analyze the standard deviations between the experimental data and the polynomial determination of those data. These standard deviations are presented in Table 1. In addition, the standard deviations obtained from past incompressible calibrations are included in Table 2 for comparison (Ref. 1).

From Table 1, the standard deviations of α_T and β_T are 0.78 degrees and 0.72 degrees respectively. Although these values appear to be quite good, they are significantly

Table 1
STANDARD DEVIATIONS
COMPRESSIBLE FLOW CALIBRATION

INNER SECTOR		OUTER SECTORS	
SECTOR EXPRESSION	7	SECTOR EXPRESSION	AVERAGE 1 - 6
$\sigma(\alpha_T)$	0.78°	$\sigma(\theta)$	4.27°
$\sigma(\beta_T)$	0.72°	$\sigma(\phi)$	0.57°
$\frac{\sigma(P_{oL})}{P_{oL} - P_{\infty L}}$	2.5%	$\frac{\sigma(P_{oL})}{P_{oL} - P_{\infty L}}$	5.7%
$\frac{\sigma(P_{oL} - P_{\infty L})}{P_{oL} - P_{\infty L}}$	1.4%	$\frac{\sigma(P_{oL} - P_{\infty L})}{P_{oL} - P_{\infty L}}$	12.2%
$\sigma(M)$	0.006	$\sigma(M)$	0.061

higher than those obtained from the incompressible calibrations. Specifically, the incompressible flow calibrations produced standard deviations of 0.42 degrees for α_T and 0.36 degrees for β_T . Similar variations are also noted in the percent errors of total and dynamic pressures. Yet, when we recall that the incompressible calibrations used a fourth order power series with 80 data points per sector and the compressible calibration used a third order power series with only 36 data points per sector, the slight differences are quite understandable. Still another measure of curve-fit accuracy

Table 2
STANDARD DEVIATIONS
INCOMPRESSIBLE FLOW CALIBRATIONS (Ref. 1)

Average of Inner Sector		Average of 6 Outer Sectors	
EXPRESSION	Std. Dev.	EXPRESSION	Std. Dev.
$\sigma(\alpha_T)$	0.42°	$\sigma(\theta)$	0.84°
$\sigma(\beta_T)$	0.36°	$\sigma(\phi)$	1.17°
$\frac{\sigma(P_{oL})}{P_{oL} - P_{\infty L}}$	0.6%	$\frac{\sigma(P_{oL})}{P_{oL} - P_{\infty L}}$	1.2%
$\frac{\sigma(P_{oL} - P_{\infty L})}{P_{oL} - P_{\infty L}}$	1.0%	$\frac{\sigma(P_{oL} - P_{\infty L})}{P_{oL} - P_{\infty L}}$	2.4%

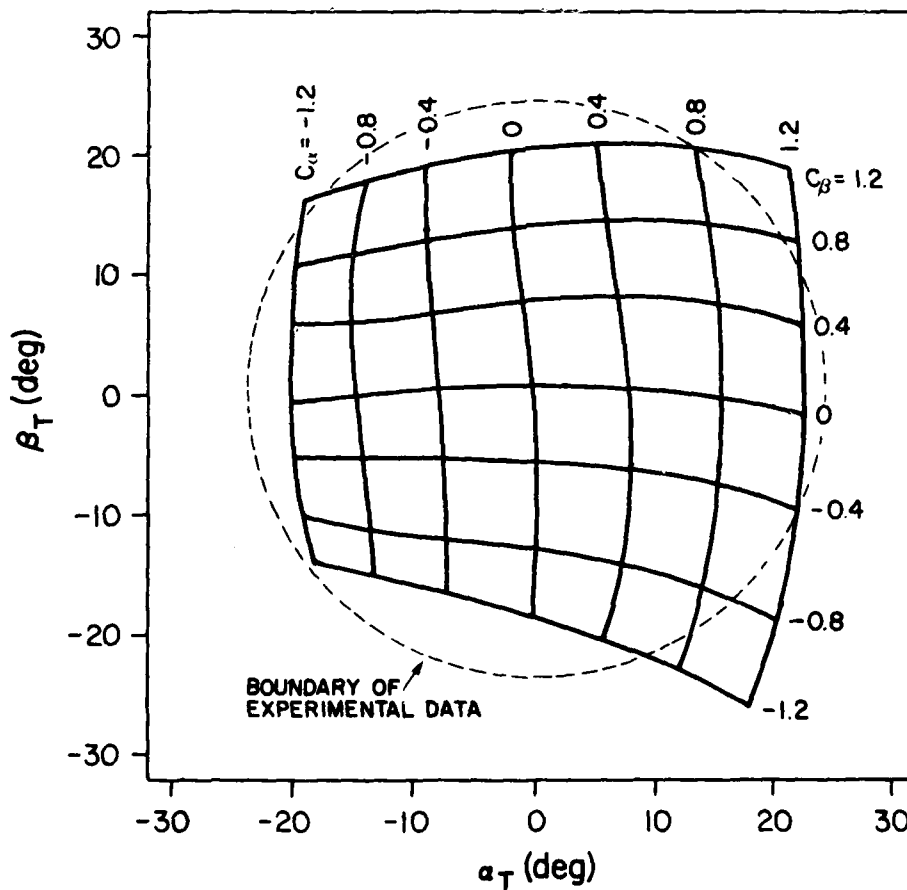


Figure 15. Isolines of C_α and C_β versus α_T and β_T for Low Angles at Low Mach Number

in the inner sector is apparent from Figures 15 and 16. Both of these figures depict isolines of C_α and C_β plotted against α_T and β_T with C_M held constant. Figure 15 presents this information for a low Mach number, with Figure 16 representative of a high Mach number. In both cases, the isolines of the coefficients are nearly straight and relatively orthogonal to each other, implying a linear dependence on their respective angle and independence to the other angle. These properties, however, begin to break

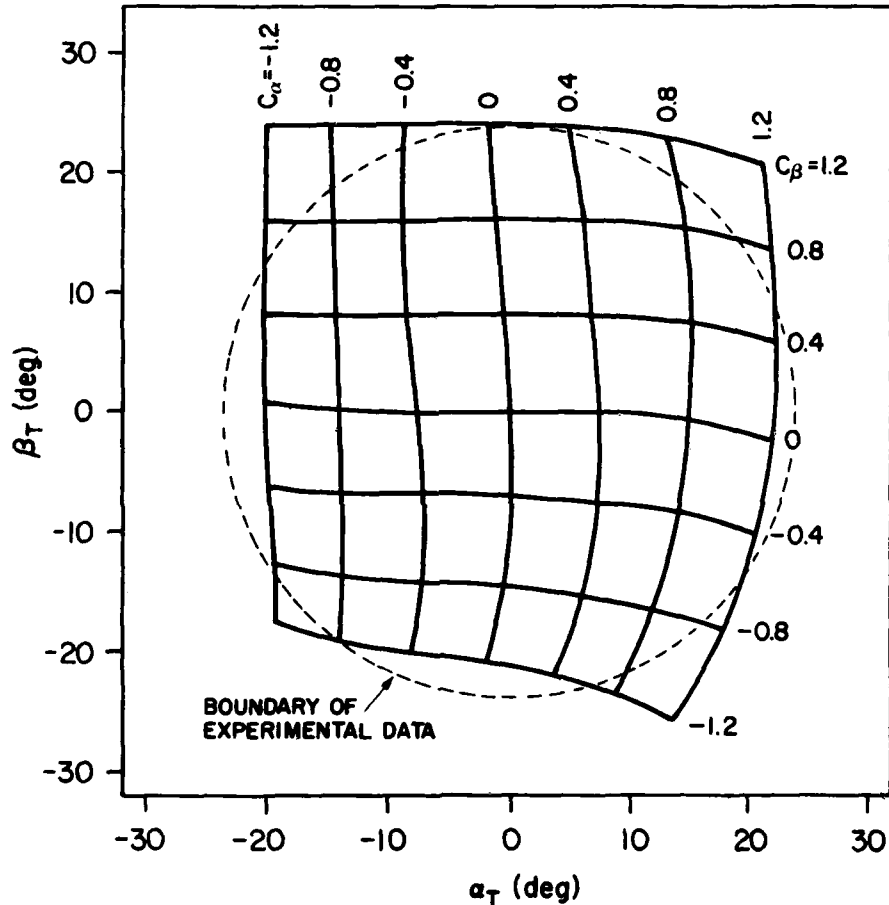


Figure 16. Isolines of C_α and C_β versus α_T and β_T for Low Angles at High Mach Number down as we exceed the limits of our experimental data. But since the boundaries of the experimental data coincide with the inner-outer sector interface (see Figure 17), data points lying outside the inner sector's experimental boundary will fall into the outer sectors. Consequently, the accuracy in determining flow properties is uniform throughout the inner sector.

In the outer sectors, the average standard deviation of the error in calculating ϕ is 0.57 degrees for the compressible calibration and 1.17 degrees for previous incompress-

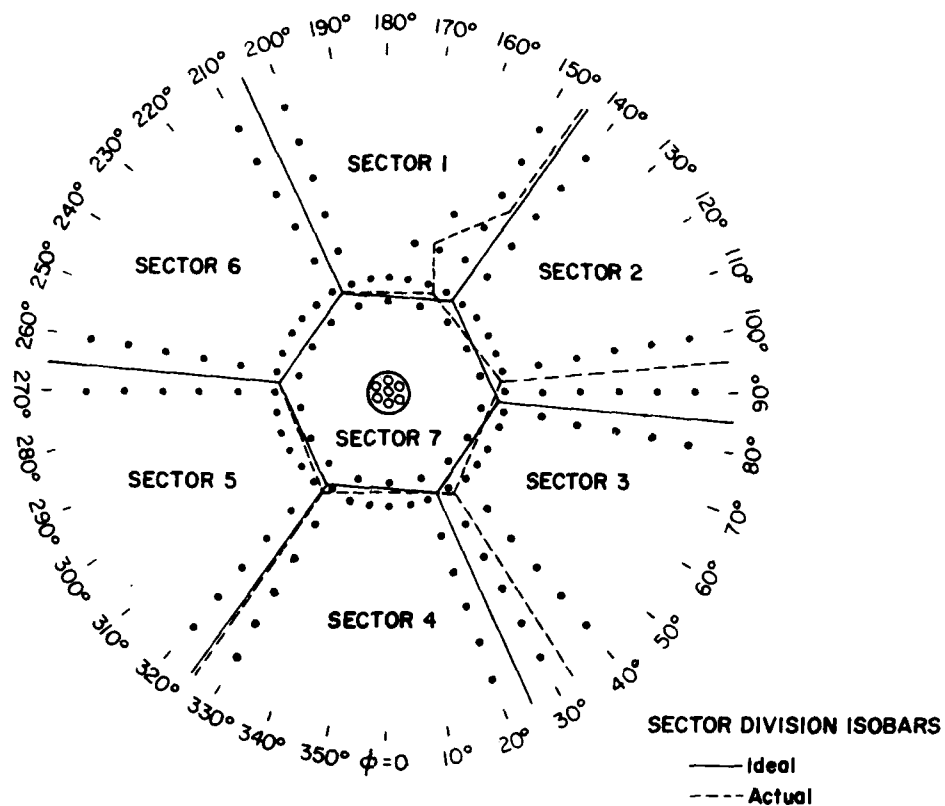


Figure 17. Ideal and Actual Sector Boundaries Based on the Highest Probe Measured Pressures

sible calibrations. Judging from Figure 17, one might expect the average standard deviation of ϕ for the compressible calibration to be substantially greater than that for the incompressible calibrations, because the actual boundaries of sectors one through four do not coincide with the ideal boundaries for which the calibration was made. Although this phenomenon is entirely consistent with the manufacturing anomalies associated with probe construction, the actual boundaries cannot be determined in advance and, therefore, cannot be taken into account in a calibration scheme using the method of Latin Squares. Nevertheless, despite the actual locations of the sector boundaries, the standard deviation in ϕ for the compressible calibration agrees favorably with its incompressible counterpart. The reason for this is shown in Figure 18. Even though Figure 18 is based on data taken from incompressible calibrations, it is representative of seven-hole probes in general. That is, the coefficient of roll continues to behave linearly, or in a way that can be represented easily by a polynomial, slightly beyond the isobaric sector boundaries. As such, the effect of using data within 10 degrees in roll from the selected boundaries, as Figure 18 suggests, does not have an adverse effect on fitting the data. Consequently, the disagreement between the actual and ideal sector boundaries

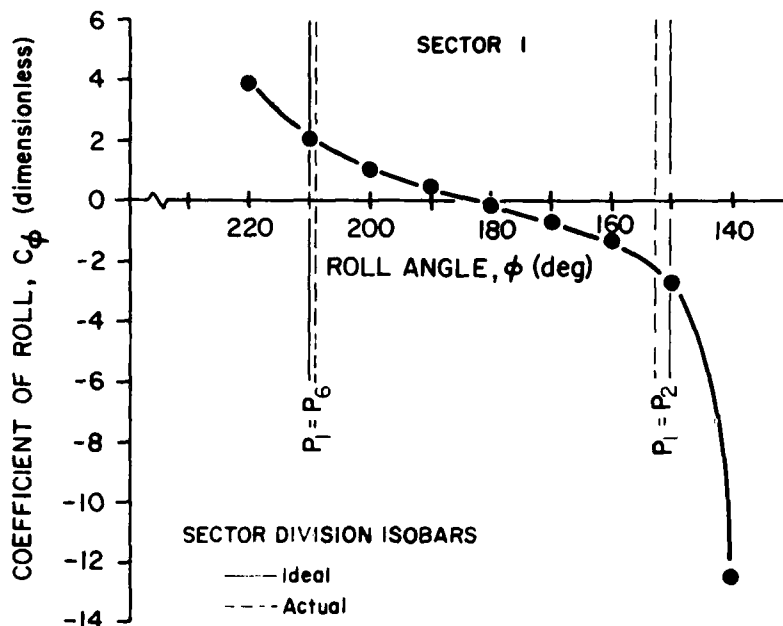


Figure 18. Incompressible Data Showing C_ϕ versus ϕ in Sector 1 for $\theta = 84$ Degrees

of Figure 17 does not significantly influence the determination of roll angle.

Despite the small error in calculating the roll angle, the standard deviation of the error in calculating pitch angle at 4.27 degrees is unacceptably high, especially when compared to the 0.84-degree standard error of previous incompressible calibrations. The actual variation between the experimental data and its polynomial prediction is presented in Figure 19, which depicts a typical outer sector. From this illustration, we can see that the greatest error in determining the pitch angle occurs at high angles of attack. This occurs as a result of the polynomial's inability to fit the actual data. Typically, the shape of the C_θ versus θ curve looks much like the lift curve of a stalling airfoil. Figure 20 illustrates such a curve for sector one, based on the extensive data available from incompressible probe calibrations. The reason why the curve hooks over as it does is evident after examining the two pressures comprising the numerator of the coefficient of pitch. According to Figure 20, the center port pressure decreases with increasing angle of pitch. Beyond some point, a suction develops at this port, causing the pressure there to dip below the free stream static pressure. But near 80 degrees angle of pitch, the suction breaks and the pressure begins to increase. As this occurs, the slope of the C_{p_7} curve approaches the slope of the C_{p_1} curve. Once the two slopes are equal, the rate of change of the numerator is zero, causing the slope of the coefficient of pitch also to be zero. No calibration may be made beyond this point, because each value of C_θ then corresponds to two values of θ . And since θ is a function of C_θ , the poly-

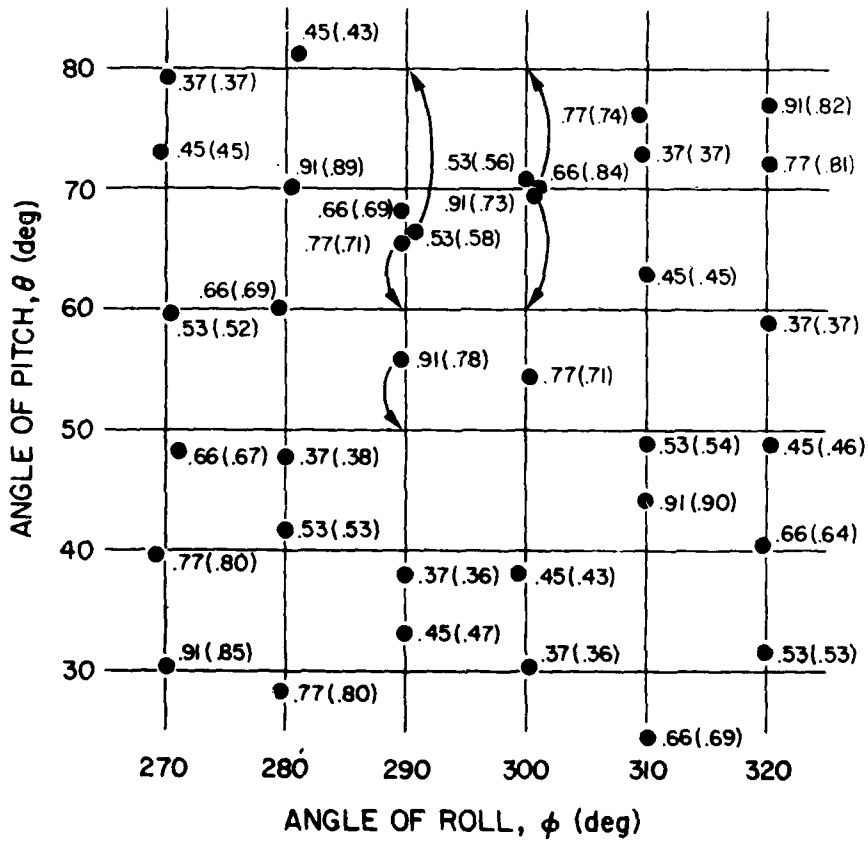
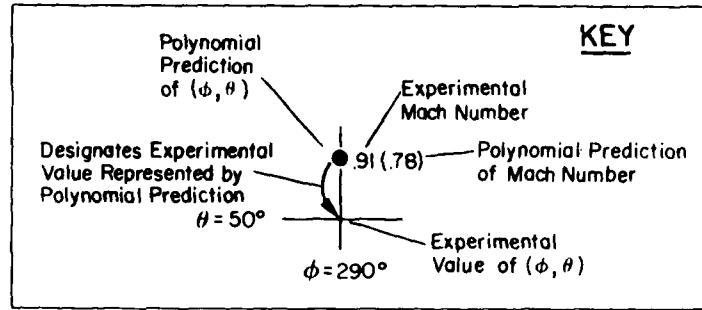


Figure 19. Three-Dimensional Data Set Showing Correlation Between Experimental and Polynomial Data for Sector 5

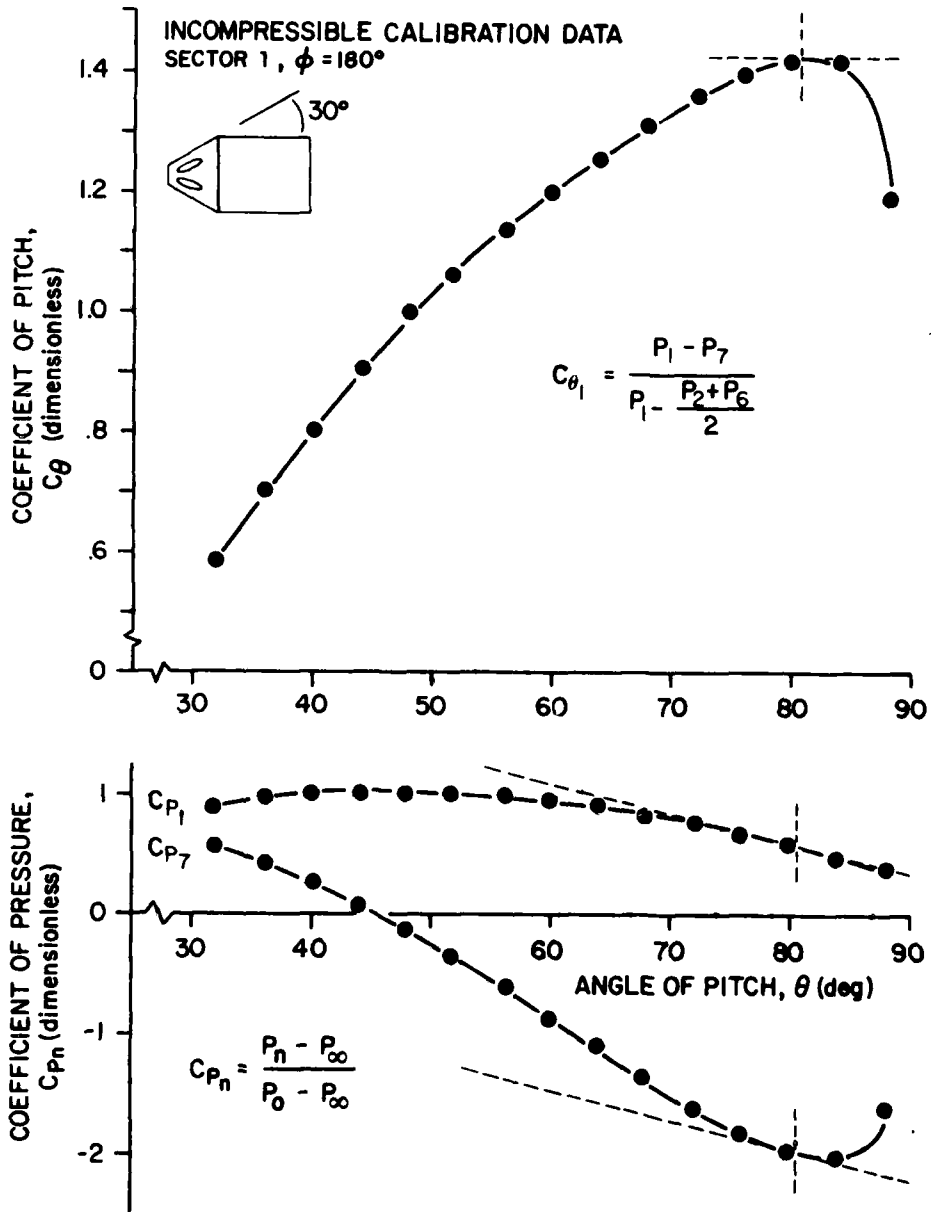


Figure 20. Mechanism for the Breakdown of Linearity in the Coefficient of Pitch at High Angles of Attack

nomial can only calculate one unique value of θ for a given value of C_p . Therefore, based on the information presented in Figure 20, we would expect to be capable of calibrating the probe out to 80 degrees angle of pitch. This was indeed the case for the past incompressible calibrations, but not the case in our compressible calibration, as Figure 19 vividly points out.

The failure of the calibration at high angles of pitch is most likely the result of probe geometry. Specifically, the half angle of the probe used in our compressible calibration is 25 degrees (see Figure 10) as opposed to the 30-degree half angle of the probes used in the incompressible calibrations. This steeper half angle was incorporated to permit a closer approximation of total pressure (as measured by the peripheral ports) at high angles, in the hope of extending the range of calibration beyond 80 degrees of pitch. However, this reasoning overlooked the effect increasing the half angle would have on the central port. That is, a steeper half angle requires the flow passing around the probe tip to turn through a greater angle, causing the suction over the central port to break at a lower angle of pitch. Consequently, the slope of the coefficient of pitch levels off earlier, limiting the calibration to a pitch angle below 80 degrees. But even as this theoretical upper limit of the calibration is approached, the breakdown in linearity of the coefficient of pitch with increasing angle of pitch forces the polynomial to work harder to fit the data. Since at high angles of attack small changes in the coefficient of pitch result in large changes in the angle of pitch, a small mismatch between the actual data and the polynomial curve fit translates into a large error as Figure 21 illustrates. Thus, as a result of the difficulty in fitting the actual data near the theoretical limit of calibration as established by the probe's geometry, the calibration appears to be limited to an angle of pitch below 80 degrees.

To confirm these suspicions, we ran a second data reduction, excluding all 80-degree pitch data. The standard deviations of the truncated data set are displayed in Table 3

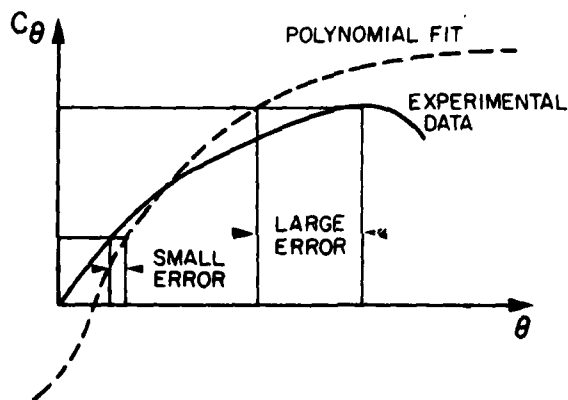


Figure 21. Limitations of Third Order Curve Fit at High Angles of Attack

Table 3
STANDARD DEVIATIONS
COMPRESSIBLE FLOW CALIBRATION

INNER SECTOR		OUTER SECTORS ($\theta = 80^\circ$ Data Truncated)	
SECTOR EXPRESSION	7	SECTOR EXPRESSION	AVERAGE 1 - 6
$\sigma(\alpha_T)$	0.78°	$\sigma(\theta)$	0.79°
$\sigma(\beta_T)$	0.72°	$\sigma(\phi)$	0.39°
$\frac{\sigma(P_{oL})}{P_{oL} - P_{\omega L}}$	2.5%	$\frac{\sigma(P_{oL})}{P_{oL} - P_{\omega L}}$	1.1%
$\frac{\sigma(P_{oL} - P_{\omega L})}{P_{oL} - P_{\omega L}}$	1.4%	$\frac{\sigma(P_{oL} - P_{\omega L})}{P_{oL} - P_{\omega L}}$	4.1%
$\sigma(M)$	0.006	$\sigma(M)$	0.022

and reflect a significant decrease in the error associated in calculating the experimental quantities. For example, the standard deviation in calculating pitch angle went down from 4.27 degrees to 0.79 degrees. The correlation between the data points of sector five also improved dramatically and is depicted in Figure 22. However, one must keep in mind that since the 80-degree points were removed from the data set, the data set is no longer as accurately represented. That is, in addition to losing the 80-degree data, we also lost an equal number of associated roll angle and Mach number data. Nevertheless, the greatly reduced standard deviations support our contention that for our probe in the vicinity of 80 degrees, the third order curve fit is incapable of accurately fitting the data.

VI. Conclusions and Recommendations

The polynomial expansion in three variables accurately extends the calibration of seven-hole probes into the compressible regime. Based on the reasonably close correlations between the standard deviations of past incompressible calibrations and the standard deviations of the compressible calibrations, the method of Latin Squares furnishes a sample space which accurately represents a much larger three-dimensional parameter space. Finally, the third order curve fit accurately represented the parameter space

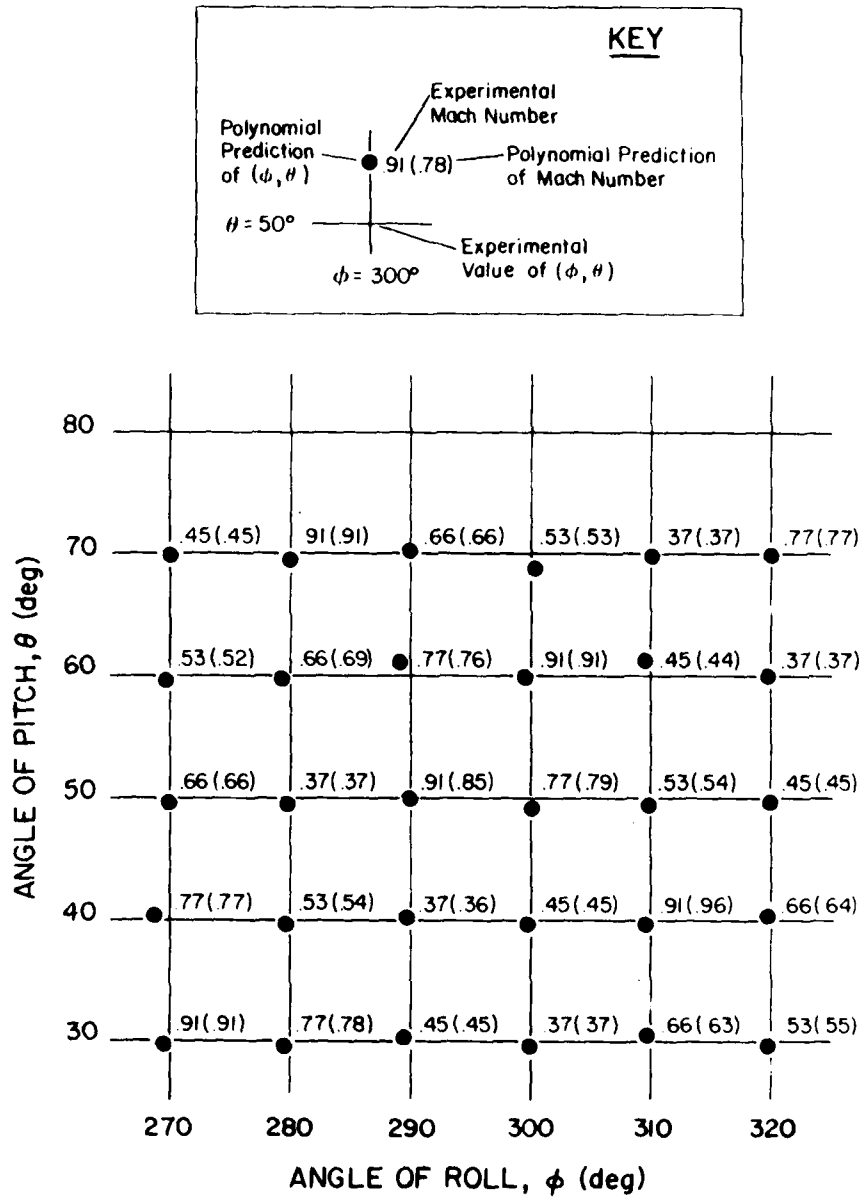


Figure 22. Three-Dimensional Data Set Showing Correlation Between Experimental and Polynomial Data for the Truncated Data Set of Sector 5

out to an angle of pitch of 70 degrees, but fell completely apart when required to fit the data extending to 80 degrees angle of attack.

It is recommended that an additional Latin Square be run in an outside quadrant. A set of calibration coefficients can then be determined using that Latin Square of data only; the same should be done with the original square. The results can then be examined to see how well the calibration coefficients of one square determine the values of the other square and vice versa. Close correlations should establish beyond a reasonable doubt the validity of a Latin Square in representing a parameter space. Next, both Latin Squares should be combined to determine another set of calibration coefficients, which in turn can be used to see if more data points significantly improve the degree of fit. Lastly, using the combined set of data points, extend the calibration to a fourth order polynomial and examine it to see if the addition of the fourth order terms significantly improve the degree of fit up to 80 degrees angle of attack.

VII. Acknowledgements

The authors of this paper wish to acknowledge the assistance of several individuals, who without their help and expertise, this calibration would not have been possible. In addition to the various technicians who installed the equipment and operated the tunnel, Mr. Claude Hollenbaugh was chiefly responsible for constructing the seven-hole probe as well as the holding and indexing apparatus. Capt. Tom Bolick wrote the computer software which performed the data acquisition and reduction for the probe calibration. And finally, Lt. Col. Roger Gallington, who engineered the theory of seven-hole probes, provided the background on incompressible flow calibrations and furnished guidance for the extension to compressible flow.

Symbols

A_i		the i th value of a particular data point, where A is either α_T , β_T , C_o , or C_q for low angles and α , ϕ , C_{on} , or C_{qn} for high angles
A_{EXP_i}		the i th value of the experimentally known value of A
A_{POLY_i}		the i th value of the polynomial predicted value of A
C_{Mn}	$n=1-7$	coefficient representative of compressibility effects
C_o		apparent total pressure coefficient for low angles
C_{on}	$n=1-6$	apparent total pressure coefficient for high angles
C_q		apparent dynamic pressure coefficients for low angles
\bar{C}_{qn}	$n=1-7$	average value of the apparent dynamic pressure coefficients for a given sector
C_{qn}	$n=1-6$	apparent dynamic pressure coefficients for high angles

AD-A108 338

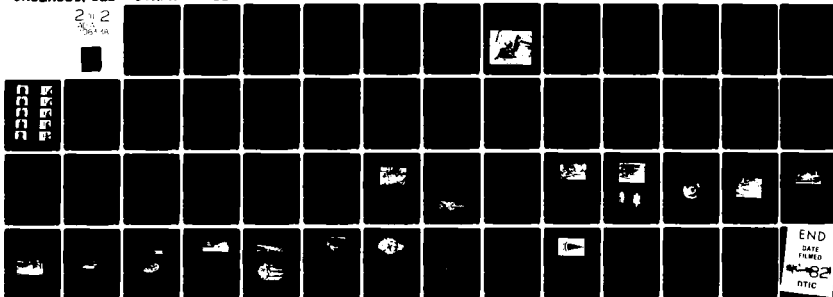
AIR FORCE ACADEMY CO
AIR FORCE ACADEMY AERONAUTICS DIGEST - FALL/WINTER 1980.(U)
MAY 81 A M HIGGINS, E J JUMPER, J M KEMPF
USAF-TR-81-4

F/0 20/4

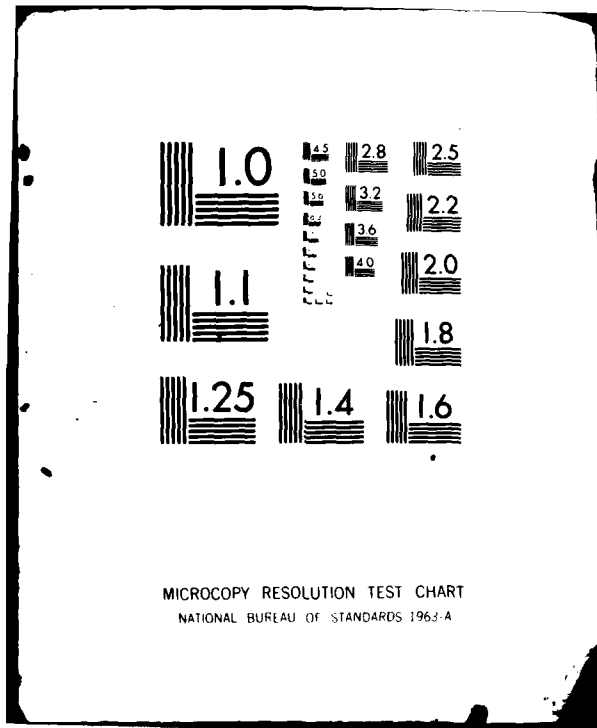
UNCLASSIFIED

NL

2
1
2



END
DATE
FILMED
1-82
DTIC



MICROCOPY RESOLUTION TEST CHART
NATIONAL BUREAU OF STANDARDS 1963-A

C_{p_n}	n=1-7	coefficient of pressure (arrived at by nondimensionalizing an individual port pressure)
C_α		angle of attack pressure coefficient for low angles
C_{α_n}	n=1-3	intermediate pressure coefficients used to determine C_α and C_β
C_β		angle of sideslip pressure coefficient for low angles
C_{θ_n}	n=1-6	pitch angle pressure coefficient for high angles
C_{ϕ_n}	n=1-6	roll angle pressure coefficient for high angles
K_n^A	n=1-20	calibration coefficient, where A denotes the parameter to which a particular set of K's belong, and n denotes the particular term of the calibration coefficient in the polynomial power series expansion
M		Mach number of free stream
M_L		local Mach number
P_n	n=1-7	pressure at port "n"
P_o		total pressure of free stream
P_{oL}		local total pressure
P_∞		static pressure of free stream
$P_{\infty L}$		local static pressure
\bar{P}_{1-6}		average of pressures 1 through 6
u, v, w		local velocity components with respect to probe
V		local velocity with respect to probe
α		angle of attack
α_T		angle between probe axis and velocity vector projected on vertical plane through probe's x-axis
β		angle of sideslip
β_T		angle between probe axis and velocity vector projected on horizontal plane through probe's x-axis
θ		total angle between velocity vector and probe's x-axis
γ		ratio of specific heats
ϕ		angle between a plane containing the velocity vector and the probe's x-axis and a vertical plane through the probe's x-axis measured positive clockwise from port number four as viewed from the front
σ		standard deviation

References

1. Gallington, R. W. "Measurement of Very Large Flow Angles with Non-Nulling Seven-Hole Probes." Aeronautics Digest - Spring/Summer 1980, USAFA-TR-80-17, USAF Academy, Colorado 80840, pp. 60-88.
2. Robertson, J. A. and Crowe, C. T. "Wave Propagation in Compressible Fluids." Engineering Fluid Mechanics, 1st ed. Boston: Houghton Mifflin Co., 1975, p. 370.
3. Chow, C. Y. and Kuethe, A. M. "Flow Around Spheres and Circular Cylinders." Foundations of Aerodynamics: Bases of Aerodynamic Design, 3rd ed. New York: John Wiley and Sons, 1976, p. 375.
4. Netter, J. and Wasserman, W. "Simple Linear Regression Model in Matrix Terms." Applied Linear Statistical Models. Illinois: Richard D. Irwin, Inc., 1975, p. 200.
5. Barker, K. W., Gallington, R. W., and Minster, S. N. "Calibration of Five-Hole Probes for On-Line Data Reduction." Aeronautics Digest - Spring 1979, USAFA-TR-79-7, USAF Academy, Colorado 80840.
6. Cochran, W. G. and Cox, G. M. "Double Grouping: Latin Squares." Experimental Designs, 2nd ed. New York: John Wiley and Sons, 1957.
7. Holman, J. P. "Statistical Analysis of Experimental Data." Experimental Methods for Engineers, 3rd ed. New York: McGraw-Hill, 1978, p. 51.
8. Kline, S. J. and McClintock, F. A. "Describing Uncertainties in Single-Sample Experiments." Mechanical Engineering, January 1953.

USAFA-TR-81-4

SECTION III

Biomechanics

DEVELOPMENT OF DESIGN CRITERIA FOR RAPID PRE-EJECTION
CREW RESTRAINT OF UPPER TORSO

A.M. Higgins* and G. Kroh**

Abstract

This paper investigates the possibility of reducing the period between the initiation of the ejection sequence (i.e., lifting ejection initiation handles, pulling the D-ring, etc.) and the first motion of the ejection seat out of the aircraft. The proposed method of reducing this time period is to provide a more rapid retraction and restraint of the crew member's upper torso during the ejection process than is presently used. The results of an experimental test program using human volunteers are presented in this report and demonstrate that human subjects can easily be retracted 10 inches in approximately 150 milliseconds. Additional tests at retraction lengths of 12 and 14 inches to determine if similar retraction times can be attained for these retraction distances are recommended.

I. Introduction

For obvious reasons, an aircraft escape system must function as rapidly as possible once it has been initiated. This aspect of escape system performance has become increasingly important with the introduction of newer aircraft such as the A-10 which operate continuously in low-altitude, high-speed environments where milliseconds lost in clearing the aircraft can mean the difference between life and death for an airman. The most obvious point in the ejection sequence where time can be reduced is during the period allowed for retraction and restraint of the crew member prior to first motion of the ejection seat. The purpose of retracting and restraining an aircrew member's upper torso is to align the crew member's spine with the force vector of the ejection catapult prior to actual initiation of the catapult (Ref. 1). It should be noted that the canopy of the aircraft is being removed to clear the ejection path concurrently with this retraction. The present Air Force escape specification (Ref. 2) requires that the powered inertia reel of the ejection system be capable of positioning an aircraft seat's occupant through 0 to 18 inches of travel. It also allows a retraction time of 0.3 seconds at 70 degrees Fahrenheit. This 300-millisecond delay requirement is significant, and its elimination has been suggested. In fact, the Air Force's A-10 System Program Office at Wright-Patterson AFB at one time actively supported the removal of this delay from the A-10's ejection seats. What is really being suggested is a trade-off between increased injury potential (principally to the spine) that would exist if the delay for spinal positioning and restraint was removed and decreased mortality due to a more rapid removal of the aircrew member from the stricken aircraft. Unfortunately, the trade-off is extremely difficult to quantify, and consequently the decision to retain or remove

*Major, USAF, Associate Professor of Aeronautics, DFAN

**Visiting Scientist at the 6570th Aerospace Medical Research Laboratory (AMRL),
German Air Force Institute of Aviation Medicine, Furstenfeldbruck, Germany

the time delay is very hard to make.

If one looks more closely at this time delay it seems to have been based on requirements for the mechanical inertia reel assembly rather than consideration of human physiological tolerance. The question a designer must first ask then is, "How fast can a crew member be safely retracted and restrained?" If it can be done safely in 150 milliseconds, for example, we have gained valuable time without compromising the necessity of spinal alignment before the catapult force of the ejection system is applied to the human body. In fact, a requirement for an inertia reel that can accomplish this goal was recently published as an Air Force Technical Need (Ref. 3). For this analysis we assumed that the mechanical requirements of a more rapid retraction can be accomplished as well as faster removal of the aircraft canopy. We therefore set out to determine if the retraction time can be safely reduced to something significantly less than 300 milliseconds.

II. Test Approach

We felt that the only way we could conclusively demonstrate actual reduced retraction time was to physically experiment and measure the retraction of human bodies. Of course, one cannot "just begin" when human volunteer subjects are involved. The testing had to be approached carefully with an engineering test plan and a medical human-use protocol that was carefully thought out and which considered the safety of the human test subjects as paramount.

Our approach was to first analyze each part of the retraction and restraint sequence and look for critical parameters that characterize the test severity. For example, the initial stage of retraction involves large retraction cable forces which are transmitted to the shoulders of the subject through the restraint harness. One critical parameter for this phase of retraction then was cable force. At the same time, a careful review of existing literature had to be done to determine the tolerable limits for these critical parameters. Here, for example, we had to determine what levels of cable force (harness loads) are allowable and what levels were expected in the tests.

Unfortunately, little information on the retraction of humans in ejection seats was available (Ref. 1 and 4). Therefore, the following test procedure approach was adopted in order to gather information: tests would begin at a level of retraction speed that would not jeopardize the human subjects, and they would then progress in steps of severity, where the test severity was judged to be a function of retraction length as well as the speed of retraction. Consequently, we decided to do three test series. The first series would involve only 10-inch retractions and would begin at a retraction speed where previous test data was available and the retractions were shown to be tolerable. The second and third series would involve 12-inch and 14-inch retractions beginning at the initial retraction speeds used in the 10-inch tests.

The reason we did not plan to conduct retraction tests for retraction lengths greater

than 14 inches is that although operational inertia reels generally provide 18 inches of strap length, the actual maximum retraction length is approximately 14 to 15 inches for a crew member who is grossly out of position in his seat. This situation would most likely occur in a multi-seat aircraft in which a crew member is unexpectedly ejected from an aircraft undergoing high "G" maneuvers or in an accidental ejection. Each test series would begin at a harmless level of speed and progress in increasing increments of severity.

To establish the expected maximum levels of the selected critical retraction parameters we ran a pre-test series using a 95th percentile anthropometric dummy and recorded these critical retraction parameters for each retraction phase. We then took the absolute maximums of these critical parameters and showed that they were below human tolerance levels (Ref. 5 and 6). During the human test program, we recorded these same critical parameters for each human subject and compared them to the values obtained from the tests using the dummy. With this technique we could compare the trends in data as we progressed to higher levels of test severity. This technique allowed us to see if the values obtained from the human tests were larger than those obtained from the tests using the dummy or if the trends were such that we could predict more severe readings for the humans at the next level and thus stop the tests. We required that all subjects be tested at each severity level before we advanced to the next level in order to insure all inputs were available before we made a decision to go to the next test level.

III. Experimental Apparatus and Procedure

The primary piece of test equipment was the Body Positioning and Restraint Device, BPRD (Ref. 1), located in the Protection Branch of the Aerospace Medical Research Laboratory (AMRL) at Wright-Patterson Air Force Base. This device is essentially a mock-up of an ejection seat that has a number of electronically-actuated, hydraulically-driven pistons and a control system housed in the area behind the seat. Each piston has a cable attached to it, and through pulley arrangements these cables are routed to various points where they can be connected to the test subject's body by a harness. Only the upper torso piston and cable were used in these tests, and Figure 1 shows a schematic of the BPRD test set-up. Figure 2 shows a subject on the BPRD in three positions during a typical retraction experiment. The positions shown are full forward, an intermediate position, and full back. Data sensor locations are shown and these sensors will be discussed in detail later. The harness-cable arrangement can be seen passing over the subject's shoulders and through the seat back.

To retract the subject a switch is thrown which actuates a solenoid, allowing the piston to be hydraulically driven and thus retracting the cable and the subject. Higher hydraulic pressures impart higher forces to the piston and result in faster retractions. Therefore, in these tests hydraulic pressure becomes a measure of retraction severity.

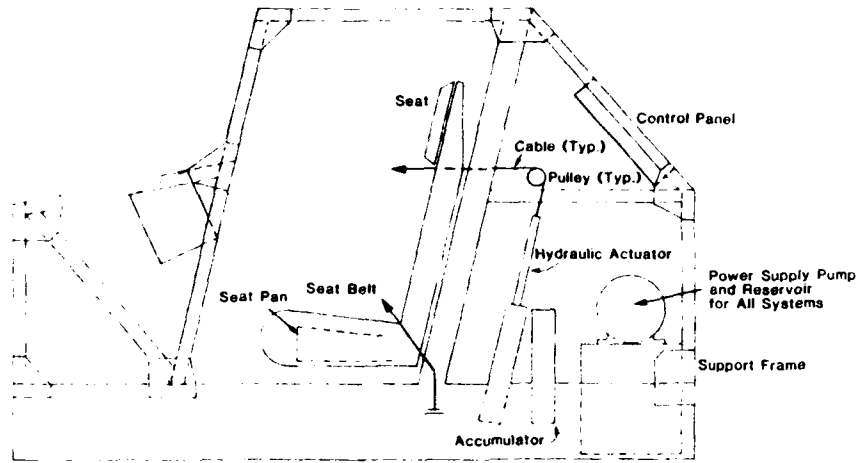


Figure 1. Body Positioning and Restraint Device (BPRD) Test Set-Up

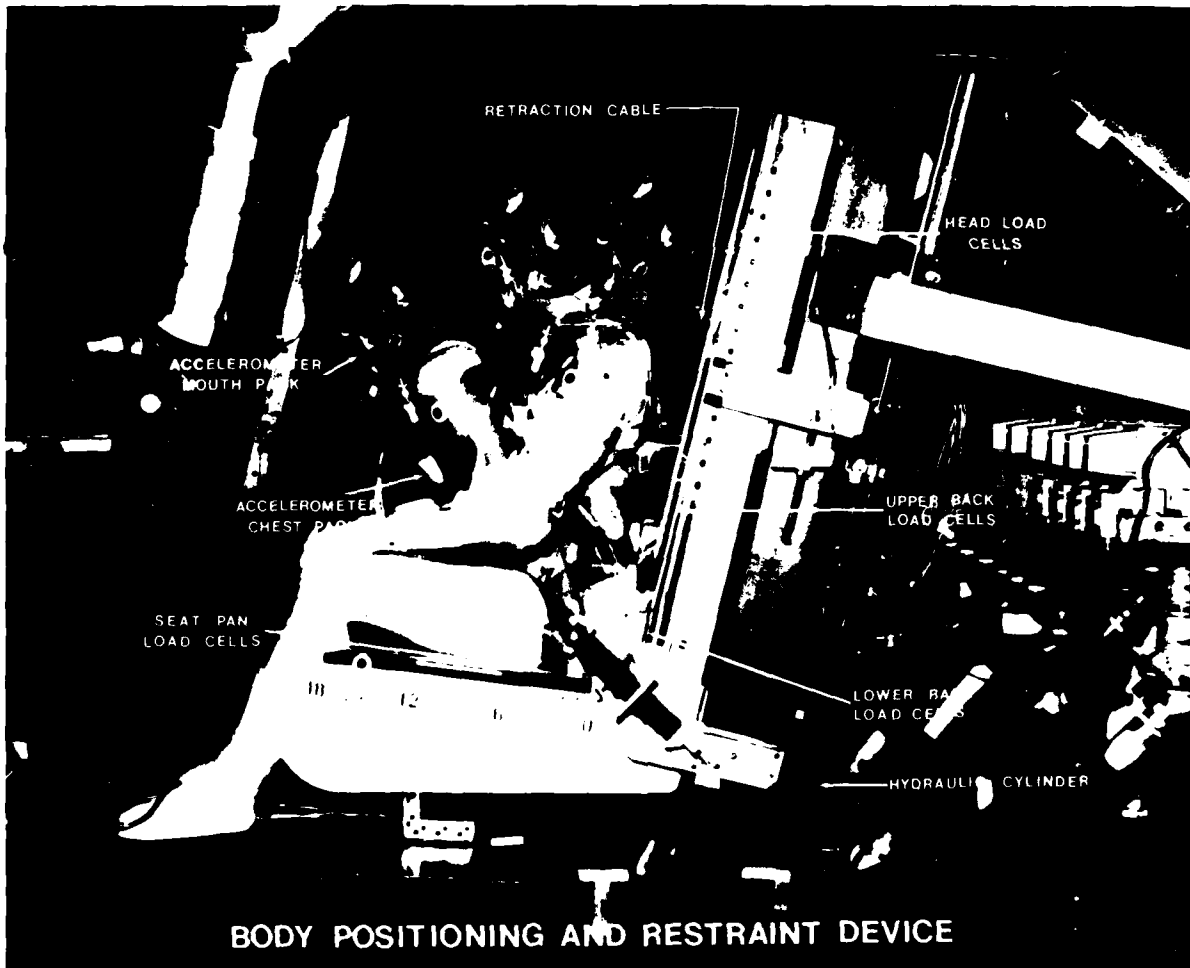


Figure 2. Subject on BPRD in Three Positions During Typical Retraction Experiment

The test procedure used in all tests is clearly spelled out by the BPRD Test Sequence Checklist which appears in Figure 3. This checklist was approved by the AMRL safety officer prior to testing and was followed exactly for all human tests. It essentially assures that (1) the subject is appropriately dressed and physically ready for the test, (2) the test instrumentation and equipment are operating properly, (3) all initial measurements have been taken, (4) the subject is properly positioned for the test, and (5) all test steps have been taken in the proper order. After the test, it assures that

BPRD TEST SEQUENCE TEST CONDUCTOR'S CHECKLIST	
1. Subject No.	19. Piston Position
2. Test No.	20. Blood Pressure
3. Subject Weight	21. Mouthpiece
4. Check ECG Signal	22. Helmet Strap Fastened
5. Cameras Loaded	23. Accel Cal/Zero
a. Side Cam No.	24. Subject Position (Preload)*
b. Lense No.	25. Cable Clearance
c. Leg Cam No.	26. Body Measurement
d. Lense No.	27. Pre-Test Photo
e. Front Cam No.	28. Bldg 40
f. Lense No.	29. Pressure Check
g. Frame Rate	30. Piston Length
h. f-Stop	31. Safety
6. Subject Arrival*	32. Clearance to Operator
7. Blood Pressure	33. Photo Ready
8. Chest Pack	34. Inst Ready
9. Harness Fit	35. Med Monitor Ready
10. Brief Subject	36. Subject Ready
11. Helmet Fit	37. Test*
12. Subject Seated	38. Post Test Med
13. Fiducial Placement	39. Post Test Photo
14. Pistons Retracted	40. Date
15. Harness Adjusted	41. Remarks
16. Subject Position	
17. Harness Attached	
18. Lap Belt Attached	*Record Time

Figure 3. BPRD Test Sequence Checklist

the subject's condition is checked and all post-test data are recorded.

As part of this procedure, the subject was asked to lean into the harness and apply a 10-to 20-pound preload to the cable to simulate the normal cable tension exerted by the inertia reel on an aircrew member in the cockpit. The actual value of the tension was displayed to the subject on a digital meter so he could adjust it. It should also be pointed out that we purposely did not reproduce one aspect of operational retractions with our experiments. In our tests, the subject was fastened to the retraction cable with the piston fully retracted, and the subject then adjusted his harness and seat belt for comfort. This harness adjustment technique then assures that no significant

afterload would be placed on the subject by the hydraulics after the piston is retracted. In the cockpit the inertia reel usually does produce an afterload. It should also be noted that a fully instrumented retraction test with a dummy was run as a check of the BPRD prior to the first human test of the day. Also, as a safety precaution, high-speed motion pictures from at least one test level were carefully reviewed prior to exposing subjects to the next test condition.

IV. Data

The data obtained from these tests can be divided into three separate categories: medical, electronic, and photographic. The specific measurements made in each of these categories are listed below.

A. Medical Data

1. Pre-test physical examination of subject
2. EKG and pulse before, during, and after the test
3. Blood pressure before and after the test
4. Post-test physical examination of subject
5. Subjective assessment of retraction severity by subject

B. Electronic Data

1. Chest acceleration in all three axes, resultant and chest severity index
2. Head acceleration in all three axes and resultant
3. Retraction cable force
4. Piston displacement
5. Piston velocity
6. Piston acceleration
7. Back impact force: three load cells
8. Head impact force: three load cells
9. Pelvis impact force: two load cells
10. Seat-pan force: three load cells

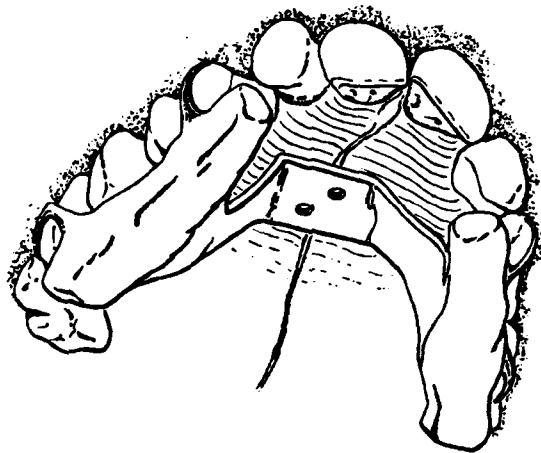
C. Photographic Data

1. Photometric data
2. Video recordings
3. Photographic stills

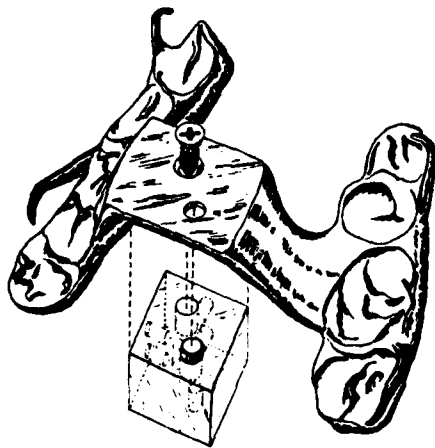
In this paper the only medical data we will comment on is the subjective assessment of the retraction severity made by the subjects.

We should note that summing of the load cell outputs attached to a particular surface will yield the total impact force on that surface, and cable force (harness load) is

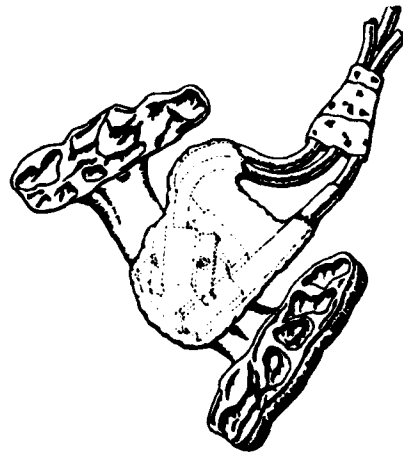
measured in the retraction cable by means of a load cell positioned under a pulley over which the cable is routed. The chest acceleration is measured by a triaxial accelerometer pack mounted on the xiphoid area using a belt arrangement. Head acceleration was measured using a newly developed accelerometer mouth mount. The triaxial acceleration package was attached to a metal mouthpiece as shown in Figure 4 (Ref. 7). Each of these mouthpieces were individually cast by the dental clinic at Wright-Patterson AFB to fit each subject's tooth pattern. The weight of the complete assembly (mouthpiece and accelerometer pack) is 50 grams.



A. Mouthpiece Attached to Subject's Teeth



B. Mounting Block Attachment to Mouthpiece



C. Assembled Accelerometer Mouth Mount
(Accelerometers and plastic mounting block are covered with an electrically insulating material)

Figure 4. Accelerometer Mouth Mount

A high-speed photographic film (nominal 500 frames per second) was used to determine body kinematics by individually tracking various points on the subject's body. This photometric data will not be discussed here. The video recordings (120 frames per second) were obtained with a television camera and were used by the principal investigator and medical monitor to review the body kinematics of the subject immediately after a test and prior to the next subject's exposure.

V. Test Subject Preparation

All of the subjects were volunteers from the AMRL Hazardous Duty Panel and demonstrated normal skull, spine, and chest x-rays, EEG, pulmonary function, treadmill exercise testing, and general physical examination. Use of these volunteers was in strict accordance with AFR 80-33 and its supplement.

The subjects wore leotards (which were dyed orange to enhance photographic coverage), AF flight helmets (HGU-26/P), and integrated parachute harnesses (PCU-15/P for males and PCU-16/P for females). The subjects donned their helmets and harnesses prior to mounting the BPRD.

Also, prior to testing, the medical investigator precisely identified various points on the subject's body for photographic tracking. A tape fiducial was then positioned over the spot. This procedure assured consistent fiducial location from subject to subject, and for the same subject from test to test.

VI. Experimental Tests

The tests described here were completed in two phases. Phase I was a pilot study done at low hydraulic retraction pressures (200, 300 PSI) to validate measurement techniques, evaluate potential human/test apparatus measurement techniques, check out data programming procedures, and to serve as an orientation experience for the volunteer subjects. These tests essentially repeated earlier tests performed at AMRL (Ref. 8). Phase II extended the studies from the harmless levels of the Phase I tests to retraction speeds comparable to those experienced operationally. Maximum retraction pressure reached in Phase II was 900 PSI. The retraction distance was 10 inches in all tests.

VII. Discussion of Results

Eleven human subjects, nine males and two females, participated in these tests, and they represent a wide range of sitting heights and body weights as shown in Table 1.

Each of these subjects were tested at each severity level (retraction pressure level), and Figure 5 is a series of photographs showing a typical retraction sequence. These photographs were taken from selected frames of the high speed film and display both the side view and the front view of the retraction event. These sequential photographs show subject F being retracted at the maximum severity level (900 PSI), and the times shown with the photographs correspond to an important event in the retraction

Table 1
SUBJECT SITTING HEIGHT AND WEIGHT RANGE

MID-SHOULDER SITTING HEIGHT RANGE		WEIGHT RANGE	
59.3 cm to 68.0 cm		118 lbs to 210 lbs	
5 percentile	60.2 cm	5 percentile	140 lbs
95 percentile	69.2 cm	95 percentile	210 lbs

sequence. For example, Figures 5c and 5f show the subject's position at the point where the retraction piston has just been fully retracted. This retraction time can easily be determined from the displacement transducer data shown in Figure 6. The piston retraction time, then, is the time elapsed from the beginning of piston motion to the point where the piston is full down (designated as Point 3). Similarly, the other event times can be determined from the load cell output, as shown in Figure 7. It is interesting to note here that the peak cable force coincides with the peak seat-pan load, which indicates that the subject is not only pulled back into the seat, but is also pulled down into the seat. Notice that Point 4 is selected to be the point where seat back load reaches its peak.

The chest acceleration for this test is shown in Figure 8. This figure shows that the maximum chest acceleration for this test is 12 G's and occurs during the onset of cable loading when the chest is being accelerated and again when the torso impacts the seat back and is being brought to rest.

The subject's head acceleration for this test is shown in Figure 9. Here the maximum resultant acceleration is 11.5 G's. This is the acceleration value that was used to compare head acceleration severity between the various subjects for the composite results as discussed below.

Individual results such as those just discussed were recorded for each subject at every test level and were then plotted in comparison to the test data obtained using the dummy subject. These composite results for piston retraction time, for example, are shown in Figure 10, where the abscissa represents the hydraulic pressure level or the retraction severity level. The data indicates clearly that increasing the pressure, i.e., the force applied to the piston, results in a faster retraction, as we expected. The body retraction time was defined as the time from the onset of cable force to the peak of seat back force. This appeared from our tests to be a reasonable criterion for completion of retraction. Cessation of head motion or head orientation was not used as a measure of completion since some subjects had continued head motion past this point, ending with upright head posture, while others maintained a head-forward position. In either case, head motion or position would seem to be an inappropriate criterion for

Front
View

Side
View



5A

1
Initial
Position
t = 0 msec



5D



5B

2
Peak
Cable
Force
t = 50 msec



5E



5C

3
Piston
Retracted
t = 101 msec



5F



5D

4
Back
Force
Peak
t = 128 msec



5G



5E

5
Final
Position
t = 227 msec



5H

Figure 5. Subject F's Retraction Sequence at Maximum Retraction Level (900 PSI)

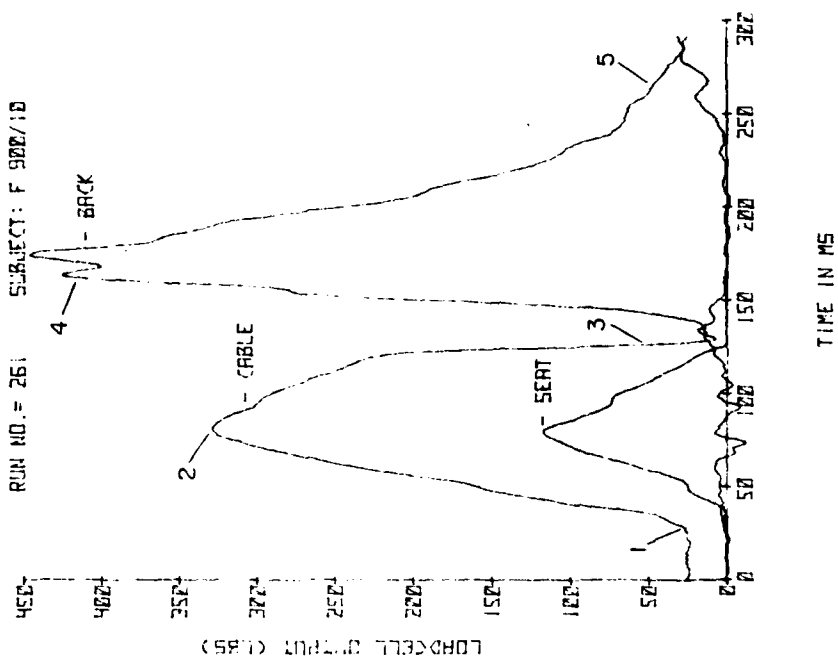


Figure 7. Various Force/Time Histories During Retraction and Impact

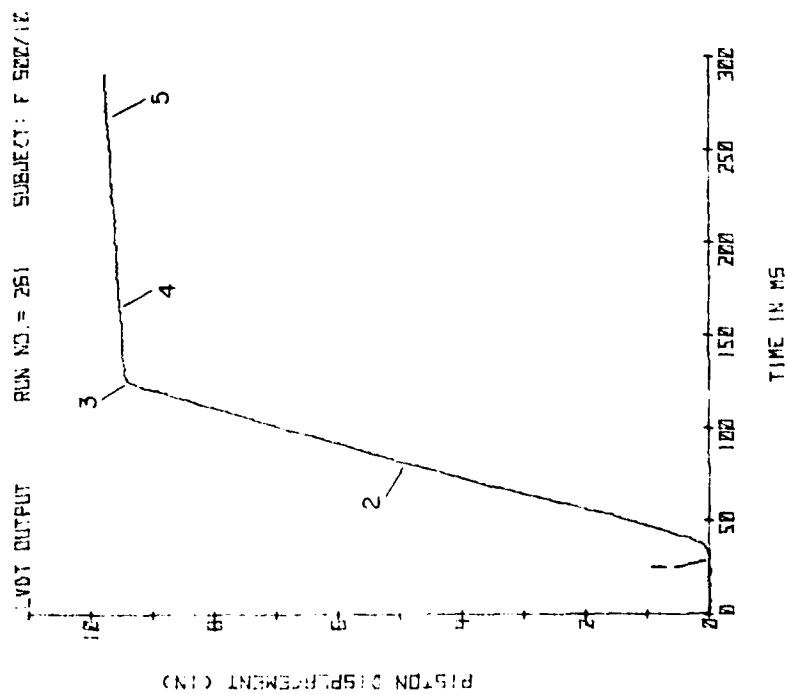


Figure 6. Retraction Piston Displacement Versus Time

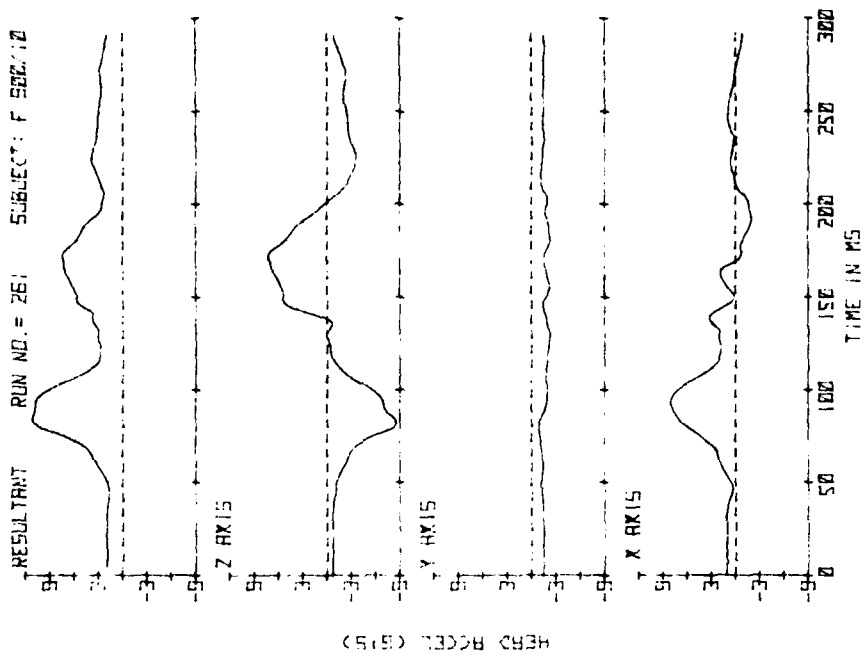


Figure 8. Chest Acceleration Recorded for Subject F at Highest Severity Level (900 PSI)

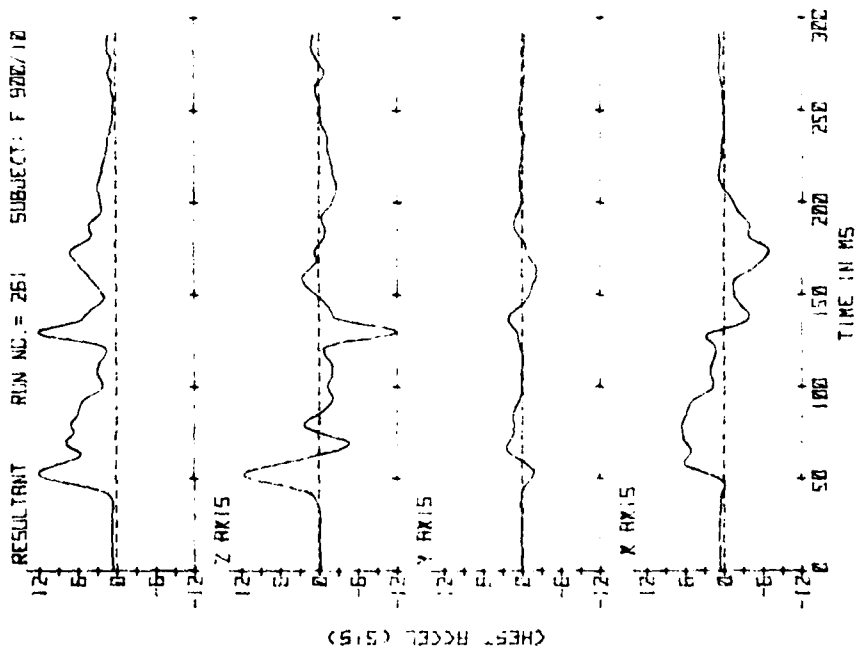


Figure 9. Head Acceleration Recorded for Subject F at Highest Severity Level (900 PSI)

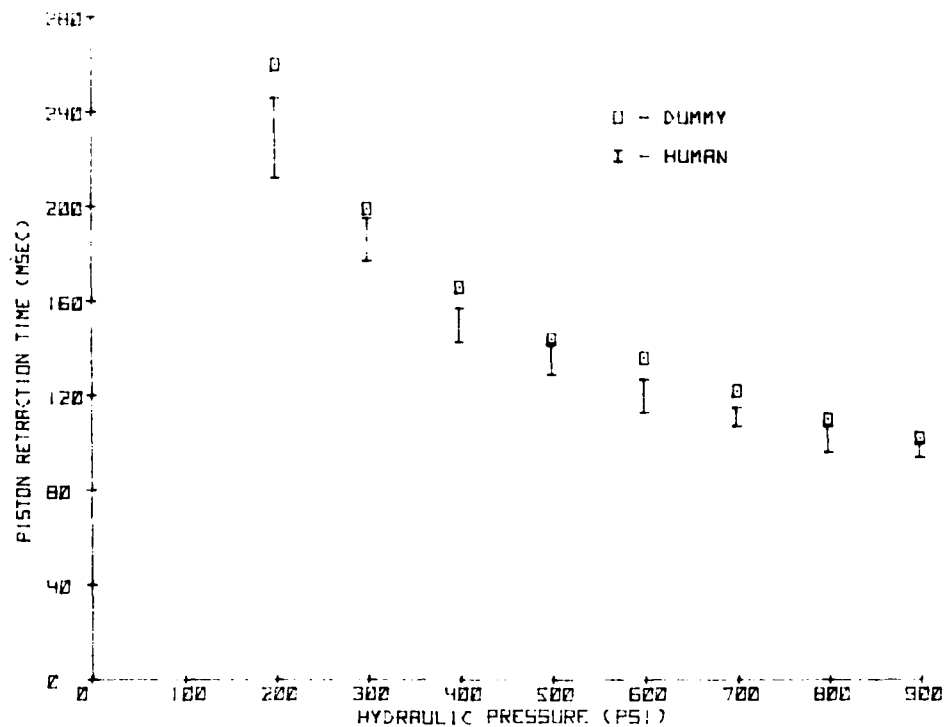


Figure 10. Composite Piston Retraction Times

measuring sequence completion. For example, if we consider the retraction situation where the subject's torso is already on the seat back, the retraction would certainly end when the harness is tightened (the peak back force point), and head motion would not be a consideration.

Figure 10 also shows that at the higher pressure levels we have reached a point of diminishing returns. Notice also that the human is always retracted more rapidly than the dummy, although at the higher pressures the difference becomes insignificant.

The female subjects had lower body mass and were, therefore, retracted more rapidly. Their piston retraction time was always at the lower end of the range shown in Figure 10, whereas the largest male was always near the top of the retraction time range.

The maximum cable force obtained for each subject at each level is shown in Figure 11. Here, as expected, cable force increased with pressure level. Note that the human peaks are always less than the data for the dummy. For the human subjects, the large males always experienced the largest cable forces and the females the smallest. This is consistent with results of the piston retraction behavior since a larger mass requires greater force to accelerate it.

The maximum seat-pan force obtained for each subject and the dummy are shown in Figure 12. Three load cells were used to measure the seat-pan load and the values plotted in Figure 12 represent the sum of those load cells. The load cells were set to zero

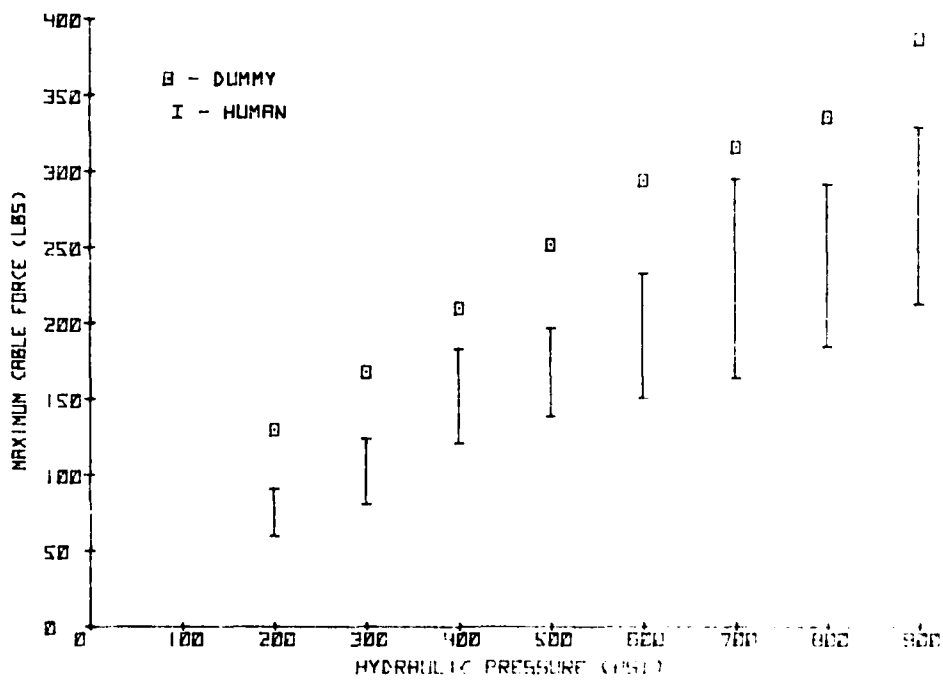


Figure 11. Maximum Cable Force at Each Pressure Level for All Human Subjects and Dummy

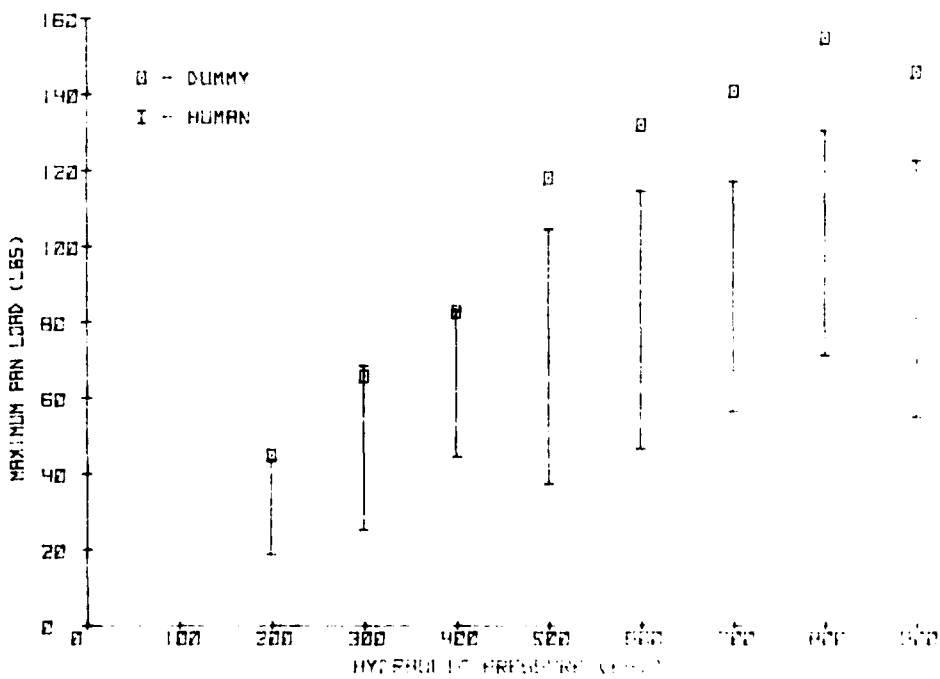


Figure 12. Seat-Pan Load for Each Pressure Level for All Human Subjects and Dummy

prior to the retractions to remove the effect of body weight so that the values obtained would reflect only the down-loading on the spine due to the retraction process. Figure 12 clearly demonstrates that this loading does occur and reaches a maximum value of approximately 130 pounds. This value, however, is below the values for the dummy and well within human tolerance.

The composite chest acceleration results are shown in Figure 13 and demonstrate that the humans experienced significantly lower values of maximum acceleration than

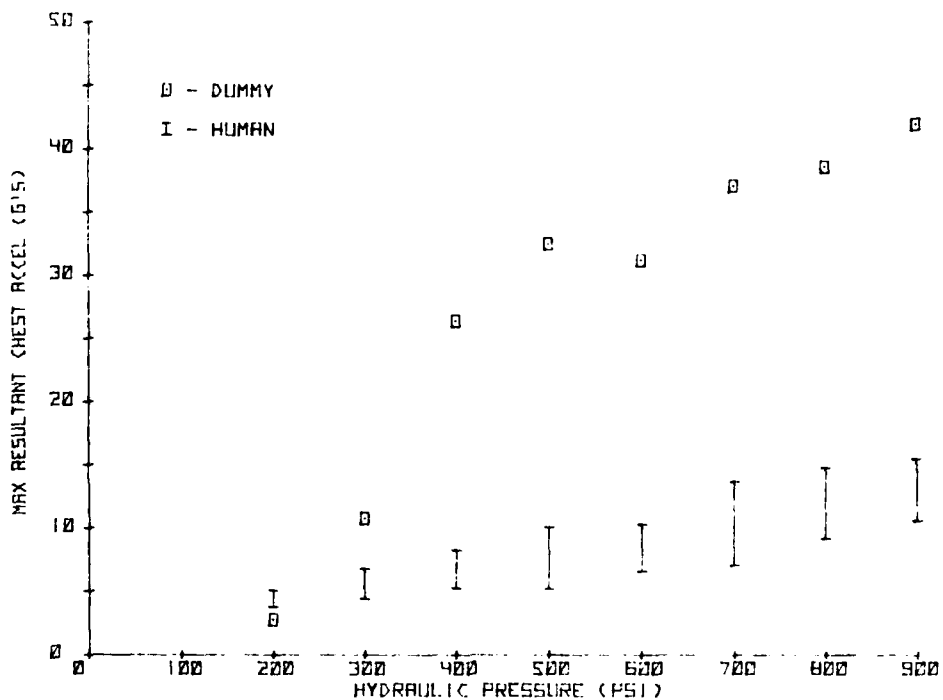


Figure 13. Maximum Chest Accelerations at Each Pressure Level for All Human Subjects and Dummy

the dummy. This data also demonstrates the nonlinear trend of the dummy's chest acceleration which we were afraid we might encounter in the tests of humans. Our concern, of course, was that although all test results from one test level would be well within tolerance limits, a large increase in test severity could occur between test levels because of the nonlinear behavior of the biological system, and we would therefore expose the test subject to possible injury. The human data, however, is approximately linear and demonstrates a fairly small range in resultant acceleration peaks at each level of hydraulic pressure.

The composite head acceleration results shown in Figure 14 demonstrate a similar trend. Here again, the dummy experienced much higher levels of acceleration than the human subjects. This was primarily due to the dummy's head impacting the headrest of

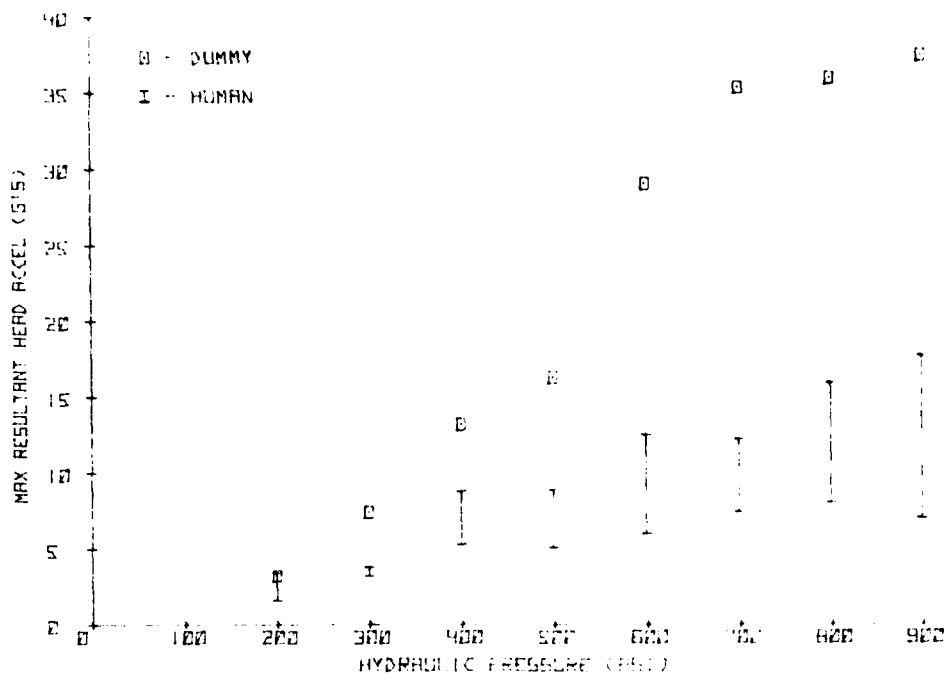


Figure 14. Maximum Head Acceleration at Each Pressure Level for All Human Subjects and Dummy

the seat. These impacts began at retraction pressure levels of as low as 400 PSI, and at the higher levels of retraction pressure these impacts were quite severe. In fact, some of these impacts were so severe that helmet fractures occurred. Our risk analysis indicated that the active muscular effects of the human neck would significantly reduce the head motion and thereby provide safe exposure. Our human tests at low pressure levels confirmed that the acceleration levels of the dummy head were significantly higher than those of the human volunteers.

We therefore proceeded with our tests using the stepped retraction procedure previously discussed. To our surprise, we observed no head impacts of the humans at all, even at the highest pressure levels. As Figure 14 indicates, the maximum resultant human head acceleration was less than one-half of the dummy's at the maximum severity level. This result once again demonstrated the importance of continued human testing. Data obtained from these tests can be used to complete optimal system designs that are demonstrably safe, whereas data from tests utilizing dummies, human cadavers, or animals would indicate injuries at these levels and lead to system designs that are not only overweight and difficult, but which also degrade system performance.

VIII. Summary and Conclusions

The results of these tests indicate that retraction of the human torso in a one-G field can be safely performed in significantly less than 300 milliseconds. The means

and standard deviations of the various retraction test parameters are shown in Table 2. Remember that the retraction time was defined as the elapsed time between the onset of cable force to the point where maximum seat back force occurred.

Table 2
RETRACTION TEST PARAMETERS
(Tabulated values are experimental means with
the standard deviation in parentheses)

TEST PARAMETERS	RETRACTION LENGTH 10 INCHES	
	600 PSI	900 PSI
Retraction Time (milliseconds)	148 (8.2)	134 (11.5)
Peak Cable Force (lbf)	185 (24.3)	250 (28.5)
Average Reel Retraction Velocity (in/sec)	77.9 (2.4)	97.4 (2.7)
Peak Seat-Pan Force (lbf)	75 (18)	102 (23.4)
Peak Back Force (lbf)	354 (71)	466 (70.6)
Peak Chest Acceleration (G's)		
Retraction	7.2 (1.4)	11.6 (1.5)
Seat Back Impact	7.5 (1.2)	11.9 (1.9)
Peak Head Acceleration (G's)		
Retraction	7.1 (1.8)	11.7 (3.0)
Deceleration	5.9 (2.3)	10.2 (3.3)

All of the measured parameters are well within human tolerance limits. The subjects tolerated the tests well at all severity levels, and considered the tests to be harmless even at the highest severity level.

We conclude then, that for for 10-inch retraction distances, times much less than 300 milliseconds are required for upper torso retraction.

The next step in this testing process will be to complete a test series of upper torso retractions at longer distances of up to 14 inches to determine if equivalent retraction time reductions can be obtained for retraction distances equalling the maximums encountered in operational retractions. If so, then it seems possible that a significant improvement in crew survival can be realized through a reduction in the initial time delay that occurs between ejection system initiation and actual seat motion.

References

1. Phillips, H. S., et al. "An Investigation of Automatic Restraint and Body Positioning Techniques." AMRL-TR-71-101, December 1973.

2. Military Specification MIL-S-9479B (USAF). "Seat System, Upward Ejection, Aircraft, General Specification for," March 1971.
3. Technical Need. Aeronautical Systems Division, Systems Command, USAF. TN-ASD-AMRL-0607-78-63(1). Crew Positioning Restraint System, 1978.
4. Carter, R. L. "Human Tolerance to Automatic Positioning and Restraint Systems for Supersonic Escape." North American Aviation, Inc., Report No. NAS9H-220, April 1959.
5. Human Use Protocol, No. 77-21. "Rapid Pre-Ejection Restraint Test Medical Protocol." On file: Aerospace Medical Research Laboratory (AMRL/BBP), Wright-Patterson AFB, Ohio 45433.
6. Human Use Protocol, No. 78-03. "Protocol for the Development of Design Criteria for Rapid Pre-Ejection Crew Restraint of Upper Torso: Phase II. Intermediate Speed Retraction Tests." On file: AMRL/BBP Wright-Patterson AFB, Ohio 45433.
7. Higgins, A. M., et al. "Mouth Mounted Accelerometer Pack." United States Patent, No. 4,189,990, April 1980.
8. Human Test Data, AMRL, Protection Branch. Log book and movies of tests on file. Tests performed April through August 1971.

USAFA-TR-81-4

SECTION IV

Engineering Education

SI UNITS (MASS?, WEIGHT?)
LET'S DO IT RIGHT

R.F. Felton*

A few years ago the United States began in earnest to change from the English system of units to the new International System of Units (SI units). Those who encouraged the change had high hopes that some of our bad habits in using the English system would disappear in the change, but alas, it seems that the American public still does not understand the difference between mass and weight. This paper examines the concepts of mass and weight by using force to explain the origin of the difficulty in understanding the correct relationship between mass and weight.

I. Introduction

In 1960 the United States, along with 36 other countries, took part in officially establishing the "Système International d'Unites" or the International System of Units (SI units). Although the United States government intended to rapidly switch from use of the English system of pounds, feet, and seconds to the new SI units of kilograms, meters, and seconds, the change has been slow in coming. It is only in recent years that the change has really made itself felt. Unfortunately, some of our bad habits with regard to our concepts of mass and weight, which we had in the English system of units, have found their way into the new world of SI units. In fact, the problem is even more severe in SI, since people do not yet have a feel for the new units.

This confusion between the concepts of mass and weight results from the fact that most people, including many engineers and scientists, do not really understand the English system of units. And it is no wonder, since there is more than one English system of units. Units (i.e., man's attempt to put weights and measures on some relative scale) were first developed by people in order to communicate and conduct their business with others. There are only a few fundamental units (sometimes referred to as standard or base units). These fundamental units are physical creations of man upon which all measurements depend. For example, the unit for the dimension of length is a fundamental unit. All the other units are derived from fundamental units through the use of equations (relationships that explain observed phenomena). For example, the unit for velocity is a derived unit ($\text{velocity} = \text{length}/\text{time}$; both length and time are fundamental dimensions and as such have defined fundamental units, and velocity is derived from this relationship). A number of different unit systems have been developed over the years (Ref. 1). In all these systems, it was necessary for someone to define the few fundamental units. The actual definitions of these fundamental units are not crucial to the problem of understanding the difference between mass and weight; the important thing is that there are units that are fundamental and are defined to be a certain thing by agreement between individuals.

*Colonel, USAF, Tenure Professor and Head of Aeronautics Department

II. Mass, Weight, and Force

A. Mass

What is mass? In all unit systems, mass has been taken as a fundamental or base unit. Mass is a measure of the inertia of a body, that is, a body's resistance to acceleration. In a sense, mass is the actual body itself, a characteristic of the body that is independent of its location. Thus, a body will have a certain constant mass, regardless of whether the body is on the earth or on the moon. Again, by agreement, a particular body, a platinum-iridium cylinder, was defined as having a certain mass, and the masses of all other bodies are determined by comparing them to this standard body. The most common method for measuring the mass of a body is the beam balance. By using a beam balance, the mass of the body is equal to the sum of the known masses used to balance the beam to a zero position.

B. Weight

What is weight? Weight is a measure of the attraction that one body (for instance, the earth) has for the mass of another body. The defining equations that allow one to determine this force of attraction are credited to Isaac Newton. Newton's law of gravitation states that the force acting on a body of mass m is proportional to the mass of the body times the mass of the second body, m' , and inversely proportional to the distance between their gravitational centers squared, r^2 . In equation form this relationship is expressed as follows:

$$F_g = G \frac{m m'}{r^2} \quad (1)$$

where F_g is the symbol for the force acting on the body, and G is a proportionality factor. The numerical values of F_g , G , m , and r depend on the choice of a system of measurement units. For example, F_g might be expressed in one of the following ways: dyne, newton, poundal, or pound-force. Since we are accustomed to measuring weight on the surface of the earth, m' and r remain essentially constant, and we may combine G , m' and r^2 of Eqn. (1) into a simpler form:

$$F_g = kmg \quad (2)$$

where F_g is quite often given the symbol W , representing weight, k is a constant of proportionality dependent on the system of units used, and g is the so-called "acceleration of gravity." The value of g varies slightly on the earth, and different values of g could be derived from Eqn. (1) for the moon or elsewhere. Again, the numerical values of F_g , k , m , and g depend on the system of units being used.

C. Force

We usually think of force in terms of an ability to accelerate a mass. Again, we are indebted to Newton, for it is Newton's second law that expresses this relationship:

$$F = kma \quad (3)$$

where F is the symbol for the force, k is the same constant of proportionality as in Eqn. (2) (again dependent on the unit system), m is again the mass on which the force is applied, and a is the acceleration or change in velocity of the body with time.

Unit systems take two fundamentally different forms based on whether Eqn. (2) or Eqn. (3) is chosen to define the units of force. In those systems in which Eqn. (3) is used to define the units of force, mass has a defined unit, as do length and time, but the unit of force is a derived unit, that is, the unit of force is defined by Eqn. (3). Notice that if we choose the proportionality factor, k , to be 1, then $F = ma$, and an absolute unit of force is defined as the force that, when acting upon one unit of mass, will produce one unit of acceleration. Table 1 lists a few systems of units in which the unit of force is an absolute unit and is derived from $F = ma$.

There are systems of units based on Eqn. (2) and which use the earth's gravity as a standard. The force of attraction of the earth on the mass of a body on or near the earth's surface is easy to observe, and a number of individuals decided that it would be convenient to have a system of units that made use of this observation. Since the force of attraction for a given mass depended on the location (refer to m' and r of Eqn. (1)), it is necessary to define this force at a specific location, and then use it as a standard. It was decided that the force of attraction would be defined at sea level and at 45 degrees north latitude, such that its numerical value would be equal to the numerical value of the mass of the body. This definition for force is referred to as the gravitational unit of force. Thus, in this system force, mass, length, and time all have defined base units, and the proportionality factor, k , is no longer 1. Table 2 lists a few systems of units in which force is a gravitational unit.

D. Mass and Weight . . . There Is a Difference

Since the force of attraction (force of gravity) is referred to as weight, W , then $W = mg$ if an absolute system of units is used, and $W = kmg$ if a gravitational system is used. Take as an example a person whose mass is 200 pound-mass (lbm), then the weight of the person on the earth would be 6434 poundals if $W = mg$ is used ($W = 200 \times 32.17$); or 200 pound-force (lbf) if $W = kmg$ is used ($W = 1/32.17 \times 200 \times 32.17$). Thus, when the gravitational system is used, one finds that the numerical value of weight can be equal to the numerical value of mass if the proper units are used (assuming, of course, that one neglects the small variation in the value of g over the earth's surface). But, the units are not the same; that is, it is true that 200 equals 200, but 200 pound-force

Table 1
UNIT SYSTEMS BASED ON AN ABSOLUTE FORCE UNIT ($F = ma$)

SYSTEM	BASE UNITS (partial list)			DERIVED UNITS (only force is listed)		
	NAME	UNIT	SYMBOL	NAME	UNIT	SYMBOL
cgs Units	mass length time	gram centimeter second	g cm s	force	dyne	
English Units	mass length time	pound-mass foot second	lbm ft s	force	poundal	
English Engineering Units	mass length time	slug foot second	sl ft s	force	pound-force	lbf
SI Units (International System of Units) Note: this is the new worldwide system of units	mass length time	kilogram meter second	kg m s	force	newton	N
<p>Examples: A one pound-force (1 lbf) is derived from $F = ma$ to be that force that when acting on a mass of one slug (1 sl) will produce an acceleration of 1 ft/s^2.</p> <p>A newton is derived from $F = ma$ to be that force that when acting on a mass of one kilogram (1 kg) will produce an acceleration of 1 m/s^2.</p>						

is not equal to 200 pound-mass. Force and mass are different things; saying that 200 pound-force equals 200 pound-mass is like saying 200 apples equals 200 oranges.

Because of space travel, most people realize that there is a difference between mass and weight. They know that one's weight on the moon is approximately one-sixth of that on earth, but that one's mass on the moon is the same as on the earth. However, most people just state that their weight is 200 pounds rather than 200 pound-force. This normally doesn't cause any problems when the earth's gravitational system is used. But with an absolute system one must make a distinction between mass and weight.

Table 2
UNIT SYSTEMS BASED ON A GRAVITATIONAL FORCE UNIT ($F = kma$)

SYSTEM	BASE UNITS (partial list)			VALUE OF k	
	NAME	UNIT	SYMBOL	NUMERICAL VALUE	UNITS OF k
English Engineering Units	mass length time force	pound-mass foot second pound-force	lbm ft s lbf	$\frac{1}{32.17}$	$\frac{lbf \cdot s^2}{lbm \cdot ft}$
cgs Units	mass length time force	gram-mass centimeter second gram-force	g_m cm s g_f	$\frac{1}{980.62}$	$\frac{g_f \cdot s^2}{g_m \cdot cm}$
mks Units Note: this is <u>not</u> the system of units that the world is changing to	mass length time force	kilogram- mass meter second kilogram- force	kg_m m s kg_f	$\frac{1}{9.8062}$	$\frac{kg_f \cdot s^2}{kg_m \cdot m}$
<p>Example: A one pound force (1 lbf) has been defined as a force equal to the attraction of gravity on a one pound-mass (1 lbm) at sea level and 45 degrees north latitude. A 1 lbf acting on a 1 lbm will produce an acceleration of 32.17 ft/s².</p>					

The new SI units is an absolute system of units (Ref. 2), and one must not confuse mass and weight (force). In SI units, the unit for mass is the kilogram (kg), and the unit for force is the newton (N). Thus, for the person whose mass is 200 pound-mass, the mass in SI units is approximately 90.7 kilograms (see Table 3). The weight of the person would be 889 newtons, where one uses $W = mg$ ($W = 90.7 \times 9.8$). Hence, there is a difference between mass and weight, so be careful and correct. You can talk about your mass in kilograms, but your weight is in newtons. Most people will undoubtedly talk about their mass, since it is a smaller number; however, if you are on a diet, it will be harder to lose mass than it would be to lose weight. For example, for the person whose mass was 90.7 kilograms and whose weight was 889 newtons, it will be easier to lose 1 newton than to lose 1 kilogram.

III. Conclusion

All of the unit systems mentioned in this article, plus several more, are currently

Table 3
 HELPFUL CONVERSION INFORMATION
 (approximate values)

MASS	FORCE
1 kg = 1000 g	1 lbf = 32.17 poundals
1 g = 0.0022 lbm	1 N = 0.02248 lbf
1 slug = 32.17 lbm	
1 g = 0.0353 ounce*	

*avoirdupois

in use in the United States. Needless to say, these units have caused a great deal of confusion, and have caused people to make many errors. The desirability of having only one unit system is obvious. The new SI unit system is superior to any other system of units, and many European countries are converting to it. Often referred to as the metric system, SI is a new system, even though it does contain a number of aspects of the old metric system. It just happened that the U.S. was late in realizing that if we wanted to communicate with the rest of the world, then we had to convert to SI units. In fact, the U.S. cannot afford not to convert to SI units if we want to conduct business on a worldwide basis. But, let us do it right and try to avoid embarrassments like the one shown in Figure 1, which appears on the back of a ruler from the Bureau of Standards (of all places).

COMPARE METRIC AND CUSTOMARY UNITS				Metric Units are in 10's 1000 millimeters = 100 centimeters = 1 meter 1000 meters = 1 kilometer	U.S. DEPARTMENT OF COMMERCE National Bureau of Standards Washington, D. C. 20234 NBS Special Publication 376 Issued December 1972 For sale by the Superintendent of Documents, U.S. Government Printing Office, Washington, D. C. 20402 Order by SD Catalog No. C13 10 3761 Price 25 cents.
Metric	Meter	Liter	Kilogram		
Length				1 meter = 1.1 yards	
Volume				1 liter = 1.1 quarts	
Weight				1 kilogram = 2.2 pounds	
Customary	Inch	Teaspoon	Grain		
	Foot	Tablespoon	Ounce		
	Yard	Cup	Pound		
	Rod	Pint	Ton		
	Mile	Quart			
		Gallon			

Figure 1. Back of a Ruler from the National Bureau of Standards
 Expressing Weight in Kilograms
 (Notice this is not consistent with SI units)

References

1. Klein, H. A. The World of Measurements. New York: Simon and Schuster, 1974.
2. Standard for Metric Practice. ASTM E 380-76E, 1 EEE Std 268-1976, ANS Z 210.1-1976.

USFA-TR-81-4

SECTION V

Aeronautical History

THE EARLY HISTORY OF THE JET ENGINE

Sir Frank Whittle*

Editor's Note

Sir Frank Whittle independently developed the first successful turbojet engine for the Allies during World War II. His interest in jet engines began while a cadet at Cranwell in 1928, and he patented his early ideas in 1930. Through his persistence these ideas, first rejected as impractical, were eventually accepted by the British Air Ministry. With Whittle as its head, the subsequent program led to not only an operating turbojet engine, but also to a successful jet-powered aircraft, the Gloster-Whittle E-28/39. The paper that follows is Sir Frank Whittle's account of those pioneer days as he presented it to the faculty and cadets of the United States Air Force Academy on March 13, 1975.

Well, gentlemen, as a graduate of Cranwell it's a great pleasure to be speaking at the Air Force Academy, and I compliment you on your smartness. I don't think we can do better at Cranwell, [but] I wouldn't guarantee it.

Well, all this jet business started at Cranwell, though you young folks, of course, probably can't believe that there was a day when the jet engine didn't exist, and you must wonder how it was that it took so long to think of such a simple idea and why there was so much trouble about getting it going. Well, I'll try and explain all that.

I didn't actually think of the turbojet while I was still at Cranwell, but it had its origin there because each term we had to write a thesis. In my first three terms, I wrote a three-part thing on chemistry in the service of the RAF. It dealt with bombs and high explosives and poison gases, and in my fourth term I chose the rather ambitious subject of future developments in aircraft design. . . I worked out a formula for range and speed, connecting range and speed, and engine efficiency and lift-drag ratio of the airplane, which I afterwards found out was quite a well-known formula, known as the Breguet formula. And I was very disappointed to find out that whatever you did for a given engine efficiency and a given lift-drag ratio, you couldn't increase the range. But it did show that if you wanted to fly both fast and far, you had to fly very high, in the stratosphere. So I set out to try and find a power plant which would work in the stratosphere, which the piston engine would not do. And at a speed of 500 miles and hour, the propeller wasn't much good because of the high Mach numbers.

Well, I thought about rockets, and the fuel consumption, of course, is much too high for an airplane. And I took a look at gas turbine-driven propellers, but, of course, there the trouble was, as I just mentioned, the propeller. So I kept on working away after I graduated from Cranwell. While I was a pilot in 111 Squadron, I thought of a piston engine inside a hollow fuselage, driving a low pressure compressor producing a jet - the same idea that the Italians produced in 1940; I think it was the Caproni - Campini's scheme. But, when I worked out what the fuel consumption was and so on, it didn't seem to me to be of much good.

*Air Commodore, RAF (ret)

Then, when I was undergoing training as a flying instructor at the Central Flying School, I suddenly felt, "Well, why not throw the piston engine away and substitute a turbine and drive a high pressure compressor instead of the low pressure compressor," and that was the turbojet.

Now I should, in all fairness, say that I was not the first to think of the turbojet as an engine. There was a Frenchman named Maxime Guillaume who took out a patent in 1921. Of course, it was long before its time.

Whatever happened to Maxime Guillaume I never knew, and whatever he did about it, I don't know. But anyway, I got a patent in Britain in 1930, after the Air Ministry had turned the thing down. They had already made up their minds that the gas turbine was a dead duck, and all the firms I tried to sell the idea to decided that the gas turbine wouldn't work.

I took out the patent and got it, and the first [figure] shows that (Figure 1). I am showing this because . . . it isn't very representative of what a jet engine really looked like, but unfortunately I haven't got with me a picture which shows a section of the early engines. But this patent drawing does give some clue as to what form the engine was going to take.

At the top is the pressure volume diagram for the stationary condition, and the curve - it's off the picture, I'm afraid - the Curve D to C, I think it is, represents the way the pressure is increased and volume reduced in the compression process, and from C to E you see the increase in volume due to heating in the combustion chamber at constant pressure. And then from E to F is the expansion, the drop in pressure through the turbine, enough to drive the compressor, and then that leaves F to G as the balance of energy for producing the energy of the propelling jet.

The machinery for doing the job is shown here very crudely. I was sitting on a fence where the compressor was concerned. Two stages of axial-flow compressors were followed by a single-stage centrifugal, a multiple combustion chamber system, a two-row Curtis turbine, and then the multiple exhaust nozzles. Of course, in practice we only use one.

This drawing was deliberately made to look a little bit, I would say, "childish," because I thought the thing ought to be on the secret list, so I thought the best thing was a drawing that was good enough for patent purposes, but which wouldn't give away too much to anyone who got hold of the patent.

Well, nothing happened for five years, and no one would believe it. You see, the great problem was this: in those days the efficiency of compressors was so poor that, say if you needed 1000 horsepower, ideally, in fact, you had to use 1500 horsepower to drive it. And turbine efficiencies were low too, so where ideally a turbine might pro-

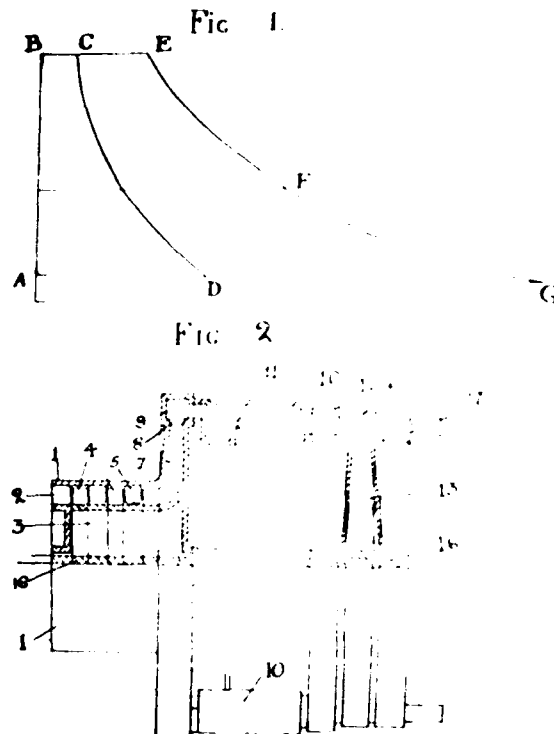


Figure 1. The Turbojet Engine in Whittle's 1930 Patent

duce, say, 2000 horsepower, it only produced 1500. So when you deducted the work required to drive the compressor from the work produced by the turbine, you didn't have much left. In fact, you were very lucky if the thing would even turn itself over.

And incidentally, what we call the positive/negative ratio and the work depended very much on the maximum temperature you could use in the turbine, and that in turn was governed by the materials available, and that was a very severely limiting factor. But I was pretty confident that we would get materials which would stand the temperature, and I was even more confident that I could improve compressors and turbines so that this big objection to the gas turbine would disappear. And I further realized that as we got bigger, the cold air of high altitude would make a very big difference to the prospects where efficiency was concerned.

Well, as I said just now, I was very confident about being able to get an efficient compressor. . .too confident, I will admit. I was equally confident to do much better on the efficiency of the turbine, but I was far from sure that we would get satisfactory

combustion, and that did in fact prove to be our biggest difficulty. And this [figure] (Figure 2) shows you the kind of conditions we had to work under in trying to develop the combustion system.

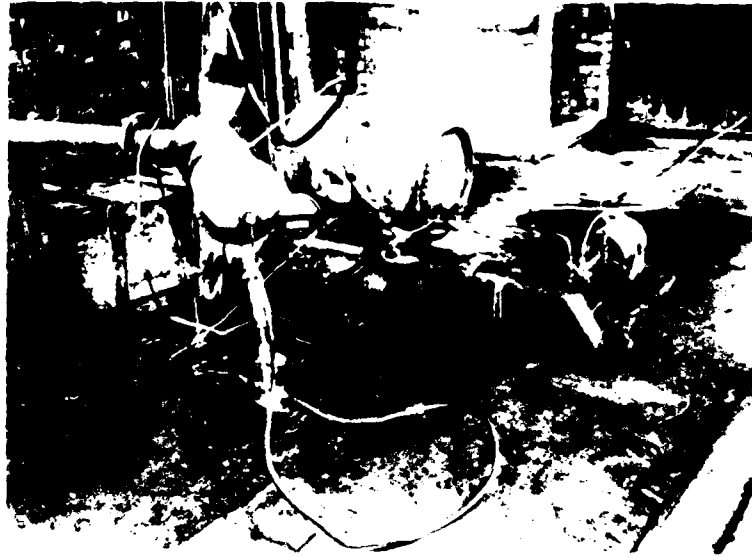


Figure 2. Early Laboratory Used to Develop the Combustion System

This was outside the BTH turbine factory, in the open air. Above it there was an office where the planning engineers and their staff worked, and we were most unpopular with them because that thing here (see Figure 2) is the combustion chamber, that's the fuel container, and here is a motor driven fuel pump, and the burner was in here.

Well, that thing used to behave more like a machine gun than a combustion chamber. In fact, on one occasion, the people in the office above had gone away to lunch, and when they came back and found that everything on the desk - the inkpots, their pens, papers, and everything else - was on the floor, they thought some practical joker had been around and done all this, until we started it up, and of course the concussions coming up from below were causing everything to "walk" in the office. On other occasions we smoked them out.

Well, the whole job was hung up for five years because nobody would take any interest in it, but it did happen that someone who had been a cadet with me at Cranwell - this is very much an Air Force job, you know - Williams (he is now Sir Dudley Williams), he was in my term at Cranwell, and we were in the same hut together, and he knew about the thing. In the Royal Air Force, later on, it was rather jokingly referred to as "Whittle's flaming touchhole." No one took it very seriously, but after five years Williams and another officer who had been invalided out after a bad crash, came along and said they thought they could raise some money. They managed to interest a firm of city bankers,

and a little company called Power Jets Limited was formed. At the time, I was at Cambridge University being trained as an engineer officer following my flying career. We managed to get enough money to start the company, and we got enough of it to put an order with the British Thompson Houston Company to build an engine to my design while I was still at Cambridge.

The Air Ministry still didn't believe in it, but fortunately, the Air Member for Personnel agreed to let me stay at Cambridge for a post-graduate year, knowing that in reality I was working on the job, though on paper I was doing aerodynamics research for Professor Jones - Sir Melville Jones, as he was later. I was, in fact, doing research work with Sir Melville Jones, but I was spending most of my time on the jet engine.

[Figure 3 shows] the first engine. For some reason or other, when the photograph was taken, they blotted out the stand on which it was mounted, but you'll see that in a later [figure]. This one had a single combustion chamber, because I was very nervous about using a multiple combustion chamber system for reasons I will explain. [This figure also shows] auxiliary things - a water pump, because we had a water cooling jacket each side of the turbine, and a fuel pump, and so forth - and this was a piece of plywood with the instruments mounted on it, and here was the control valve. All this was in the open factory in the BTH initially, and it was later thrown out by the chief engineer because he thought it was too dangerous.

When we first tried to start up the engine, I gave a signal to light up, and someone looking through a quartz window in the combustion chamber told me that it had lit up. Then we speeded the thing up with an electric motor to 2000 RPM, then I opened the throttle, and the thing accelerated, and it accelerated out of control. And so did everyone standing around it. I didn't, because I was paralyzed with fright. It's a

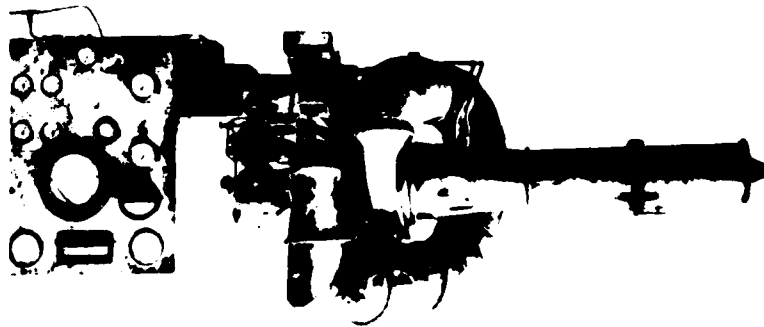


Figure 3. First Engine

funny thing - if you are actually in control, that's the kind of reaction.

Well, this happened several times, and I began to think that we had something which was fundamentally uncontrollable. The next night, which was a Tuesday evening, not only did the thing accelerate out of control on this second occasion, because the heat had weakened the spring in the fuel injector, [but] there were leaking joints at the top of the thing and flames in midair. It was pretty terrifying. The thing went off making a noise like an air raid siren. I badly needed half a bottle of wine that night.

The next day I was walking down toward the turbine factory with the deputy chief engineer of the turbine factory. He was a north countryman with a broad Yorkshire accent - which is probably not very familiar to you - and he hadn't seen the engine run. I told him how frightened I had been the night before. He said, "Ee, lad, you don't know what it is to be frightened. You should have been standing next to the Blackdown job when it jumped out of its bearings." That was a vertical turbine.

Anyway, he was present when we made our first experiment with a vaporizer in the exhaust pipe, using vaporized kerosene instead of diesel fuel.

The thing went fine, at first. It went up to 4000 RPM, beautifully under control. Then the vaporizer primed, so that instead of getting kerosene vapor in the combustion chamber, we got liquid kerosene. And off she went again. And off went Collingham at high speed, and he got jammed in a door leading out of the factory, competing with someone else trying to get out at the same time. And the chief engineer of the turbine factory was fighting for the possession of a turbine exhaust casing with one of the test hands. It was pretty exciting!

On another occasion only a few days later, the compressor fouled the casing, and the whole thing came to a screeching halt from 12,000 RPM in one and a half seconds. One of my colleagues turned to run when this terrible screech happened. Before he had even taken a pace and a half, the thing was stopped. The shop superintendant put a hand on his shoulder and said, "It's no use running, sir. It'll soon catch you if it wants." What made me laugh was this man, Walter Smith, had himself down the factory at high speed four times, at least.

Anyway, after that the chief engineer of the whole BTH turned us out - he thought it was too dangerous having this thing running in the open factory. But we did manage to rent an old iron foundry seven miles away, and there we carried on with our test work.

Well, that first engine wasn't very satisfactory. The first run was April 1937. It was, in fact, . . . the first jet engine ever to run, though the Germans were only a few weeks later. Their first engine ran in September of 1937.

We reconstructed it twice in 1937 and 1938. The first reconstruction didn't work at all well. We had a turbine failure. So we had to reconstruct it a second time, and this time I took the bold step of having a multiple combustion chamber system (see Figure 4). You wouldn't think it was the same engine, but it is, except for the sheet metal work. All the sheet metal work was new. Of course, we had to have a new turbine because

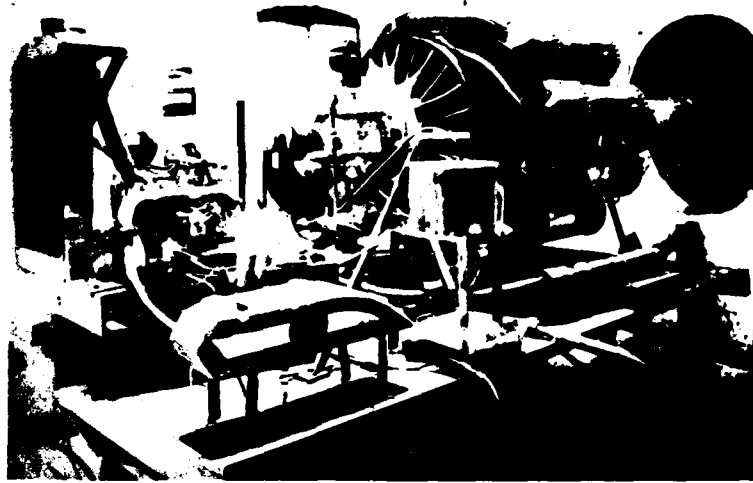


Figure 4. Reconstructed Engine with Multiple Combustion Chambers

we'd just wrecked one, but otherwise all this front end is the same, the compressor casing is the same, the rotor shaft and all the rest of it were the same as in the first engine, because we couldn't afford to do anything else. We lost a lot of time because we couldn't afford to have new parts as we should have done.

We were now starting up with a 10-horsepower BSA car engine which was connected by a pulley. The petrol tank (from a motorcycle) [was] for the car engine, [and] the radiator [was] for the starter motor.

Well, we found about a year later that we could start this thing up with the starter motor of this starting engine. The horsepower [of the] electric motor was enough to start up the experimental engine.

We couldn't get much support from the Air Ministry at first - they looked upon this as long-term research. They did put me on the special duty list after the end of my post-graduate year at Cambridge, but at first they wouldn't do anything else to help us. Then they agreed to pay about 5000£ for so many hours of running and a report and the reconstruction, and then a short time later they agreed to pay for those test houses. The test houses were built for 10,000£ - two test houses (see Figure 5).

We had a large Venturi tube inside so we could measure the airflow into the engine. But the real point of showing you [Figure 5] is to show you the conditions we had to work under. . .all this rubble all over the place. It was like working in a junk yard, and the engine wasn't much more than junk either.

[Figure 6 does not show] the actual rotor of the experimental engine, but it's sufficiently similar to explain it. As you can see, we had a single-stage, double-sided centrifugal compressor, driven by a single-stage turbine. That was really the main



Figure 5. Test Houses

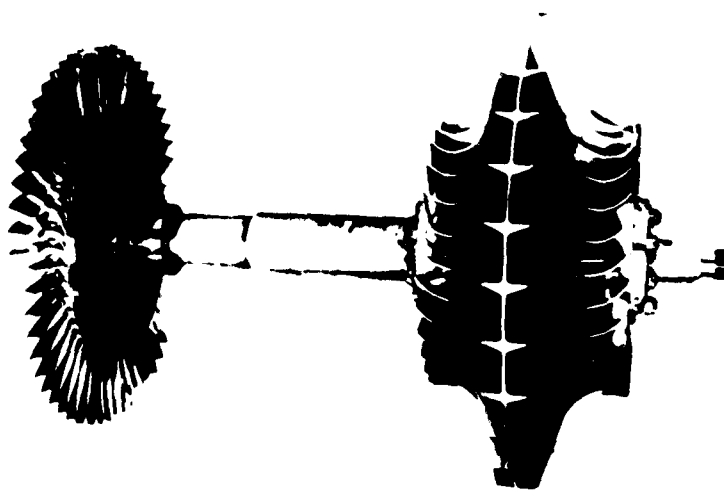


Figure 6. Turbine/Compressor Spindle

rotating part. Since no lady is present, I think I can make a comment I have made at various times: that reciprocating motion is fine in biology, but I have no use for it in engineering.

As you can see, it's pretty simple. It was simple then. They are not so simple these days. In fact, when Hives of Rolls-Royce came to see the engine, when first of all we told him the thrust was about 1000 pounds, he said, "Poo! That's not enough to blow the skin off a rice pudding." But one of his engineers - now Sir Stanley Hooker - pointed out to him that that made it more powerful than the Merlin, which was the main engine of the Royal Air Force in those days. And that made Hives change his mind about jet engines. And then, when I was explaining to him the simplicity of the thing, he said, "We'll soon design the bloody simplicity out of it." And they succeeded, because the more complicated it is, the more you can charge for it, you see.

[Figure 7 shows] what happened to the experimental engine after a very useful four

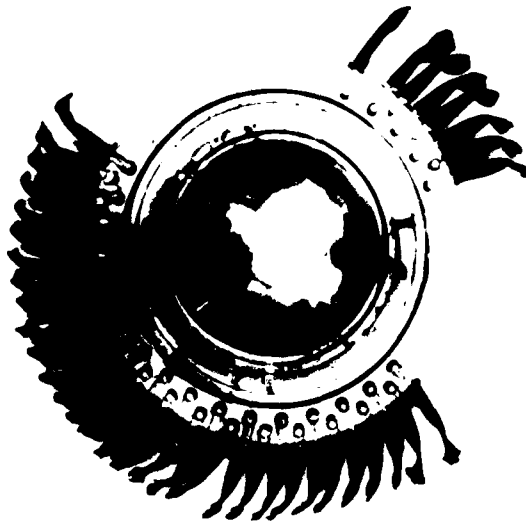


Figure 7. Failed Turbine with de Lavale
Blade Fittings

years of development running. The first turbine had the de Lavale-type [fittings] for the turbine blades, but they just weren't good enough. Before this failed, we had devised what we called the "fir tree" [fitting], which is now universally used. This was the end of about a 100-hour test - the blades came out. It was getting pretty bad before it actually failed; so bad, in fact, that every time the engine came to rest you could hear a tinkling noise as the blades flopped over in their slots.

At the end of June 1939, the Director of Scientific Research, who up to then had called this a long-term research thing, came up to see it run, and he was greatly impressed.

I had the curious experience, driving him to catch his train, when all the way to the station he was telling me all the advantages of it: how smooth it was, that it could run on almost any fuel, et cetera, et cetera. I was only a squadron leader then, so I wasn't going to argue. He decided there and then that we must have a flight engine and an airplane to put it in, and they later ruled that the flight engine must be as similar to the experimental engine as possible, and this is it. [Figure 8 shows] the W-1, the first flight engine. It's very similar to the experimental engine, except that it was a lot lighter. The experimental engine weighed about 1000 pounds, whereas this weighed about 620 pounds. It was designed for 1240 pounds of thrust, but it was derated to 860 pounds for the first flight. It flew once at 1000 pounds during flight trials. It did eventually reach 1240 pounds before we eventually retired it.



Figure 8. The W-1 Engine

[Figure 9 shows] the airplane that was built at the same time, the Gloster-Whittle E28. It was a highly successful airplane. It flew with several engines one after the other, at first with the W1-X, then with the W-1, then with the W1-A, then with the W2-B, then the W2-500, and eventually the W2-700, which was too powerful for it in fact, and couldn't be opened up fully. With the W-1 it reached a speed of about 370, which was faster than the Spitfire. With the W2-700 it did well over 500, and then started to run into compressibility troubles, and is intact in the Science Museum in London today.

The other one, the thin-winged one - the second one that was built - was lost because the ailerons seized up through contraction at the height of 32,000 feet, and Squadron Leader Davey, the pilot, had to bail out.

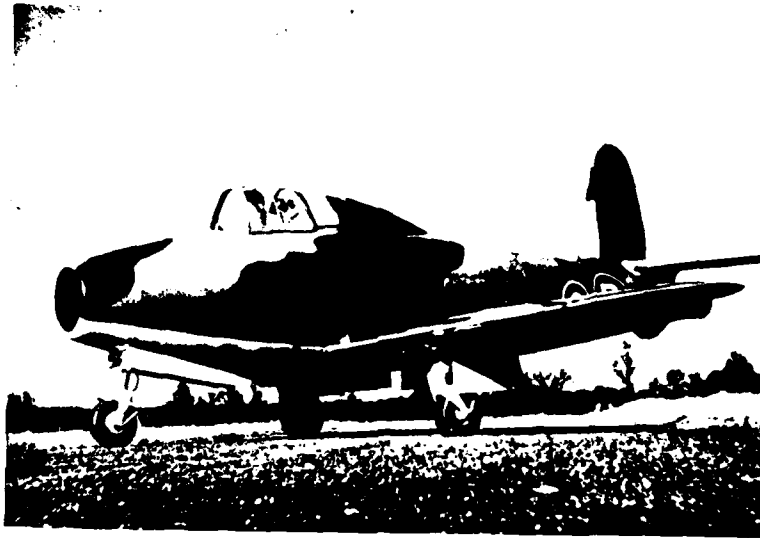


Figure 9. The Gloster-Whittle E28

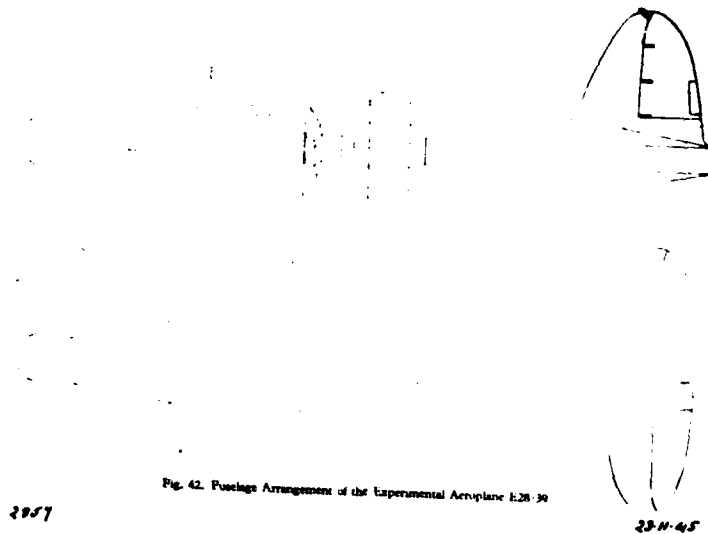


Figure 10. Fuselage Arrangement of the Experimental Airplane E28/39

[Figure 10] shows you the general arrangement of that airplane. As you can see, the air was taken in right at the front and passed around the pilot through two ducts and into the engine chamber, which was behind the fuel tank. I don't know how the pilot felt about having a fuel tank right behind him, but there it was. It never did him any harm.

Now everyone sees engines in the tail these days, but I always wanted them to be at the back of the airplane (see Figure 11). That seemed to me to be the most appropriate place. But few people realize that we did, in fact, fly the first airplane with an engine in its tail. That was the Wellington, used as a flying test bed. We were lent a Wellington.

By this time, we had our own flight testing facilities, including the Wellington, and we replaced the tail gun turret with the test cell. The Wellington, as you probably

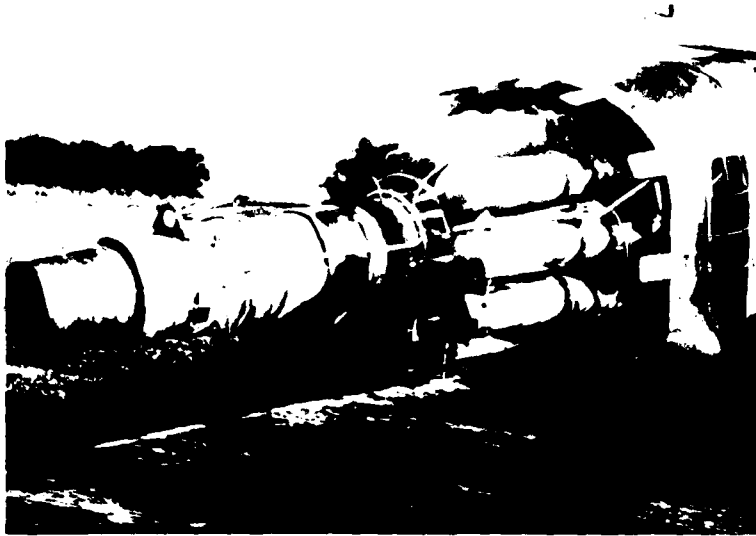


Figure 11. Jet Engine Installed in the Tail of a Wellington Bomber

know, was a twin-engined bomber, powered by two Bristol radial engines (with propellers, of course). Well, we took out the tail gunner's turret and put in the W2-B engine, which was the production version of the engine, and used this as a flying test bed.

Well, the story goes - I don't know how true it is - a B-17, which, as you know, was the standard day bomber of the U.S. Air Force (the U.S. Army Air Force, as it was in those days), a four-engine bomber, was flying along when along came a Wellington with its two-piston engines going and the W2-B in the back. The story goes that the pilot for a joke cut his two-piston engines and feathered the propellers, opened up the W2-B and overtook the B-17. So the crew of the B-17 saw a Wellington with both engines failed, as they thought, go shooting past them. They probably decided to take more water with it.

At the same time as we were doing all this, the Germans were at it too. I've often said that inventions are something which happen in several places at much the same time. Ideas ripen rather like fruit; you get several people getting the same idea at the same time, and no doubt many other people thought of jet engines at the same time as I did. The Germans were certainly doing it too. A lot of people have written to me saying that they had thought of the jet engine, and I don't doubt they did, but thinking about it is one thing, and making it work is quite another.

Well, von Ohain was at work in Germany, and [Figure 12 shows] his engine, which was quite similar to ours in many ways, except that he used a radial in-flow turbine instead of an axial-flow turbine. And though his engine ran a little later than ours, they did, in fact, get an airplane into the air before we did. They did about three or

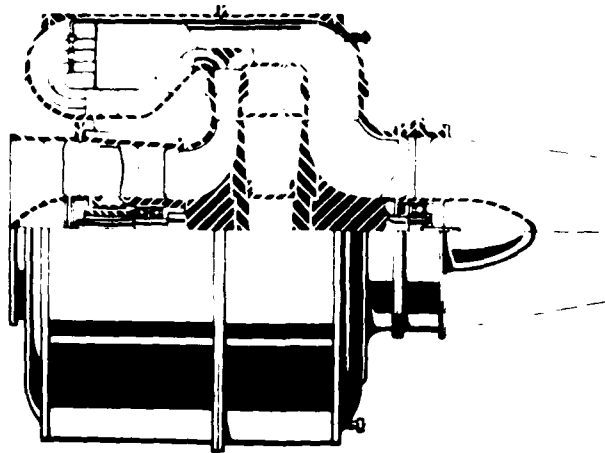


Figure 12. Schematic of von Ohain's Jet Engine

four flights. I think I am safe to say it wasn't anything like as successful as the E28, because the type of engine used in the E28 went into production, but von Ohain's engine never did. The Germans then changed over to the axial-flow type of engine, the Junkers 004, which powered the Messerschmidt Me 262.

[Figure 13 shows] the German airplane which flew in August 1939, the Heinkel He 178. An this is what von Ohain wrote on this thing when he gave it to me. Very nice!

[Shown in Figure 14 is]. . .a later version of von Ohain's engine. I can't really tell you much about it. Whether it actually flew or not, I don't know. I don't think it did, but I may be wrong.

[Figure 15 shows] the Me 262, which was really the first jet airplane to go into production. I wouldn't call it a very safe airplane. It did a lot of damage to American day bombers. It didn't do any damage to the RAF night bombers because they never sent them up at night. But it was a real menace to the American day bombers, so much so that our Meteors were withdrawn from combat duty for tactical exercises to try and find out

I Geschichtlicher Überblick

Beim fortschreitenden Entwerfen der He 178 zeigte sich, daß die Grenzen der erreichbaren Leistungsfähigkeit der Zelle, sondern die konstruktiven Möglichkeiten, die gegeben sind, im wesentlichen die Leistungsfähigkeit zeigen, bei der Entwicklung der He 178 die Schaffung eines Triebwerks, das die Anforderungen an die He 178 erfüllt.

Als in der He 178 die Entwicklung der He 178 die Schaffung eines Triebwerks, das die Anforderungen an die He 178 erfüllt.

Die von Ohain und seiner Mitarbeiter entwickelte He 178 sollte die Möglichkeit bieten, die Anforderungen an die He 178 zu erfüllen.

Das Triebwerk der He 178 ist ein Strahltriebwerk, das die Anforderungen an die He 178 erfüllt.

Die Entwicklung der He 178 ist ein Beispiel für die Entwicklung der He 178.

Die Entwicklung der He 178 ist ein Beispiel für die Entwicklung der He 178.

Hamburg auf dem einschlagenden Weg zur Entwicklung der He 178.

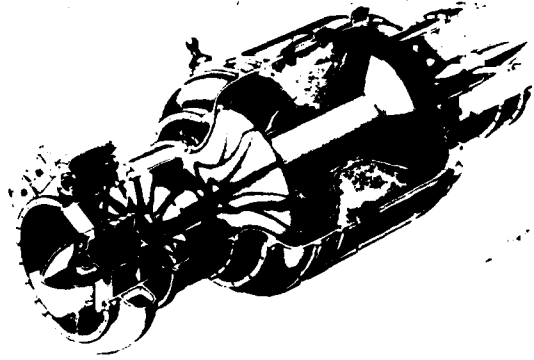
*To Sir Frank Whittle
in deep admiration
of his great life's work
Hans von Ohain
19th Sept 1966*



He 178 mit Strahltriebwerk He S 8 A

Figure 13. German He 178 Aircraft with Inscription by Hans von Ohain

Strahltriebwerk He S 8 A perspektiv-Teilschnitt



Das Strahltriebwerk der He 178 ist ein Strahltriebwerk, das die Anforderungen an die He 178 erfüllt.

Figure 14. Later Version of von Ohain's Engine

a way of dealing with jet fighters, and they didn't succeed in finding out any way.

But nevertheless, I think it's true that these things killed more of their own pilots than they did anyone else's because they had a very high wing loading - it took a hell of a long runway to get off the ground - and the engine had a most unfortunate characteristic: if you tried to open up quickly, the compressor surged and you lost power instead of gaining it. And believe me, when you are coming in and are under shooting, and you want to open up your engine, and instead of gaining power you lost it, there just is no future in it. An that's what happened several times, I understand, to these airplanes.



MESSERSCHMITT Me 262A

Figure 15. Messerschmitt Me 262A

After the war, we had a captured one at Farnborough. It took off, taking the whole of the Farnborough runway and just cleared the trees at the far end. A wing commander, a friend of mine, turned to me with a shudder and said, "Now we know why Hitler wanted to extend the Third Reich."

In 1941, before America entered the war, the British and American governments got together to arrange for the production of jet aircraft in America. The main reason, from our point of view, was that we were afraid of being bombed out, so we wanted to back up what we were doing with production in the States.

On October 1st, 1941, we flew over the W1-X engine with an engineer and two technicians to the General Electric Company. We selected them because they had already gotten a lot of experience with turbo-superchargers, which were rather similar, and they got on with the job very quickly. By April of 1942, before I went over in June, they had gotten the engine on the bench - the I-14, which was their version of our W2-B. Bell Aircraft were getting on so fast with the airplane that they had it flying on October 2nd of 1942. In fact, the Bell airplane flew before our twin-engined Meteor, but it never went into combat.

Well, [Figure 16] is it. As you can see, it had its two engines tucked in, and for the first time we used these plates to prevent the boundary layer from fouling up the flow into the intake. I was responsible for that particular feature on this thing.

[Figure 17] is one of our later engines, the W2-700, which, as I have already told you, was rather too powerful for the E28. It developed a thrust of 2000 pounds initially and reached 2500 by the time we'd developed it.

[Figure 18] shows the production airplane which was powered by Rolls-Royce Wellands, the Rolls-Royce version of the W2-B.

U S A

L-continued.



BELL XP-59A

Figure 16. Bell XP-59A

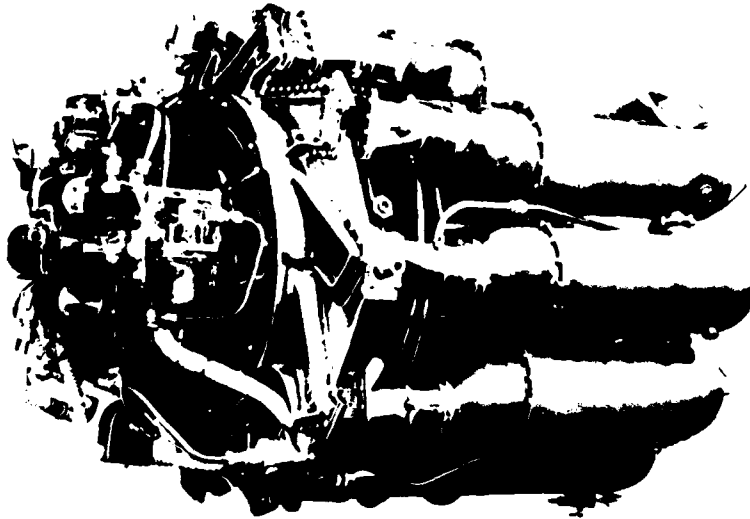


Figure 17. The W2-700 Engine

Throughout 1942 we had developed terrible problems all the time, until Rolls-Royce took over from the Rover Company, who had been selected for production. When Rolls-Royce took over, Sir Stanley Hooker became the boss, as it were, of the technical side, and things really began to move, and we soon had the Meteor in production.

They went into operation in July of 1944. Their first use was a quite unexpected



Figure 18. First Production Airplane, The Meteor,
Powered by Two W2-B Engines

one - they were used against the flying bombs, because they were the only airplanes which could catch them. Then, after this, as I've already told you, they were withdrawn for operational practice and exercises to see whether jet airplanes could be dealt with.

I flew the Meteor myself, but not until 1945, and then I had to do it by stealth because the Ministry wouldn't give me permission to fly it. But we had our own airfield then, and all the people there were subordinate to me, so I told them I was going to get into the airplane and taxi it. There was no one there who was able to say "no," and you know, it just took off.

Well, Rolls-Royce really got on with the job. They built the Nene engine, which had a thrust of 5000 pounds. One evening Hooker and another Rolls-Royce engineer and myself were having drinks in a pub in Lancashire, and one of us - I don't know who - said, "Why don't we scale down the Nene until it will fit the Meteor?"

So they did that, and six months after that conversation they built the Derwent V (see Figure 19), with which we got the airspeed record in November 1945.

I flew the Meteor again - the Meteor 3 on that occasion; not the one with the Derwent V, but one with the Derwent I. In order to keep the press quiet while a delay was going on in the attempt at the speed record, they asked me to fly the Meteor up and down the high speed course. I had the great pleasure of flying at 50 feet, flat out, up and down the high speed course. I had the wind taken out of my sails, however, when my younger son remarked, "What? Only 450? It will do 600, you know," to me. The Derwent V, incidentally, was made in thousands.

Now [Figure 20] is just to show you that we were also working on more advanced concepts. This was the basic patent for the turbofan which I took out in 1936. It doesn't

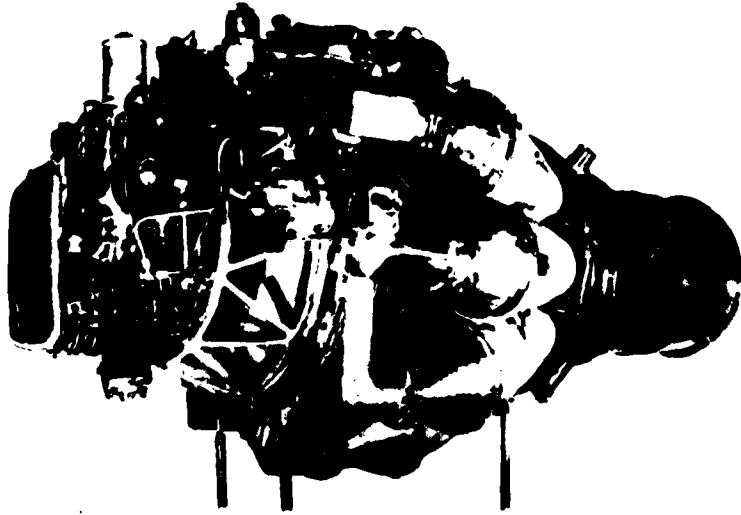


Figure 19. Derwent V Engine

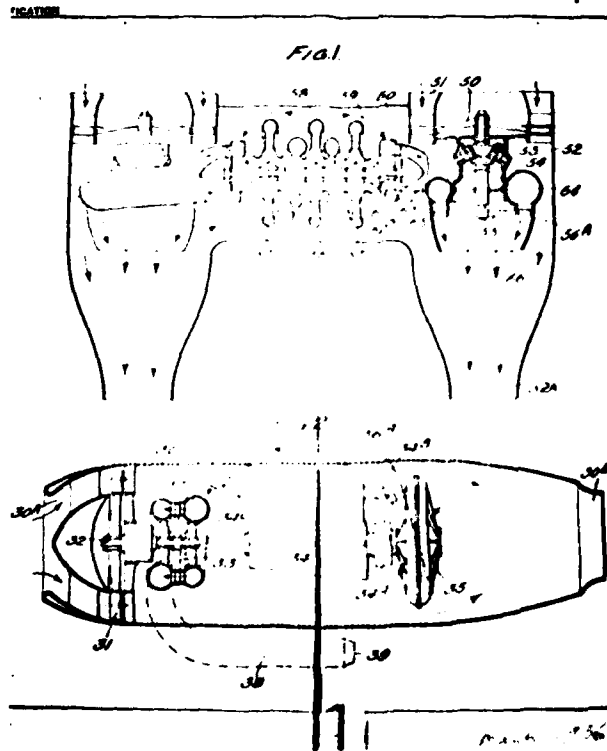


Figure 20. Schematic of Turboprop From 1936 Patent

look much like the turbofans you see these days because in order to avoid the complications of shafts going through shafts, I had [the] gas-generating unit cross-wise - cross-wise in the fuselage - and two nacelles with the fans driven by their own turbines.

Not many people realize that Power Jets were responsible for turbofans and aft-fans as well as the simple turbojet. The big disadvantage of the simple turbojet is that its propulsive efficiency is very low. So I always wanted to be able to gear down the jet; in other words, to turn a low-mass, high-velocity jet into a high-mass, low-velocity jet, and that's the whole object of the turbofan.

To make the turbofan engine was a major proposition. We couldn't spare the manpower, and we didn't have the money, so we rigged up a scheme that we could tack onto an existing engine. We called that the aft-fan, [shown in Figure 21]. It's simply something you add to the back end of the engine and use the exhaust of the main engine to drive turbines independent of the main engine, which drive a low-pressure compressor, which gears down your jet more or less, so you get a cold jetstream there and a hot jetstream here and a much better propulsive efficiency. This we call the No. 2 Thrust Augmenter. We never actually built it, but we sent the drawings to General Electric, and they, some time later, did in fact build it. The engines in the Convair 990 have them, and the Phantom

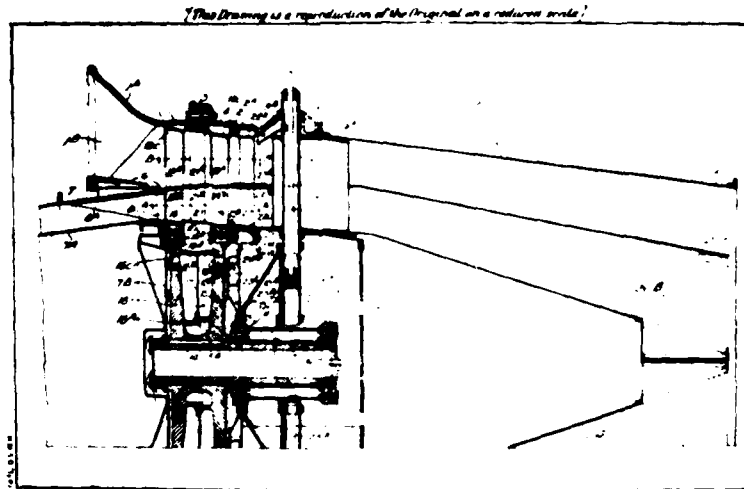


Figure 21. Schematic of Aft Fan, the No. 2 Thrust Augmenter

Fanjet has it, and other General Electric engines have it.

[Figure 22 shows a different turbofan design.] It's not a good thing to have the turbine running slower than the fan, which is inevitable in the arrangement you've just seen. It's much better to have it the other way around. So we wanted to do a tip turbine job, and have a tip turbine driving the fan instead of the other way around. The big snag there was ducting the hot exhaust from the main engine to the tip turbine without fouling up the flow into the fan.

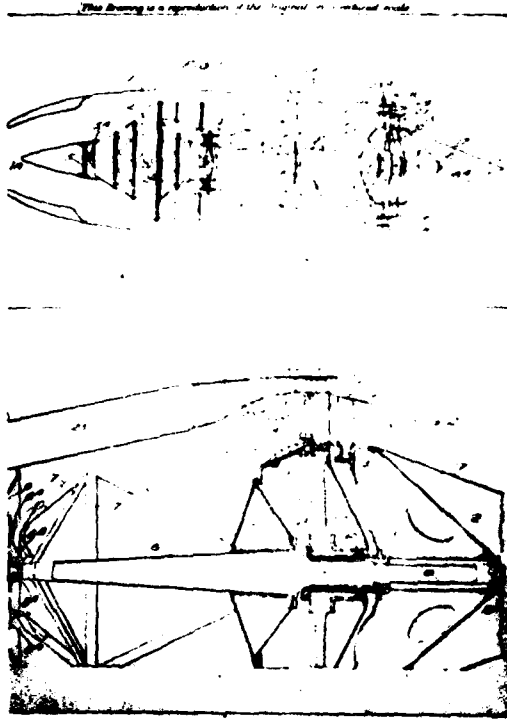


Figure 22. Alternate Turbofan Design

[Figure 23] shows you what we were trying to do. We built this one. It did, in fact, give a 40-percent improvement, but since we were expecting far more than that, we didn't go on with it because [of] the ducts leading to the blades of the tip turbine. It was a single-stage job. This is the tip turbine, with its blading on the fan blades, but the ducting did, in fact, foul up the flow into the fan. We could have done something about it if we had the time and the manpower, but we had the much more urgent job of getting on with the simple jet.

The turbofan was obviously desirable for a long range airplane. [Figure 24] shows the civil version of an airplane which was based on what we then regarded as what was needed for bomber operations in the Pacific. I went to the Staff College in 1943, and I took the opportunity of having a meeting of the students and the directing staff. We had a conference to try and define what was needed for a Pacific bomber, and we came up with 4000 miles still air range, a speed of 450 miles an hour, and so on, a bomb load of 10,000 pounds, which, of course, also made very good civil airliner specification. And that was the airplane on which we based the design of the LRI engine (Figure 25).

[The LRI ducted-fan engine] was the last engine I designed. This is just a diagram of it, and you might say it was the first turbofan to be designed. Unfortunately, Power Jets by then had been nationalized, and one consequence of nationalization was that the

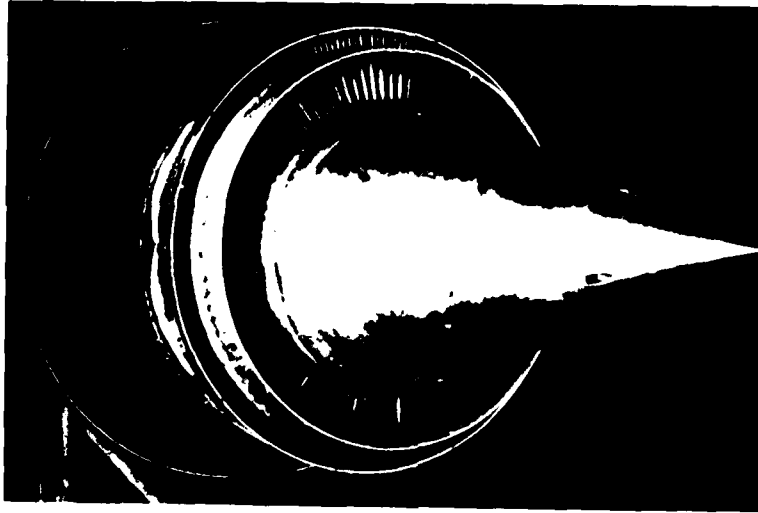


Figure 23. Built and Tested Tip Turbine Design

Transatlantic Civil Airliner - 4 LRI Engines with Ducted Fans

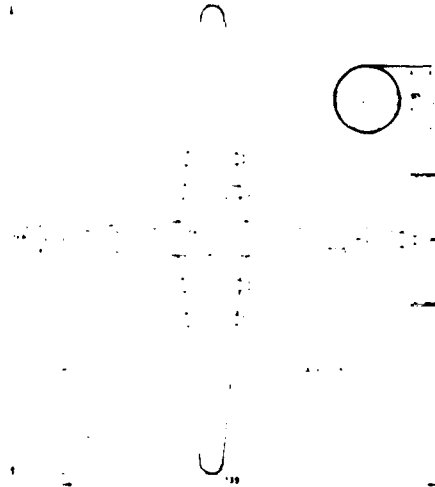


Figure 24. Transatlantic Civil Airliner
with Four LRI Ducted-Fan Engines



Figure 25. LRI Ducted-Fan Engine

contract for this thing was cancelled. In my opinion, this cost 20 years in the development of the turbofan.

As you can see (see Figure 25), this engine has a nine-stage axial-flow compressor with a single centrifugal compressor stage. That assembly was driven by a turbo-row turbine, which also drove a front fan - a two-stage front fan - via a gearbox. This diagram is, of course, very diagrammatic. It's a great pity that we were never able to complete that. It was about half done when the contract was cancelled. We had the

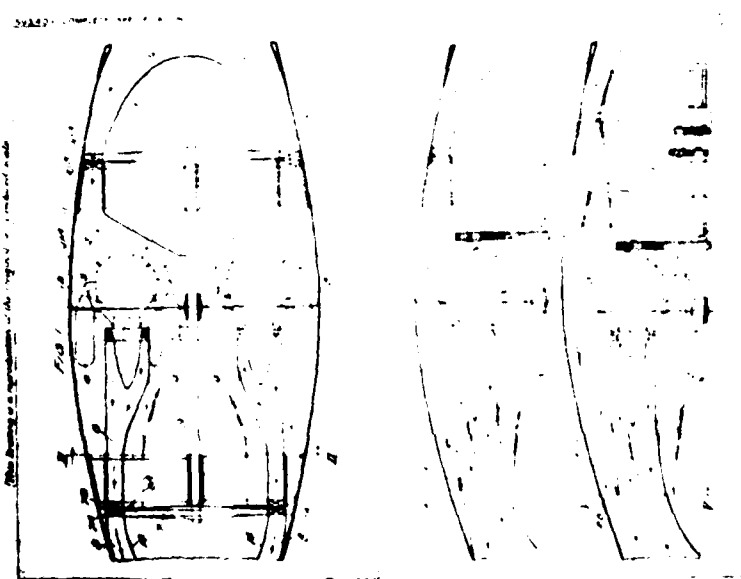


Figure 25. A Simplified Turbine-Fan Arrangement

wretched experience of being told that we were to concentrate on research and development. We were no longer to be allowed to design and build engines.

[Figure 26 shows] another arrangement by which we avoided the complications of one shaft going through another. Here we had four simple jet engines arranged round the shaft of a fan assembly, [with] the turbine driving that fan.

So, gentlemen, I'll tell you one or two more amusing stories before we go on to questions.

When that experimental airplane first flew, of course it caused an awful lot of surprise because, though you are used to seeing airplanes without propellers, no one had ever seen that sort of thing in those days. One story that came back to me was when two officers were watching at Cranwell, where we did our first flight trials. One said to the other, "How the hell does that thing work, John?" And the other one replied, "Oh, it's easy, old boy. It just sucks itself along like a Hoover."

And at a neighboring Air Force station, Waddington, which only about six miles from Cranwell, one officer was sitting in the mess and he said, "You know, chaps, I've seen a very strange airplane. It made the most peculiar noise and there was something very wrong with it, and I can't think what it was." And then he said, "Oh, my God, I must be going round the bend. It didn't have a propeller."

One more story I'll tell you. You've probably heard it.

One of the early American jet airplanes was the P-80, which looked rather like a duck, the Lockheed P-80, and the story is that two ducks were flying along when the P-80 went whistling past at 500 miles an hour. One duck said to the other, "Say, that guy is sure in a hurry to get someplace." And the other duck said, "I guess you'd be in a hurry to get any place if you had a ten-foot blowtorch where he's got it."

Well now, gentlemen, if you'd like to ask a few questions, I'll do my best to answer them.

Question: Why do you figure it was that although the American version of the Bell P59A was built early during the war, it was never used in combat?

Sir Frank: Well, you'd better ask your people about that. I just don't know the answer to that one.

Question: What was it like when you took off in a jet? How did it handle?

Sir Frank: What was it like? Oh, delightful. It was far simpler than today. On the way here I was in the cockpit of the DC-10, which is a very nice airplane from the passenger's point of view, but, my God, is the cockpit complicated! And didn't I offer to land it for them. But. . .in the days of the Meteor, all you had was the throttle and just one or two simple instruments - the air speed indicator, the altimeter, the attitude indicator, or whatever you call it these days. The. . .what is it called these days? [Flight director?] Ah, yes. Well, it was a very simple airplane to fly. Even

in those days, with the piston engine, you had to go through the routine TMP FFG, you see, when you were taking off. "T" meant trim, "M", mixture control - make sure you were in rich - "P", propeller pitch, "F", flaps - make sure your flaps are in the right position - and. . .I've forgotten now, but I had to remember it in those days. But you didn't have to worry about things other than how to set the undercarriage and flaps on the Meteor - no radiators, no pitch control, no mixture control.

Question: Sir, what did the turbodrill have to do with the turbojet?

Sir Frank: What did it have to do with the turbojet? Well, its mechanical engineering has a lot in common with the turbojet - you know, things like bearings and gears - and it has, of course, a turbine, and a pretty efficient turbine too, but it's a hydraulic turbine. But beyond that, of course, it is a very different thing, naturally, and has a very different purpose. But it does drill about four or five times as fast as the conventional method. Unfortunately, it's now "on the shelf" since Rolls-Royce went bankrupt - through a jet engine, incidentally. That brought that project to an end.

Question: What kind of engine life did the early engines in the Meteor have? How often did you have to change them?

Sir Frank: The official life was 125 hours. The Germans were lucky if their's lasted 25 hours.

The program concludes.

